

DEVELOPMENT OF A HIGH-PERFORMANCE COMPOSITE CATHODE  
FOR LT-SOFC

By

BYUNG WOOK LEE

A DISSERTATION PRESENTED TO THE GRADUATE SCHOOL  
OF THE UNIVERSITY OF FLORIDA IN PARTIAL FULFILLMENT  
OF THE REQUIREMENTS FOR THE DEGREE OF  
DOCTOR OF PHILOSOPHY

UNIVERSITY OF FLORIDA

2010

© 2010 Byung Wook Lee

To my lovely Family

## ACKNOWLEDGMENTS

I would like to thank my advisor, Dr. Eric D. Wachsman, for his support and guidance. His encouragement helped me to reach a higher level of success and expand my potential. I also would like to thank my committee members, Dr. David Norton, Dr. Juan C. Nino, Dr. Wolfgang Sigmund, and Dr. Mark Orazem, for their invaluable advice, guidance and constructive comments.

In particular, I would like to thank my colleague, Dr. Matthew Camaratta, for his endless encouragement, collaboration, and friendship. Without him, it would have been much difficult for me to get to this memorable moment of being a PhD. I also wish to acknowledge my former and current group members; Dr. Eric Armstrong, Dr. Kang Taek Lee, Nick Vito and other members for providing me excellent research environment and helpful comments. Dr. Craciun and Kerry Sieben in Major Analytical Instrumentation Center (MAIC) are also the people that I would like to give special credit for their invaluable discussion and collaboration on materials characterization.

Last but not least, I would like to give special thanks to my parents and my sister for their sincere support, patience, and trust towards me.

## TABLE OF CONTENTS

	<u>page</u>
ACKNOWLEDGMENTS.....	4
LIST OF TABLES.....	7
LIST OF FIGURES.....	8
ABSTRACT .....	11
CHAPTER	
1 INTRODUCTION .....	15
2 LITERATURE REVIEW .....	18
2.1. Operating Principles of Solid Oxide Fuel Cell .....	18
2.2. Bi-Layer Electrolyte.....	20
2.3. Single Phase Bismuth Ruthenate ( $\text{Bi}_2\text{Ru}_2\text{O}_7$ ) Cathode.....	21
2.3.1. Electronic Conductivity of Bismuth Ruthenate ( $\text{Bi}_2\text{Ru}_2\text{O}_7$ ).....	21
2.3.2. Structure of Bismuth Ruthenate ( $\text{Bi}_2\text{Ru}_2\text{O}_7$ ).....	22
2.4. Dual Phase Composite Cathode of Erbium Stabilized Bismuth Oxide ( $\text{Bi}_{1.6}\text{Er}_{0.4}\text{O}_3$ ) - Bismuth Ruthenate ( $\text{Bi}_2\text{Ru}_2\text{O}_7$ ) .....	23
2.5. Factors Affecting Cathode Performance .....	24
2.6. Infiltration or Impregnation Process .....	25
3 SYNTHESIS OF A NANO-SIZED PYROCHLORE BISMUTH RUTHENATE, $\text{Bi}_2\text{Ru}_2\text{O}_7$ , USING GLYCINE-NITRATE COMBUSTION (GNC) FOR LT-SOFC CATHODE APPLICATION.....	33
3.1. Introduction .....	33
3.2. Experimental.....	35
3.2.1. GNC $\text{Bi}_2\text{Ru}_2\text{O}_7$ Synthesis .....	35
3.2.2. Cell Fabrication .....	36
3.2.3. Characterization .....	37
3.3. Results and Discussion.....	38
3.3.1. The Effect of Glycine to Nitrate (G/N) Ratio on $\text{Bi}_2\text{Ru}_2\text{O}_7$ Synthesis.....	38
3.3.2. Particle Size Analysis .....	39
3.3.3. Phase Stability.....	41
3.3.4. Electrochemical Performance.....	41
3.4. Conclusion .....	43
4 SYNTHESIS OF IN-SITU COMPOSITE CATHODES OF BISMUTH RUTHENATE AND STABILIZED BISMUTH OXIDE FOR LT-SOFC.....	53
4.1. Introduction .....	53

4.2. Experimental .....	56
4.2.1. Stabilization of ESB Suspension .....	56
4.2.2. Synthesis Process .....	56
4.2.3. Characterization .....	58
4.3. Results and Discussion.....	58
4.3.1. Zeta Potential of ESB Suspension .....	58
4.3.2. Phase Purity of BRO7-ESB Composite and Formation of BRO7 Nanoparticles .....	60
4.3.3. Electrochemical Performance.....	60
4.4. Conclusion .....	62
5 PYROCHLORE BISMUTH RUTHENATE, $\text{Bi}_2\text{Ru}_2\text{O}_7$ , INFILTRATED CATHODES FOR HIGH-PERFORMANCE LT-SOFCS.....	72
5.1. Introduction .....	72
5.2. Experimental .....	74
5.2.1. Infiltration Process .....	74
5.2.2. Characterization .....	75
5.3. Results and Discussion.....	76
5.3.1. Cathode Microstructure and the Effect of Heating Condition.....	76
5.3.2. Compositional Analysis .....	78
5.3.3. The Effect of Infiltration on Cathode Polarization .....	78
5.3.4. Performance Comparison.....	81
5.4. Conclusion .....	82
6 SUMMARY .....	96
APPENDIX	
A ISSUE ON SYNTHESIS OF PURE $\text{Bi}_2\text{Ru}_2\text{O}_7$ .....	102
B IMPEDANCE SPECTROSCOPY.....	107
LIST OF REFERENCES .....	113
BIOGRAPHICAL SKETCH.....	119

## LIST OF TABLES

<u>Table</u>		<u>page</u>
3-1	Crystallite sizes of pure BRO7 depending on $2\theta$ using Scherrer's equation and its average .....	52
3-2	ASR values of all BRO7-ESB composite cathodes compared at each temperature measured .....	52
4-1	ASR values of all BRO7-ESB composite cathodes compared at each temperature measured .....	71
5-1	Activation energies of GNC BRO7-SS ESB (chapter 3) and infiltrated BRO7 cathodes (sample #1 and #2) calculated from Figure 5-12 using equation (5-2) .....	95
5-2	ASR values of all BRO7-ESB composite cathodes compared at each temperature measured .....	95

## LIST OF FIGURES

<u>Figure</u>	<u>page</u>
2-1 Schematic of a fuel cell, comprised of an anode, electrolyte, and cathode .....	28
2-2 Schematic view of polarizations (or overpotentials) in a SOFC .....	28
2-3 Temperature dependence of electrical conductivity for $Pb_2Ru_2O_{6.5}$ , $Bi_2Ru_2O_7$ , $CaRuO_3$ , and $SrRuO_3$ .....	29
2-4 Successive two formula units out of a pyrochlore unit cell ( $A_2B_2O_6O'$ ) .....	30
2-5 Composite cathode showing two parallel paths for oxygen species and electrons respectively .....	31
2-6 (a) $R_{ct_{eff}}$ as a function of electrode thickness (b) The effect of finer structure on $R_{ct_{eff}}$ .....	31
2-7 Schematic illustration of the current constriction effects for different cathode microstructure and current collector geometry.....	32
2-8 Schematic of the microstructure derived by two types of infiltration strategy.....	32
3-1 Flow chart of Glycine-Nitrate Combustion (GNC) route for BRO7 synthesis .....	45
3-2 Effect of Glycine to Nitrates ratio (G/N) on the crystallinity of as-synthesized BRO7 precursors.....	46
3-3 Evolution of high-purity BRO7 as a function of calcining temperature .....	46
3-4 TEM images of BRO7 nanoparticles and aggregates of those .....	47
3-5 (Left) SEM image of BRO7 aggregates calcined at 700°C for 2hrs and (Right) Energy Dispersive Spectroscopy (EDS) analysis on the particle (red circle in the left figure).....	47
3-6 Particle size distribution of BRO7 particles measured by TSI PSD 3603 (Aerosizer) .....	48
3-7 Thermogravimetric (TG) plot to show the stability of the final BRO7 calcined 700°C 2hrs powder at temperature range of 25~1000°C .....	48
3-8 a) Nyquist and b) Bode plots as a function of temperature for GNC BRO7-SS ESB composite cathode tested in air .....	49
3-9 Overlapped Bode plots measured at 600°C of BRO7-ESB composite cathodes .....	50

3-10	Arrhenius plot of ASR for comparison of GNC BRO7-SS ESB with the other BRO7-ESB composite cathodes reported .....	51
4-1	Molecular structure of ammonium citrate dibasic.....	64
4-2	Flow chart of synthesis process for in-situ ESB-BRO7 composite cathodes .....	64
4-3	Zeta potential of ESB powder suspension with or without a dispersant (ammonium citrate) as a function of pH.....	65
4-4	XRD patterns of in-situ ESB-BRO7 composite cathodes depending on calcining temperatures .....	66
4-5	SEM image of in-situ BRO7-ESB composites showing adsorbed BRO7 nanoparticles on ESB phase .....	67
4-6	a) Nyquist and b) Bode plots of in-situ BRO7-ESB composite cathode tested at each temperature in air under open circuit potential.....	68
4-7	Overlapped Bode plots measured at 600°C of BRO7-ESB composite cathodes .....	69
5-1	Schematic of infiltration process .....	83
5-2	Temperature profiles of two different heat treatment conditions for sample #1 and sample #2 .....	83
5-3	Schematic of impedance testing set-up.....	84
5-4	Cross-sectional SEM images of a) sample #1 and b) sample #2 .....	84
5-5	SEM images of BRO7 nanoparticles: the same spot with (a) low (b) high (zoomed-in) magnifications.....	85
5-6	a) Representative SEM image of infiltrated BRO7-ESB composite cathodes showing the region (bright region in the middle of image) used for porosity calculation where 30 vol% of graphite was used as a pore-former to construct ESB scaffolds and b) calculated average porosity and its standard deviation....	86
5-7	TEM images and EDS spectra of a) ESB scaffold and b) BRO7 nanoparticles with red circle on Ru element energy spectrum indicating the presence of Ru element in BRO7 nanoparticles .....	87
5-8	Nyquist plots of BRO7 infiltrated ESB composite cathode (sample #1) at different temperatures (550~700°C) .....	88
5-9	Nyquist plots of BRO7 infiltrated ESB composite cathode (sample #2) at different temperatures (550~700°C) .....	89

5-10	Overlapped Nyquist plots of GNC BRO7-SS ESB, infiltrated BRO7-ESB sample #1, and sample #2 at different temperatures (550~700°C) to better show the improvement of performance .....	90
5-11	Overlapped Bode plots of BRO7 infiltrated ESB composite cathodes (sample #1 and #2) and GNC BRO7-SS ESB composite cathode at different temperatures (550~700°C) for comparison on dominating processes.....	91
5-12	Arrhenius plot of ASR for performance comparison with several conventionally mixed composite cathodes and the other infiltrated cathodes reported .....	92
5-13	Overlapped Bode plots of BRO7 infiltrated ESB cathodes (sample #1 and #2), conventionally mixed BRO7-ESB composite cathode, and YSB infiltrated LSM cathodes at 700°C.....	93
5-14	Arrhenius plot of ASR for performance comparison with all conventionally mixed BRO7-ESB composite cathodes .....	94
A-1	Diffraction patterns of $\text{Bi}_3\text{Ru}_3\text{O}_{11}$ (or $\text{Bi}_2\text{Ru}_2\text{O}_{7.3}$ ) synthesized with amorphous citrate reaction method .....	105
A-2	Diffraction patterns of BRO7 and impurity phases such as $\text{Bi}_3\text{Ru}_3\text{O}_{11}$ (or $\text{Bi}_2\text{Ru}_2\text{O}_{7.3}$ ) synthesized with GNC method.....	105
A-3	Diffraction patterns of BRO7 (bottom) before and (top) after leaching taken from the literature .....	106
B-1	Typical impedance cell response on complex plane and its equivalent circuit .	111
B-2	Typical Warburg impedance response on complex plane .....	111
B-3	Impedance response for as-sintered (1500°C, 4 hr) HS3Y samples (circles), annealed at 1200°C for 110 hr in both 10% $\text{H}_2$ balance $\text{N}_2$ atmosphere (triangles), and air (diamonds) showing the effect of increasing grain size .....	112
B-4	a) Equivalent circuit and b) impedance response in complex plane for mixed kinetic and charge transfer control.....	112

Abstract of Dissertation Presented to the Graduate School  
of the University of Florida in Partial Fulfillment of the  
Requirements for the Degree of Doctor of Philosophy

DEVELOPMENT OF A HIGH-PERFORMANCE COMPOSITE CATHODE  
FOR LT-SOFC

By

Byoung Wook Lee

December 2010

Chair: Eric D. Wachsman

Major: Materials Science and Engineering

Solid Oxide Fuel Cell (SOFC) has drawn considerable attention for decades due to its high efficiency and low pollution, which is made possible since chemical energy is directly converted to electrical energy through the system without combustion. However, successful commercialization of SOFC has been delayed due to its high production cost mainly related with using high cost of interconnecting materials and the other structural components required for high temperature operation. This is the reason that intermediate (IT) or low temperature (LT)-SOFC operating at 600~800°C or 650°C and below, respectively, is of particular significance because it allows the wider selection of cheaper materials such as stainless steel for interconnects and the other structural components. Also, extended lifetime and system reliability are expected due to less thermal stress through the system with reduced temperature. More rapid start-up/shut-down procedure is another advantage of lowering the operating temperatures. As a result, commercialization of SOFC will be more viable.

However, there exists performance drop with reduced operating temperature due to increased polarization resistances from the electrode electrochemical reactions and

decreased electrolyte conductivity. Since ohmic polarization of the electrolyte can be significantly reduced with state-of-the art thin film technology and cathode polarization has more drastic effect on total SOFC electrochemical performance than anode polarization as temperature decreases, development of the cathode with high performance operating at IT or LT range is thus essential.

On the other hand, chemical stability of the cathode and its chemical compatibility with the electrolyte should also be considered for cathode development since instability and incompatibility of the cathode will also cause substantial performance loss.

Based on requirements of the cathode mentioned above, in this study, several chemico-physical approaches were carried out to develop a high-performance composite cathode, in particular, for LT-SOFC operating 650°C and below since stability and compatibility of the materials in interest are secured at low temperatures.

First, a nano-sized pyrochlore bismuth ruthenate ( $\text{Bi}_2\text{Ru}_2\text{O}_7$  or BRO7 shortly), one of the promising cathode materials, was successfully synthesized using glycine-nitrate combustion (GNC) route. Stoichiometric  $\text{Bi}_2\text{Ru}_2\text{O}_7$  without any impurity phase was achieved with considerably improved processing condition, leading to the crystallite size of ~24nm in diameter. Even though the resulting powder tends to agglomerate, resulting in overall 200~400nm size range, it still showed better quality than the one prepared by solid state (SS) reaction route followed by extra milling steps such as vibro-milling and sonication for further particle size reduction. Glycine-to-nitrate (G/N) ratio was found to play a critical role in determining the reaction temperature and reaction duration, thus phase purity and particle morphology (particle size, shape, and agglomeration etc). Composite cathodes of such prepared BRO7 (GNC BRO7) combined with SS erbia-

stabilized bismuth oxide,  $\text{Bi}_{1.6}\text{Er}_{0.4}\text{O}_3$  or ESB, showed better electrochemical performance than vibro-milled BRO7 (VM BRO7)-SS ESB. ASR values of  $0.123\Omega\text{cm}^2$  at  $700^\circ\text{C}$  and  $4.59\Omega\text{cm}^2$  at  $500^\circ\text{C}$ , respectively, were achieved, which follows well the trend of particle size effect on performance of composite cathodes. Additionally, the number of processing steps (thus time) was reduced by GNC route. Several issues in regard to synthesis process and characteristics of BRO7 material itself will be addressed in this dissertation.

Secondly, a unique in-situ composite cathode synthesis was successfully developed and applied for BRO7-ESB composite cathodes to improve percolation and to reduce agglomeration of each phase inside the cathode so that the effective triple phase boundary (TPB) length was extended. To disperse and stabilize ESB powder in de-ionized (DI) water, zeta potential profile of ESB powder in DI water as a function of pH was first achieved. The effect of a dispersant (ammonium citrate dibasic) on the stability of ESB powder dispersed in DI water was also investigated. Knowledge of BRO7 wet chemical synthesis from previous study was utilized for final product of in-situ BRO7-ESB composite cathodes. Such prepared composite particles were characterized and the electrochemical performance of in-situ BRO7-ESB composite cathodes was examined as well. Performance enhancement was observed so that ASR values of  $0.097\Omega\text{cm}^2$  and  $3.58\Omega\text{cm}^2$  were achieved at  $700^\circ\text{C}$  and  $500^\circ\text{C}$ , respectively, which were 19% and 22% improvement, respectively compared to those of conventionally mixed composite cathodes of BRO7-ESB.

Finally, a highly controlled nanostructured BRO7-ESB composite cathode was developed by infiltration of BRO7 onto ESB scaffolds to maximize the effective TPB

length, to improve the connectivity of ESB phase inside the cathode for better oxygen-ion diffusion, and to minimize delamination between the electrolyte and cathode layers. ESB scaffolds were first established by adding a graphite pore-former and controlling heat treatment condition. Nano-sized BRO7 particles were successfully created on the surface of previously formed ESB scaffold by infiltration of concentrated (Bi, Ru) nitrate solution followed by the optimized heat treatment. Such prepared composite cathodes exhibited superior electrochemical performance to conventionally made BRO7-ESB composite cathodes and even better than GNC BRO7-SS ESB developed in this dissertation, e.g.  $0.073\Omega\text{cm}^2$  at  $700^\circ\text{C}$  and  $1.82\Omega\text{cm}^2$  at  $500^\circ\text{C}$ , respectively. This cathode system was revealed to be highly competitive among all the reported composite cathodes consisting of the same or different materials prepared by various processing techniques. It was demonstrated that the extended TPB length from continuous network of BRO7 nanoparticles and better connectivity of ESB scaffolds enabled the outstanding performance. Moreover, de-lamination of cathode from the electrolyte was prevented thanks to improved adhesion between ESB scaffolds and ESB electrolyte.

Dissociative adsorption of oxygen gas were proposed to be the dominant rate-determining process for the overall oxygen reduction reaction at low temperatures ( $500\text{-}600^\circ\text{C}$ ) whereas all of the constituting sub-reactions such as oxygen gas dissociative adsorption, oxygen ion diffusion towards TPB region, and oxygen ion incorporation were found to play roles competitively in the overall reaction at relatively high operating temperature ( $650\text{-}700^\circ\text{C}$ ) based on analysis of impedance spectra.

## CHAPTER 1 INTRODUCTION

A fuel cell is a device that converts the chemical energy directly into electricity by electrochemically combining a fuel with an oxidant through an ion-conducting electrolyte. Among various kinds of fuel cells depending on the type of electrolyte being used, solid oxide fuel cell (SOFC), in particular, has received great attention as an alternative electric power generation system due to its high electrical efficiency, fuel flexibility, and minimal environmental impact etc.<sup>1-2</sup>

Owing to the high installation costs and poor systems durability, however, conventional high temperature SOFC operating at around 1000°C has prevented its widespread commercialization. As a result, tremendous effort has been devoted to the development of low temperature SOFC (LT-SOFC) operating at 500-700°C since it can bring the advantages over the conventional high temperature SOFC as below.<sup>3-4</sup>

- Use of low-cost metallic materials such as ferritic stainless-steels for interconnect and construction materials, which makes both the stack and balance-of-plant cheaper
- Longer operational lifetime and system reliability
- More rapid start-up and shut-down procedures required for potential applications in transportation and mobile applications

From an electrical point of view, however, reduction of the operating temperature is detrimental because the electrochemical processes limiting performance of the cell (anodic reactions, ion transport in the electrolyte and cathodic reactions) are thermally activated and become considerably slower at reduced temperatures.<sup>5</sup> In particular, the more temperature goes down, the bigger cathode polarization plays a role in governing overall performance of the cell. Consequently, the development of a cathode with low

cathode polarization is inevitable in order to achieve reasonable electrochemical performance of LT-SOFC which is  $\sim 0.5 \text{ W/cm}^2$  at operating voltage of  $\sim 0.7 \text{ V}$ .<sup>2</sup>

It is well known that a composite cathode, consisting of an electro-catalyst with high electronic conductivity and an oxygen-ion conducting phase, reduces the cathode polarization significantly by effectively extending the reaction zone from the electrode/electrolyte interface into the electrode and by adding the ionic conductivity to the electrode, which provides additional path for transport of oxygen species to the cathode/electrolyte interface.<sup>6-7</sup>

In addition, further decrease in the cathode polarization can be achieved by two distinct approaches. One is to control the geometrical parameters such as porosity, particle size, volume fraction, and spatial distribution of each component for composite cathodes based on percolation theory for better gas diffusion and connectivity of constituent phases. The other is to improve the materials properties such as the electronic conductivity and/or catalytic activity towards the oxygen reduction by doping or replacing the electrode material by itself<sup>5</sup>.

Meanwhile, since the cathode polarization also depends on the electrolyte materials system upon which the cathode is deposited as well as the cathode system by itself, care should be taken to select the right combination between the cathode and electrolyte.<sup>8</sup>

Abhishek et al. from our group developed a composite cathode consisting of Bismuth ruthenate ( $\text{Bi}_2\text{Ru}_2\text{O}_7$  or BRO7) and 20 mol% erbia-stabilized bismuth oxide ( $(\text{Bi}_2\text{O}_3)_{0.8}(\text{Er}_2\text{O}_3)_{0.2}$  or ESB) that shows area specific resistance (ASR) values as low as

$\sim 0.08\text{cm}^2$  and  $\sim 3.47\Omega\text{cm}^2$  at  $700^\circ\text{C}$  and  $500^\circ\text{C}$ , respectively, on gadolinium doped ceria (GDC) as the electrolyte.<sup>9</sup>

More recently, Camaratta showed in his study that the composite cathode of ESB-BRO7 can be further optimized by introducing pure BRO7 current collector and changing microstructure such as constituent particle size and electrode thickness.<sup>10</sup> The best performance that he obtained was ASR as low as  $\sim 0.03\Omega\text{cm}^2$  and  $\sim 0.73\Omega\text{cm}^2$  at  $700^\circ\text{C}$  and  $500^\circ\text{C}$ , respectively, on 20ESB electrolyte with micron size of ESB and nano-size of BRO7, which is comparable to one of the best results reported by Shao and Haile for  $\text{Ba}_{0.5}\text{Sr}_{0.5}\text{Co}_{0.8}\text{Fe}_{0.2}\text{O}_{3-\delta}$  (BSCF).<sup>11</sup> However, it should be pointed out that yield ratio to get fine particles ( $<100\text{nm}$ ) of BRO7 was prohibitively low. Therefore, the more effective processing route is essential to get reproducible and scalable BRO7-ESB composite cathode systems without compromising high performance verified from previous study.

Consequently, if all the requirements mentioned above for the optimized composite cathode were satisfied, it is expected to achieve a high-performance composite cathode with low production cost, enabling the realization of LT-SOFC.

## CHAPTER 2 LITERATURE REVIEW

### 2.1. Operating Principles of Solid Oxide Fuel Cell

The primary components of a fuel cell are an ion conducting electrolyte, a cathode, and an anode as shown in Figure 2-1.<sup>4</sup> In the simplest example, a fuel such as hydrogen is fed into the anode and an oxidant, typically oxygen, into the cathode. The electrolyte serves as a barrier to gas diffusion, but allows the transport of ions (e.g.  $O^{2-}$ ) across it. Oxygen gas, combining with electrons, is electro-reduced at the cathode to produce  $O^{2-}$  which is driven across the electrolyte by the chemical potential (or oxygen partial pressure) difference between the two sides of the electrolyte due to the oxidation of fuel at the anode. Free electrons are released at the anode when the fuel is oxidized, and they travel to the cathode through an external circuit. Thus, the oxygen partial pressure gradient ( $P_{O_2}$ ) over the electrolyte is a driving force for the electromotive force across the electrolyte, which sets up a terminal voltage towards the external load.<sup>12</sup>

The theoretical open-circuit potential for a cell with oxygen potential gradient is given by the well-known Nernst equation in a cell,<sup>4</sup>

$$E = \frac{-\Delta G}{nF} = -\frac{RT}{4F} \cdot \ln \frac{P_{O_2}'}{P_{O_2}''} \quad (2-1)$$

where  $P_{O_2}''$  and  $P_{O_2}'$  are the equilibrium partial pressure of oxygen at the anode and cathode respectively, R is the ideal gas constant, F is Faraday's constant, and T is the absolute temperature. The coefficient (n) in the denominator represents the number of electrons transferred per mole of oxygen molecules during reduction in the cell.

However, the output potential of a SOFC in practical operation is lower than the ideal values due to the over-potential ( $\eta$ ) or potential loss induced from polarization. The total cell polarization consists of three major contributions caused by different mechanisms- ohmic polarization, activation polarization, and concentration polarization as shown in Figure 2-2 and it can be expressed as the equation as follows:

$$\eta_{total} = \eta_{\Omega} + \eta_A + \eta_C \quad (2-2)$$

The drop of potential due to activation polarization is associated with the electrochemical reactions in the electrodes. The second drop of potential comes from the ohmic resistance when ions and electrons conduct in the electrolyte and electrodes, respectively. The third drop, which could be significant at high current densities, attributes to the mass transport resistance, or concentration polarization, of gas species.

The rate of electrode reaction can be related to the activation polarization by the Butler-Volmer equation;<sup>13</sup>

$$i = i_o \left( \exp\left(\frac{(1-\beta)nF}{RT} \eta_{act}\right) - \exp\left(-\frac{\beta nF}{RT} \eta_{act}\right) \right) \quad (2-3)$$

where  $\beta$  is the symmetric factor representing the fraction of applied potential promoting the cathodic reaction. R, T,  $\eta$  and F are the gas constant, absolute temperature, the number of electrons involved in the reaction and Faraday constant respectively.  $i_o$  is the exchange current density and  $i$  is the current density (negative for the cathode current).

In the low current density regime, it can be simplified as

$$\eta_{act} \cong -\frac{RT}{\beta nF} \ln\left(\frac{-i}{i_o}\right) \quad \text{when } \beta F \eta_{act} \ll -RT \quad (2-4)$$

In large current density regime, on the other hand, Tafel equation is applicable:

$$\eta_{act} \cong a + b \ln i \quad (2-5)$$

where a and b are influenced by the electrode microstructure and thickness.

## 2.2. Bi-Layer Electrolyte

With regard to an electrolyte material for LT-SOFC, doped ceria and stabilized bismuth oxide have been proposed and studied by many researchers due to their relatively high ionic conductivities at 500-700°C. It has been shown that Gd-doped ceria (GDC) with as low as ASR of  $\sim 0.15 \Omega \text{cm}^2$  can be achieved with thickness of 15 $\mu\text{m}$  at 500°C.<sup>14</sup> Stabilized cubic bismuth oxides, on the other hand, are known to exhibit the highest ionic conductivities due to their inherent concentration of oxygen vacancies and weak metal-oxide bonds.<sup>15-16</sup> The highest ionic conductivity was obtained by the fcc phase of  $\text{Er}_2\text{O}_3$  stabilized  $\text{Bi}_2\text{O}_3$  (ESB). Verkerk et al. examined the oxygen ion conductivity of 20mol%  $\text{Er}_2\text{O}_3$  stabilized  $\text{Bi}_2\text{O}_3$  (20ESB) and reported its values as 0.37S/cm and 0.023S/cm at 700°C and 500°C, respectively.<sup>17</sup> However, each of them has some critical issues to be used alone as an electrolyte. For GDC, when it is placed at low oxygen partial pressures ( $< 10^{-14}$  atm),  $\text{Ce}^{4+}$  is reduced into  $\text{Ce}^{3+}$  leading n-type electronic conduction with  $P(\text{O}_2)^{-1/4}$  dependence.<sup>18</sup> This phenomenon lowers the ionic transference number ( $t_i$ ) and open circuit potential (OCP) of the cell using GDC as an electrolyte due to the electronic conduction through it, thus resulting in the lower cell efficiency. Meanwhile, bismuth oxide-based electrolytes seem to show the decomposition of  $\text{Bi}_2\text{O}_3$  to Bi under a moderate reducing atmosphere, which seriously limits its application in fuel cell environments. Takahashi et al. showed that the

decomposition of Bi/Bi<sub>2</sub>O<sub>3</sub> happens under the oxygen partial pressure ( $P_{O_2}$ ) of  $\sim 10^{-13.1}$  atm at 600°C.<sup>19</sup>

As an alternative, Wachsman et al. developed a bi-layer electrolyte concept to overcome the thermodynamic instability of both materials.<sup>20-21</sup> In their work, they demonstrated that higher OCP was obtained using bi-layer of doped ceria and stabilized bismuth oxide than using each of single electrolyte layer respectively since the ceria layer prevents the bismuth oxide layer from decomposing by shielding it from low  $P_{O_2}$  in the anode side and, in turn, the bismuth oxide layer serves to block the electronic conduction through doped ceria into the cathode side. Therefore, the development of a cathode system applicable for GDC/ESB will be reasonable.

### **2.3. Single Phase Bismuth Ruthenate (Bi<sub>2</sub>Ru<sub>2</sub>O<sub>7</sub>) Cathode**

#### **2.3.1. Electronic Conductivity of Bismuth Ruthenate (Bi<sub>2</sub>Ru<sub>2</sub>O<sub>7</sub>)**

For a single phase purely electronic conducting cathode, it has to meet the following requirements: high electronic conductivity at operating temperature, thermal and chemical compatibility with the electrolyte, namely, similar thermal expansion coefficients (TEC) and no reaction with the electrolyte, and high catalytic activity for oxygen reduction.<sup>22</sup>

In the beginning of bismuth/ceria bi-layer SOFC research, the cathode materials were mainly gold or platinum, a single phase purely electronic conducting cathode, since rather widely used perovskite cathodes with low cathode polarization have the high reactivity with bismuth oxides.<sup>23</sup>

Meanwhile, pyrochlores based on bismuth ruthenate, lead ruthenate, and yttrium ruthenate have been studied as cathodes for application in SOFC since they exhibit relatively high electrical conductivity.<sup>24-26</sup> In particular, Takeda et al. studied pyrochlores

such as  $\text{Bi}_2\text{Ru}_2\text{O}_7$  and  $\text{Pb}_2\text{Ru}_2\text{O}_{6.5}$  and perovskites such as  $\text{CaRuO}_3$ ,  $\text{SRRuO}_3$  as cathode materials for YSZ based SOFC. As can be seen in Figure 2-3,<sup>25</sup> they observed metallic behavior for pyrochlores with almost temperature independent conductivity ( $10^2$ - $10^3$  S/m from room temperature up to 900 °C), which is comparable to the best conventional single phase cathode materials. However, since cathode reaction sites (TPBL) are limited to near the interface between the electrolyte and cathode for single phase purely electronic conducting, it is more desirable to introduce an ionic conducting phase into the cathode layer so as to increase TPBL and ionic conductivity resulting in lower polarization.

### 2.3.2. Structure of Bismuth Ruthenate ( $\text{Bi}_2\text{Ru}_2\text{O}_7$ )

Successive 2/8 formula units out of a pyrochlore  $\text{A}_2\text{B}_2\text{O}_7$  unit cell (consisting of eight formula units) are shown in Figure 2-4. It belongs to the family of cubic pyrochlore-type structure with  $Fd\bar{3}m$  space group and lattice parameter of  $a \approx 10.29 \text{ \AA}$ .<sup>27-28</sup> The cation sublattice consists of bigger  $\text{A}^{3+}$  ( $\text{Bi}^{3+}$  in  $\text{Bi}_2\text{Ru}_2\text{O}_7$ ) and smaller  $\text{B}^{4+}$  ( $\text{Ru}^{4+}$  in  $\text{Bi}_2\text{Ru}_2\text{O}_7$ ) which order into alternate (110) rows in every other (001) plane and into alternate ( $\bar{1}10$ ) rows in the other (001) planes respectively. This cation ordering provides three distinguishable tetrahedral sites for the oxygen ions: 8a sites surrounded by 4  $\text{A}^{3+}$  ( $\text{Bi}^{3+}$  in  $\text{Bi}_2\text{Ru}_2\text{O}_7$ ) cations, 8b sites surrounded by 4  $\text{Ru}^{4+}$  cations, and 48f sites surrounded by 2  $\text{Bi}^{3+}$  and 2  $\text{B}^{4+}$  ( $\text{Ru}^{4+}$  in  $\text{Bi}_2\text{Ru}_2\text{O}_7$ ) cations. While 8a and 48f sites are occupied, 8b sites are vacant, which results in an ordered oxygen ion sublattice. Thus, the formula unit of the pyrochlore can also be written as  $\text{A}_2\text{B}_2\text{O}_6\text{O}'$  ( $\text{Bi}_2\text{Ru}_2\text{O}_6\text{O}'$  for  $\text{Bi}_2\text{Ru}_2\text{O}_7$ ) to distinguish between the oxygen ions occupying the 48f site as O and those occupying the 8a sites as O'.

An electronic band structure study was carried out for metallic  $\text{Bi}_2\text{Ru}_2\text{O}_7$ , which revealed that the metallic character originates from the Ru  $t_{2g}$ -block bandwidth where the more Ru  $t_{2g}$ -block bandwidth increases resulting from an increase in Ru-O-Ru bond angle and an shortening of the Ru-O bond, the more the material becomes metallic.<sup>29-30</sup>

#### **2.4. Dual Phase Composite Cathode of Erbia Stabilized Bismuth Oxide ( $\text{Bi}_{1.6}\text{Er}_{0.4}\text{O}_3$ ) - Bismuth Ruthenate ( $\text{Bi}_2\text{Ru}_2\text{O}_7$ )**

Since dual phase composite cathodes, consisting of an ionic conducting phase and an electronic conducting phase, have proved to have lower cathode polarization than a single phase purely electronic conducting cathode,<sup>6, 31-32</sup> the development of dual phase composite cathodes for bismuth/ceria bi-layer electrolyte has been a focus of study in our group. In general, composite cathodes, consisting of an electro-catalyst with high electronic conductivity and an oxygen-ion conducting phase, are expected to not only increase TPBL, which results in lower over-potential toward oxygen reduction, but shorten surface diffusion path of dissociatively adsorbed oxygen to TPB sites upon addition of an ionic conducting phase as can be seen Figure 2-5.<sup>33</sup> Moreover, there arises an additional path for transport of oxygen species such as bulk diffusion through the ionic conducting phase. Thermal expansion also can be matched well between the composite cathode and electrolyte due to use of the same ionic conducting phase in both layers. For instance, a composite cathode of ESB-BRO7 exhibiting ASR as low as  $\sim 0.03\Omega\text{cm}^2$  and  $\sim 0.73\Omega\text{cm}^2$  at  $700^\circ\text{C}$  and  $500^\circ\text{C}$ , respectively, on 20ESB electrolyte was developed thanks to the high electronic conductivity and catalytic activity towards oxygen reduction of BRO7 phase and the high ionic conductivity of ESB phase as well. As expected, this composite cathode system showed no chemical reactivity with ESB electrolyte used.<sup>10</sup>

## 2.5. Factors Affecting Cathode Performance

Virkar et al. developed theoretical model showing the effect of porous composite electrodes on the overall charge-transfer process by taking into account various parameters such as intrinsic charge-transfer resistance, electrode thickness, ionic conductivity of the ionic conducting phase and porosity etc.<sup>32, 34</sup>

Low current regime is assumed so that the activation polarization can be approximated as being ohmic as follows;

$$\eta_{act} \approx \frac{RT}{zFi_0} i = R_{ct} i \left( R_{ct} = \frac{RT}{zFi_0} \right) \quad (2-6)$$

Diffusion of gaseous species in porous electrodes is assumed to be rapid so as not to be rate limiting. Also, the electronic conductivity in the electronic conducting phase is assumed to be high enough. The performance of the electrodes is judged by the effective charge-transfer resistance ( $R_{ct}^{eff}$ ), which is defined as ASR of the entire SOFC minus ASR of the dense electrolyte. It was demonstrated that  $R_{ct}^{eff}$  decreases as the thickness of the composite cathode increases, eventually approaching an asymptotic minimum as can be seen in Figure 2-6(a). On the contrary, as the electrode thickness approaches zero,  $R_{ct}^{eff}$  becomes close to the intrinsic charge-transfer resistance  $R_{ct}$  implying that the electrode behaves as thin single phase electronic conducting cathode. In addition, the model shows that finer microstructures give better electrode performance Figure 2-6(b). However, since concentration polarization increases with increasing electrode thickness, the optimum microstructure of the electrode should be made as fine as possible to permit the use of moderate thickness of

cathodes to ensure that concentration polarization is not a limiting factor and simultaneously to obtain as low value of  $R_{ct}^{eff}$  as possible.

On the other hand, an inhomogeneous current distribution is expected when the number of contacts between the cathode and current collecting mesh and lead wire is insufficient, leading to higher in-plane electrode resistance as can be seen in Figure 2-7.<sup>35</sup> Thus, a porous current collecting layer of coarse grains on top of a thin cathode layer of fine grains was suggested for LT-SOFC.<sup>36</sup> This is the reason that the pure BRO7 current collector layer substantially influences the overall performance.

## **2.6. Infiltration or Impregnation Process**

A nano-structured cathode is theoretically an ideal microstructure possessing the advantages of high electrocatalytic activity and large TPB length. It has been reported that the nano-sized oxides improved the catalytic properties due to an increase in surface vacancy concentration, ionic and electronic conductivities.<sup>37-38</sup> Modeling studies show that larger TPB length is associated with smaller particles.<sup>39-40</sup> However, since SOFC cathodes require the structural integrity with adequate mechanical strength and stability at operating temperatures typically higher 500°C, the cathode entirely comprised of nano-structure may be not suitable. Thus, the nano-structure should be supported on a more robust micro-sized cathode backbone. The technique to construct this microstructure is called 'infiltration or impregnation.' Although the infiltration has been used in relatively recent years to improve performance of the SOFC electrodes, it attracted many research activities both experimentally<sup>41-49</sup> and theoretically through modeling studies.<sup>50-51</sup> Several reviews with different emphasis in this area are also available.<sup>52-54</sup>

The infiltration/impregnation technique involves depositing nanoparticles into a pre-sintered backbone. The sintering of backbone is normally performed at high temperature. Thus, mechanical bonding between the electrode backbone and the electrolyte is good enough to give the structural stability to the system. Moreover, sufficient percolation of each constituting phases ensures high effective conduction of electron or oxygen ion. On the other hand, the firing process for the deposition of nanoparticles and the formation of the desired phase can be conducted at temperatures much lower than that needed for the traditional ceramic fabrication process. For example, while the firing temperature of the traditional LSM–YSZ composites is usually higher than 1100°C,<sup>55</sup> the infiltration process requires only 800°C for the deposition of LSM on the YSZ backbone.<sup>46</sup> The low temperature fabrication brings about many advantages. Since the firing temperature is low, nanoscale characteristics of particles can be preserved, which is beneficial to achieving high catalytic activity and large TPB length. A modeling study showed that the TPB length in a cathode prepared by infiltration is much larger than that of the composite electrode prepared by the traditional ceramic mixing process.<sup>50</sup> In addition, the reaction between the MIECs and YSZ can be avoided since the firing temperature is low, making it possible to use these MIEC materials, which have high electrochemical performance, but high reactivity with YSZ electrolytes, as cathodes for SOFCs. The infiltration may also alleviate the thermal expansion mismatch. For cathodes fabricated by the infiltration process, the coefficient of thermal expansion (CTE) is mainly dominated by the backbone materials. Thus, infiltrating with a material of mismatched CTE has little effect on the overall CTE of the cathodes.

Figure 2-8 shows the schematic of the microstructures constructed by the infiltration method. Two types of nano-structures are possible since the electrode is usually a composite consisting of two phases, an electronic conducting phase and an ionic conducting phase. Infiltrating an electron conducting nano-sized electrocatalyst into an ion conducting backbone is one option or vice versa. For these two types of infiltration, depositing nanoparticles into the backbone not only increases TPB reaction sites for oxygen reduction, but also provides the pathway for charge transport. Another strategy is to infiltrate nanoparticles of the electrocatalyst and/or electrolyte into a mixed conducting backbone of composites comprised of both ionic and electronic conductors or of a single phase MIEC material. For this strategy, the infiltrated nanoparticles are not required to provide the function of charge transport though.

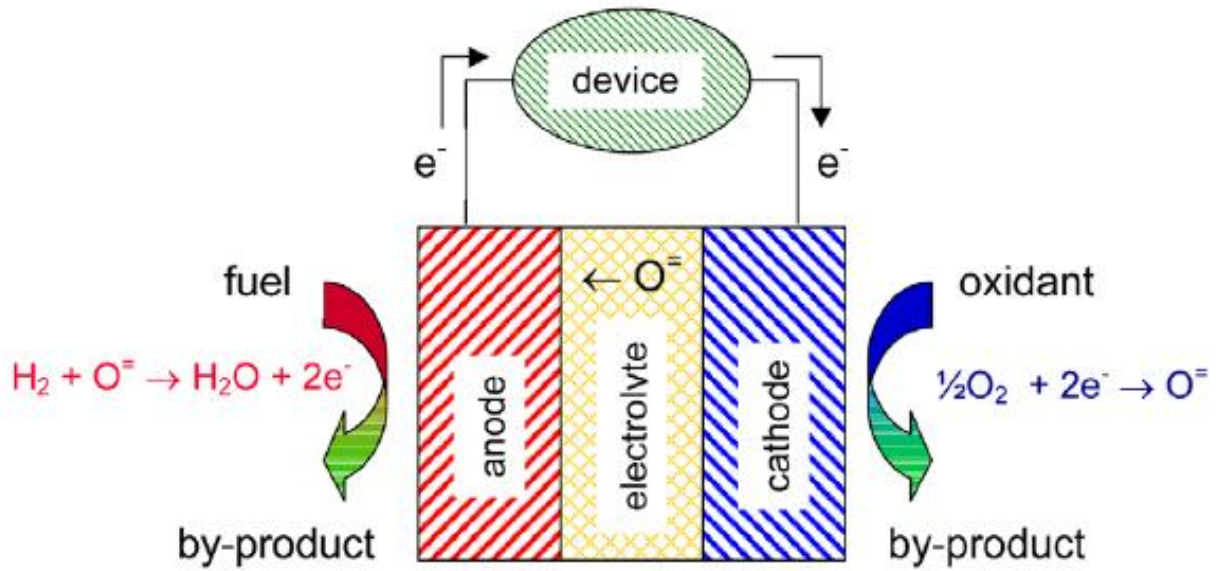


Figure 2-1. Schematic of a fuel cell, comprised of an anode, electrolyte, and cathode<sup>4</sup>

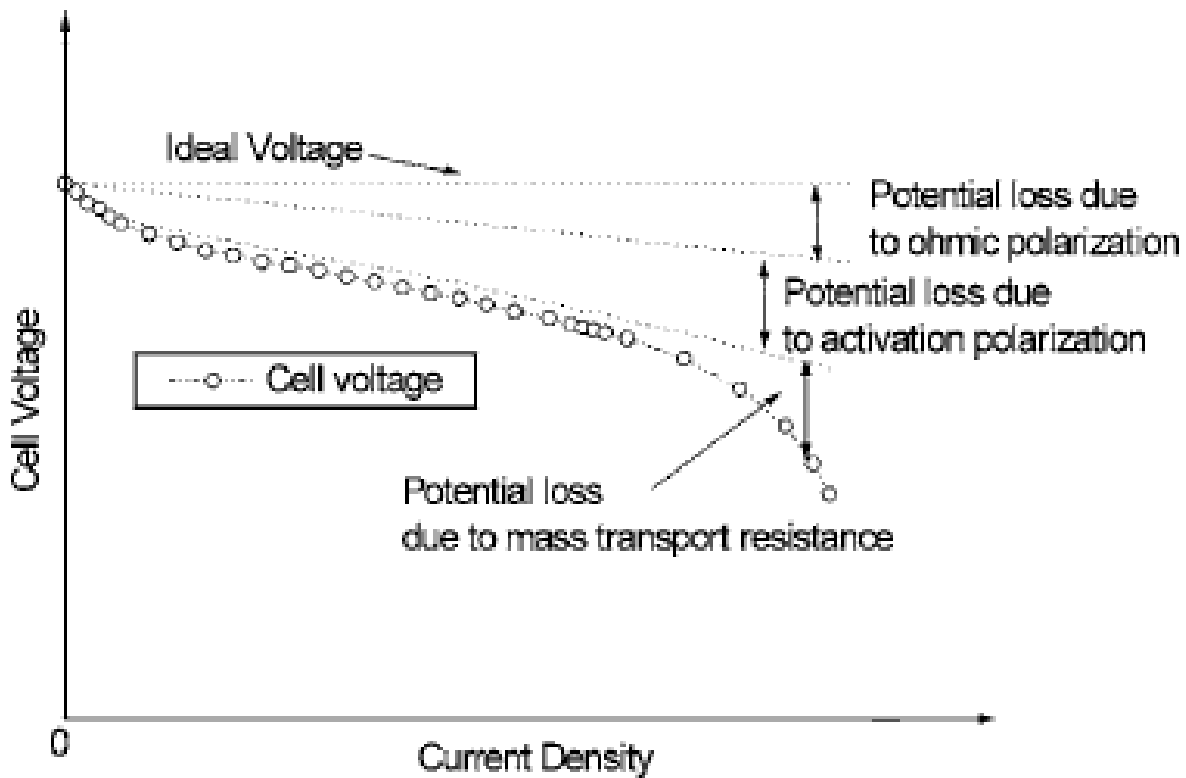


Figure 2-2. Schematic view of polarizations (or overpotentials) in a SOFC<sup>12</sup>

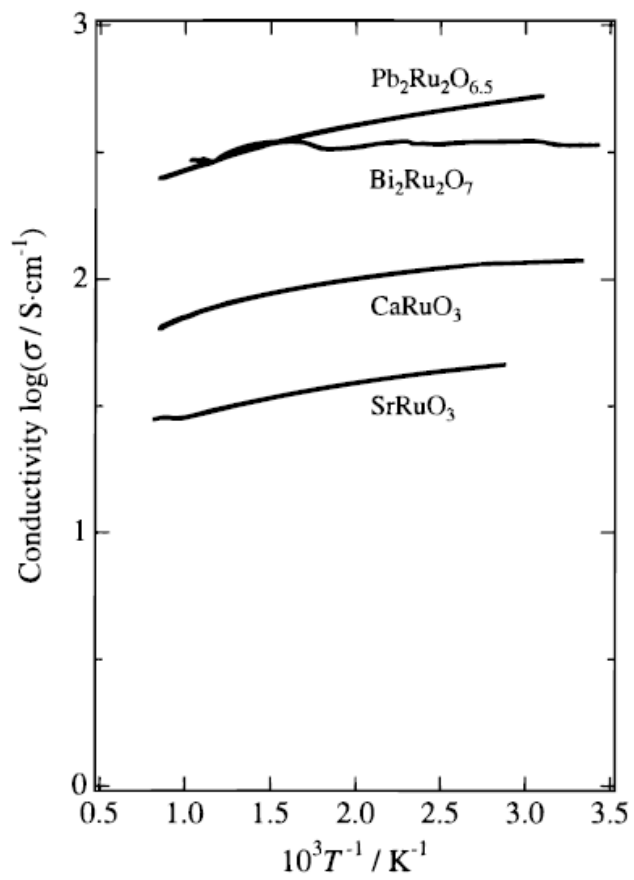


Figure 2-3. Temperature dependence of electrical conductivity for  $Pb_2Ru_2O_{6.5}$ ,  $Bi_2Ru_2O_7$ ,  $CaRuO_3$ , and  $SrRuO_3$ <sup>25</sup>

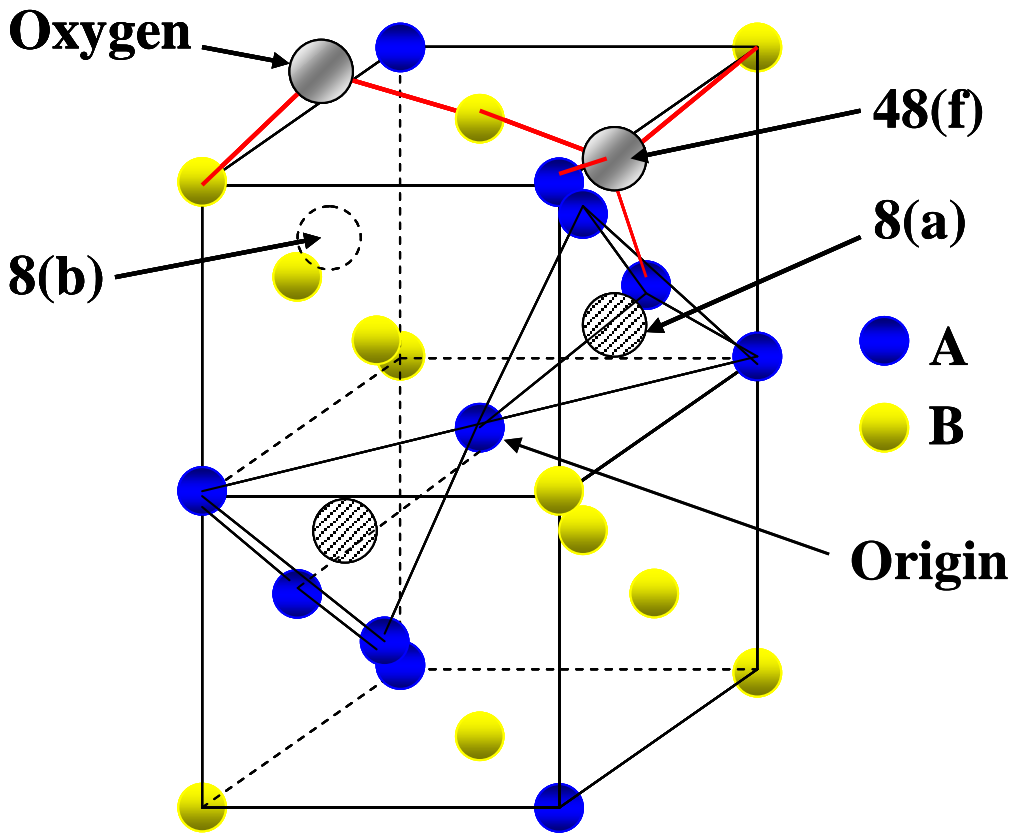


Figure 2-4. Successive two formula units out of a pyrochlore unit cell ( $A_2B_2O_6O'$ )

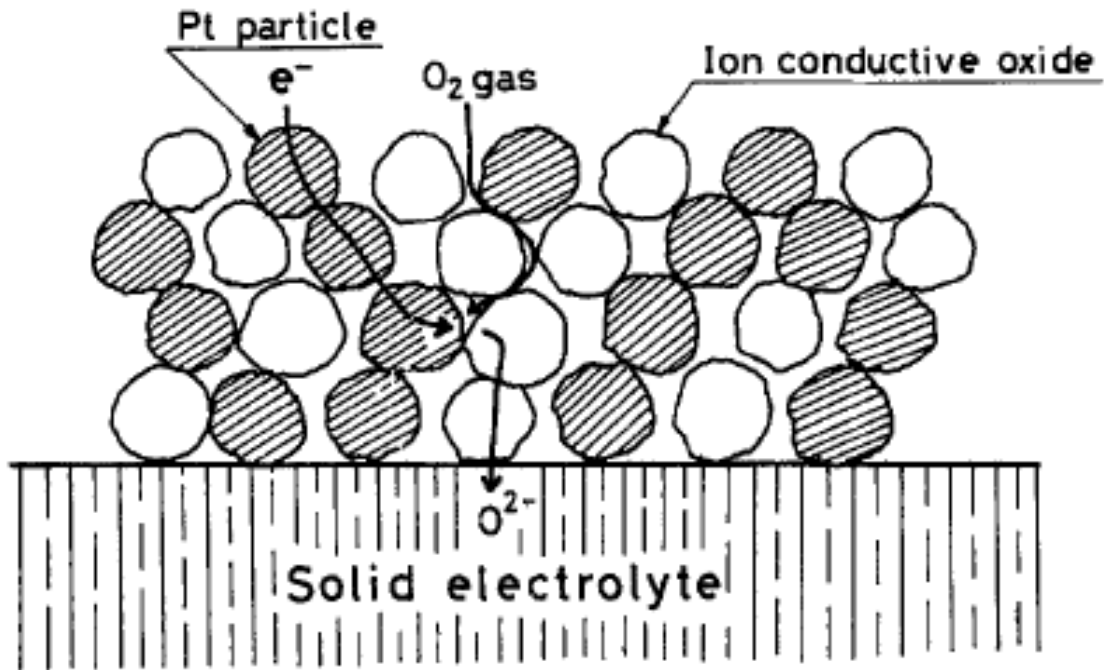


Figure 2-5. Composite cathode showing two parallel paths for oxygen species and electrons respectively<sup>33</sup>

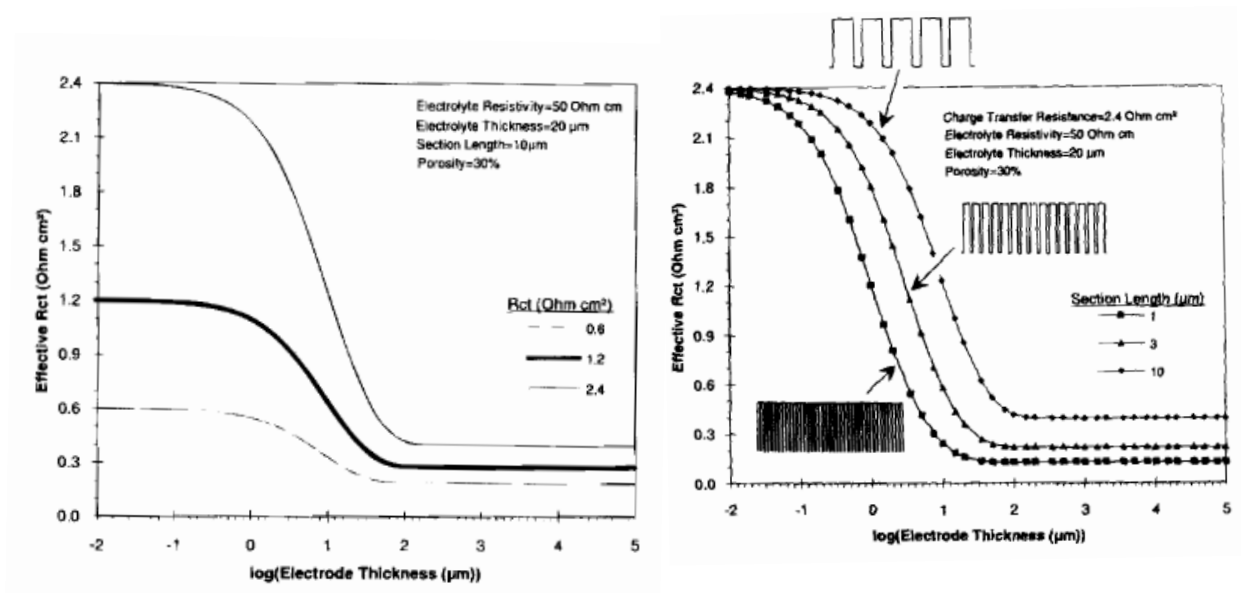


Figure 2-6. (a)  $R_{ct}^{\text{eff}}$  as a function of electrode thickness (b) The effect of finer structure on  $R_{ct}^{\text{eff}}$ <sup>32</sup>

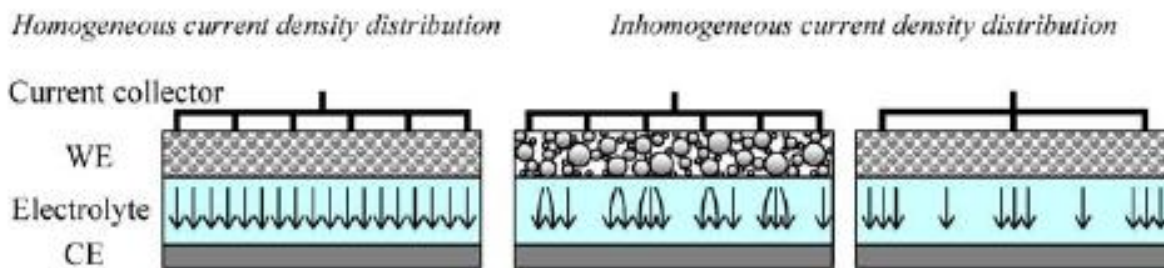


Figure 2-7. Schematic illustration of the current constriction effects for different cathode microstructure and current collector geometry<sup>35</sup>

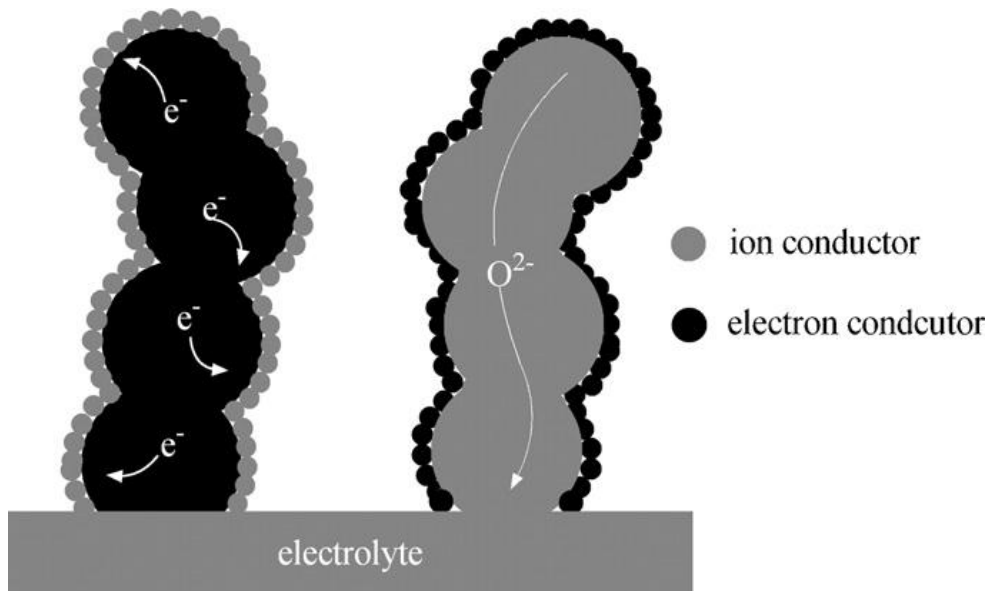


Figure 2-8. Schematic of the microstructure derived by two types of infiltration strategy. (left: ionically conducting nanoparticles with electronically conducting backbone, right: electronically conducting nanoparticles with ionically conducting backbone)<sup>56</sup>

CHAPTER 3  
SYNTHESIS OF A NANO-SIZED PYROCHLORE BISMUTH RUTHENATE,  $\text{Bi}_2\text{Ru}_2\text{O}_7$ ,  
USING GLYCINE-NITRATE COMBUSTION (GNC) FOR LT-SOFC CATHODE  
APPLICATION

**3.1. Introduction**

Transition metal oxides with a pyrochlore structure described as  $\text{A}_2[\text{Ru}_{2-x}\text{A}_x]\text{O}_{7-y}$ , where  $\text{A}=\text{Pb}$  or  $\text{Bi}$ ,  $0 \leq x \leq 1$ , and  $0 \leq y \leq 0.5$ , have been actively investigated as potential electro-catalysts or electrode materials for batteries, sensors, and fuel cell applications over several decades due to their high catalytic activity towards oxygen reduction and/or evolution, as well as relatively high electronic conductivity with metallic behavior ( $> 300 \text{Scm}^{-1}$ ) at targeted temperatures.<sup>57-61</sup> More recently, these ruthenium pyrochlores have drawn attention as a promising cathode material for intermediate or low temperature solid oxide fuel cell (SOFC) applications ( $600\text{-}800^\circ\text{C}$  and  $<600^\circ\text{C}$ , respectively).<sup>23-26, 62</sup> Among them, in particular, bismuth ruthenate is more of interest because of its better stability and less toxicity than lead ruthenate at temperature range of  $500\text{-}700^\circ\text{C}$ .<sup>26</sup> There exists two representative bismuth ruthenates, i.e.  $\text{Bi}_2\text{Ru}_2\text{O}_7$  (BRO7) and  $\text{Bi}_2\text{Ru}_2\text{O}_{7.3}$  (or  $\text{Bi}_3\text{Ru}_3\text{O}_{11}$ ) in ambient atmosphere depending on the temperatures. Low temperature bismuth ruthenate  $\text{Bi}_2\text{Ru}_2\text{O}_{7.3}$  with cubic structure transforms irreversibly to high temperature pyrochlore  $\text{Bi}_2\text{Ru}_2\text{O}_7$  beyond  $950^\circ\text{C}$ .<sup>63-64</sup> Even though there is some discrepancy regarding the transition temperature, it is obvious that high temperature pyrochlore BRO7 is difficult to form at temperature below  $900^\circ\text{C}$ . In general, as a result, high-temperature pyrochlore BRO7 is synthesized using solid state (SS) reaction where the appropriate amounts of constituting oxides ( $\text{RuO}_2$  and  $\text{Bi}_2\text{O}_3$ ) for the final composition ( $\text{Bi}_2\text{Ru}_2\text{O}_7$ ) are mixed and heated to over  $900^\circ\text{C}$  for several tens of hours for long-range diffusion among reactants. Thus, the resulting

powder contains particles of several microns in size due to grain growth inherent from long period of high temperature heat treatment.<sup>25, 63</sup> Several extra processing steps such as ball-milling and vibro-milling etc are required to further break up the micron-sized particles into the submicron range. Accordingly, this conventional SS reaction route is not suitable for producing a nano-sized powder.

On the other hand, it was recently reported from our group that ASR values as low as  $0.03\Omega\text{cm}^{-1}$  and  $0.73\Omega\text{cm}^{-1}$  at  $700^\circ\text{C}$  and  $500^\circ\text{C}$ , respectively, can be achieved for an optimized size combination of BRO7-ESB composite cathodes where very fine particle size of BRO7 was prepared by SS reaction route with multiple extra processing steps such as vibro-milling, sonication, and sedimentation.<sup>10</sup> However, it should be pointed out that the yield ratio to get those fine particles ( $<100\text{nm}$ ) of BRO7 was prohibitively low. Therefore, the processing route attempted above is not an effective fabrication method for mass production.

Contrary to the conventional SS reaction route, wet-chemical synthesis methods such as Pechini-type citrate route, sol-gel route,<sup>65-66</sup> co-precipitation route,<sup>67</sup> and glycine-nitrate combustion (GNC) route<sup>68-69</sup> etc require relatively lower processing temperature, thanks to more intimate (molecular level) mixing between reactants. That is, the nucleation process takes place through the rearrangement and short-distance diffusion of nearby atoms and molecules, not long-distance diffusion, which normally happens with conventional SS reaction route. As a result, more fine and homogeneous powder with large specific surface area can be achieved with wet-chemical synthesis routes. Among these, GNC route was specifically chosen in this study to synthesize nano-sized pyrochlore BRO7 since GNC route has to date never been reported for

BRO7 synthesis, while there have been several attempts to prepare submicron BRO7 through co-precipitation<sup>70</sup> and sol-gel routes.<sup>66</sup> GNC allows for very short reaction times, which is a characteristic inherent from combustion, and the gas by-products (CO<sub>2</sub>, N<sub>2</sub>, or H<sub>2</sub>O) produced during the reaction partially prevent the particles from agglomerating so that the development of nano-sized powders is plausible even though the reaction temperature could be as high as ~1400°C.<sup>69</sup>

In this work, glycine-to-nitrate (G/N) ratio was carefully examined to determine the optimum ratio for better crystallinity and phase purity of BRO7. Also, calcining temperature and duration were controlled to get the smallest nano-sized particle as possible. Such synthesized BRO7 was mixed with erbia-stabilized bismuth oxide (Er<sub>0.4</sub>Bi<sub>1.6</sub>O<sub>3</sub>, ESB) to make a composite cathode and its electrochemical performance was compared to that of the conventionally made BRO7-ESB cathodes reported previously from our group to examine the feasibility of GNC route for BRO7 nanoparticle synthesis. The increased triple-phase-boundary (TPB) reaction sites in BRO7-ESB composite cathode arising from more contacts between nano-sized BRO7 and micron-sized ESB were expected to improve electrochemical performance, which was evidenced already for composite cathodes consisting of vibratory milled BRO7 (VM BRO7) and SS route ESB (SS ESB) in the previous study from our group.<sup>10</sup>

## **3.2. Experimental**

### **3.2.1. GNC Bi<sub>2</sub>Ru<sub>2</sub>O<sub>7</sub> Synthesis**

The synthesizing process is outlined in flowchart in Figure 3-1. Metal nitrates are employed as oxidizing agents while the glycine plays roles as both a chelating agent for metal cations (Bi<sup>3+</sup> and Ru<sup>4+</sup> in this case) and a fuel, i.e. reducing agent. Stoichiometric amount of Ru((NO)(NO<sub>3</sub>)<sub>3</sub>)<sub>3</sub> (Ru 31.3% min, Alfa Aesar) and Bi(NO<sub>3</sub>)<sub>3</sub>·xH<sub>2</sub>O (Puratronic®

99.999%, Alfa Aesar) for the final BRO7 were dissolved separately in de-ionized (DI) water to form an aqueous solution. The solution was then added to the glycine solution where varying amounts of glycine in the solid state were dissolved in DI water as determined by the required glycine-to-nitrate (G/N) ratio. The whole solution was then stirred for 1 hr on a hot plate at 80°C for better mixing. Next, the hot plate was heated to 120°C for water evaporation. Once water is entirely evaporated, the solution becomes viscous gel. Upon further heating of the hot plate to 250~300°C, spontaneous, exothermic autoignition (combustion) begins and ends rapidly within 3s, yielding a porous and foamy black ash of BRO7 precursor. As-prepared materials were then ball milled in ethanol for 24 hrs using YSZ grinding media and dried on a hot plate with stirring to break up any aggregates inside the precursor before calcination, The dried precursors were further calcined at temperatures over 600°C for 2hrs in the open air to remove any residual carbonates and unreacted phases.

### **3.2.2. Cell Fabrication**

ESB powder was obtained using conventional SS reaction synthesis and then crushed by mortar and pestle and sieved (325 Mesh). ESB electrolyte pellets were prepared with 3.0 g of these solid-state powders by uniaxial pressing (approximately 12 Kpsi) in a half-inch die followed by isostatic pressing (250 MPa). These green bodies were then fired at 890 °C for 15 hrs. The sintered pellets had densities 94%±2% of theoretical with 1.11 cm ±0.02 cm in diameter and 0.3 cm ±0.01 cm in thickness. Cathode inks were prepared by combining organic vehicles with the mixture of BRO7 and ESB powders (50-50 wt%) in appropriate ratio for 35~40vol% of porosity in the final cathode after sintering. The inks were applied to both sides of the ESB electrolyte substrates by paint-brushing to make symmetrical cells. These cells were dried at

120°C for 1 hr, and sintered at 800°C for 2 hrs. Pure BRO7 powder was separately mixed with organic vehicles and applied on top of the cathodes as a current collector.

The active cathode area, where the cathode ink was applied (the top or bottom surface area of the electrolyte), was 0.97cm<sup>2</sup>.

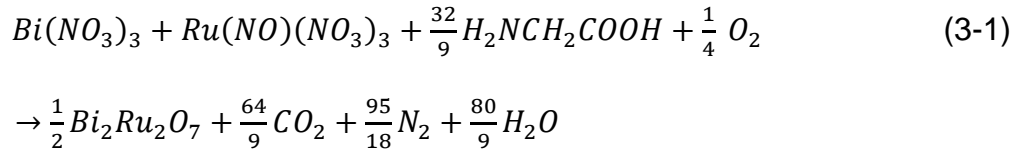
### **3.2.3. Characterization**

X-Ray Diffraction (XRD) patterns of several precursors and powders were recorded with a Philips APD 3720 diffractometer using  $\lambda K\alpha(\text{Cu}) = 1.5406 \text{ \AA}$  to determine phase formation, purity, crystallinity, and approximate crystallite size. Step scans were taken over a range of  $2\theta$  angles, 20°~80°, with 0.02° step scan and 0.5sec/step. The particle size was estimated by a JEOL TEM 200CX transmission electron microscope (TEM). The evaluation of morphology and microstructure of cathode system was carried out with the aid of JEOL JSM 6400 scanning electron microscope (SEM). Energy Dispersive Spectrum (EDS) was also used to analyze the composition of the BRO7 powders. Particle size distribution was analyzed with TSI PSD 3603 (Aerosizer) from Ahmherst Process Instrument Co. Inc. to better understand behavior of particles such as agglomeration. Thermogravimetric and differential thermal analysis (TG/DTA) was performed on the final BRO7 powder (calcined at 700°C 2hrs) using Mettler-Toledo TGA/DTA instrument to examine the stability of the phase at temperature range of 25~1000°C. In addition, two-electrode Electrochemical Impedance Spectroscopy (EIS) was measured on GNC BRO7-SS ESB composite cathodes deposited on both sides of ESB electrolyte pellet using Solartron 1470E frequency response analyzer in standalone mode for unbiased testing with frequency range of 0.1MHz to 0.01Hz and AC voltage amplitude of 100mV.

### 3.3. Results and Discussion

#### 3.3.1. The Effect of Glycine to Nitrate (G/N) Ratio on Bi<sub>2</sub>Ru<sub>2</sub>O<sub>7</sub> Synthesis

According to the propellant chemistry,<sup>71</sup> the maximum heat during combustion is obtained when the net oxidizing valency of metal nitrates is equal to the net reducing valency of fuel. In the case of GNC route, hydrogen and carbon can be considered to be reducing agents with valency of +1 and +4, respectively, whereas oxygen is regarded as an oxidizing agent with a valency of -2 and nitrogen is assumed to have a valency of zero.<sup>68</sup> In addition, for BRO7, Bi and Ru can be assumed to have valency of +3 and +4, respectively. With these valency values, the stoichiometric redox reaction can be calculated as follows:



GNC route produces N<sub>2</sub>, H<sub>2</sub>O, and CO<sub>2</sub> gases as by-products in addition to BRO7 precursor. The optimum G/N ratio, which can generate the maximum reaction heat, was found to be about 0.6 based on the calculation above. Five different G/N ratios (0.4, 0.6, 0.8, 1.0, and 1.2) were chosen in this study for BRO7 synthesis to evaluate the effect of G/N ratio on the crystallinity and particle size of BRO7 precursor. As seen in Figure 3-2, BRO7 precursors become more crystalline from amorphous as G/N ratio is varied from 0.4 to 1.2 even though the best crystallinity is expected to appear at G/N=0.6 based on the maximum reaction heat calculated above. This could be attributed to the presence of abundant oxygen gas from the environment so that more reducing agent, i.e. glycine, is required to generate the maximum heat, which is in turn evidenced as better crystallinity for G/N ratios above 0.6. However, the best peak pattern similar to pure

BRO7 was achieved at G/N=1.0 with less impurity phases such as unreacted Bi<sub>2</sub>O<sub>3</sub>, Ru and/or RuO<sub>2</sub>. Therefore, G/N ratio of 1.0 was selected for further study of phase evolution according to calcining conditions and microstructural analysis on the final powder. Figure 3-3 shows the effect of further heat treatment on the phase purity of BRO7 precursor. In the preliminary study, it was found that time duration doesn't play a critical role in phase evolution. BRO7 precursor calcined at 700°C for 2hrs exhibited almost the same XRD peak pattern as the one calcined at 700°C for 10hrs. The only difference was the peak sharpening of BRO7 calcined at 700°C for 10hrs due to its grain growth. Thus, the duration was fixed at 2hrs for this study while the calcining temperatures were varied from 600-900°C at 100°C interval. As calcining temperature increased, the crystallinity increased accordingly. Pure BRO7 phase was achieved even at 700°C for 2hrs, which is much lower compared to the 900°C for tens of hours necessary for the formation of pure BRO7 with conventional SS route.<sup>10</sup> Impurity phases such as unreacted Bi<sub>2</sub>O<sub>3</sub> was totally removed beyond 700°C.

### 3.3.2. Particle Size Analysis

The size of BRO7 crystallites obtained after 700°C-2hrs calcining was estimated using the Scherrer's equation<sup>72</sup> from X-ray line broadening of several peaks as follows:

$$D = \frac{0.9\lambda}{B \cos \theta} \quad (3-2)$$

where D is the average particle size in nm,  $\lambda$  the wavelength of X-ray used (Cu K $\alpha$  radiation, 0.15406nm, in this case), B the width in radian at half maximum intensity (called full width half maxima (FWHM)), and  $\theta$  the Bragg diffraction angle of the line.

The true B value can be calculated from the following equation:

$$B^2 = B_M^2 - B_S^2 \quad (3-3)$$

Where  $B_M$  is the measured full width at half maximum intensity and  $B_S$  is the full width at half maximum intensity of standard silicon. The calculated values for several main peaks and average crystallite size are given in Table 3-1. The average crystallite size of ~24nm in diameter was achieved for BRO7 calcined at 700°C for 2hrs. TEM images of BRO7 calcined at 700°C for 2hrs (Figure 3-4) also confirmed that crystallites in size range of 20~40nm were actually formed.

However, it should be pointed out that the resulting particles tend to aggregate during calcination, which was evidenced with SEM image as shown in Figure 3-5. From SEM image, the aggregated particles seemed to be distributed in size of 200~400nm, which was also confirmed by particle size distribution analysis (Figure 3-6). Peak position of particle distribution was ~360nm in diameter, thus most of particles seemed to aggregate and behave as polycrystalline particles rather than single crystal. However, this size range is still much smaller than that of the conventionally made one. For example, the particle size of vibro-milled (VM) SS BRO7 for 7 days was reduced from ~1.31 $\mu$ m of as-prepared SS BRO7 to ~0.73 $\mu$ m, which is still about two times larger than that of GNC BRO7 particles and contains a small number fraction but significant volume fraction of large, unbroken particles.<sup>10</sup>

On the other hand, EDS analysis on nanoparticles confirmed the formation of  $Bi_2Ru_2O_7$  (Figure 3-5).

Consequently, a nano-sized BRO7 was synthesized with reduced processing time. This was made possible thanks to both high reaction temperature (>900C°) and shorter reaction time (< 3s), a characteristic of GNC route, which is not possible with conventional SS synthesis and many other methods.

### 3.3.3. Phase Stability

Figure 3-7 shows TG plot obtained on the final BRO7 powder calcined at 700°C for 2hrs to see if there's any weight loss involved at temperature range of 25~1000°C. As can be seen, there was no weight loss detected at practical level up to 1000°C, indicating that the stability of the final BRO7 should be preserved at testing condition (500~700°C).

### 3.3.4. Electrochemical Performance

Electrochemical impedance testing was carried out on BRO7-ESB composite cathodes. The performance of this composite cathode was expected to be superior to composite cathodes comprised of SS BRO7-SS ESB and VM BRO7-SS ESB due to the expanded TPB reaction sites resulting from the smaller particle size of BRO7. Figure 3-8 shows typical Nyquist plots of GNC BRO7-SS ESB cathodes as well as Bode plots (a convenient graphical representation of impedance data for locating characteristic frequencies)<sup>73</sup> obtained at different temperatures (700~550°C) in air under open circuit potential. The plot is  $R_{el}$ -corrected for easy comparison (Figure 3-8 a). That is, the high-frequency real-axis intercept,  $R_{el}$ , is subtracted from the real component of each data point in spectra. In this way, the low-frequency intercept with the real-axis directly corresponds to the cathode polarization,  $R_p$ . Therefore, area specific resistance (ASR) of the cathode can easily be calculated by multiplying  $R_p$  by the electrode area (~0.96 cm<sup>2</sup> in this study) and dividing by 2 to account for the symmetrical cell. The high-frequency real-axis intercept,  $R_{el}$ , is known to mainly consist of the bulk electrolyte resistance, lead resistance, and contact resistance between the cathode and mesh current collector.<sup>10</sup> As expected, ASR increases as temperature goes down since the oxygen reduction reaction is thermally activated process.<sup>74</sup>

On the other hand, characteristic frequency is believed to be associated with the dominating electrochemical process. From the Bode plot in Figure 3-8 b, it can be noticed that the characteristic frequency (highest point of each spectrum in Bode plot) is changed from 10~1kHz at 700°C to <10Hz at 500°C, which is typically assumed to be related to oxygen adsorption (1~10Hz) and gas diffusion through the pores (<1Hz), respectively.<sup>55</sup>

To further examine whether the dominating process is affected by use of GNC BRO7 nanoparticles, the Bode plots of four different cathodes at 600°C were compared as shown in Figure 3-9. The characteristic frequencies of GNC BRO7-SS ESB, VM BRO7-SS ESB, and Sup BRO7-SS ESB were almost the same (5~6 Hz), indicating that the dominant electrochemical process was not changed among them. However, SS BRO7-SS ESB showed a little bit lower characteristic frequency (~1Hz). Since ESB for all of these cathodes was prepared with the same SS synthesis (SS ESB), the difference in characteristic frequency seemed to be caused by difference in BRO7 phase, that is, particle size depending on the synthesis routes. Although the difference in characteristic frequencies is not substantial, the extended TPT reaction sites and better percolation resulting from nano-sized BRO7 (VM, Sup, and GNC BRO7) are believed to influence on the dominating process.

In addition, Figure 3-10 is the Arrhenius plot of ASR for direct comparison between GNC BRO7- SS ESB in this study and the reported cathode systems.<sup>10</sup> As expected, ASR values of GNC BRO7- SS ESB were lower than those of SS BRO7-SS ESB and VM BRO7-SS ESB at examined temperatures due to the extended TPB sites as the

particle size of BRO7 is reduced. ASR values of all the BRO7-ESB composite cathodes compared are listed in Table 3-2 for better comparison among ASR values.

The activation energy of GNC BRO7- SS ESB cathode system was determined to be ~1.26eV, which is comparable to the previously reported values, 1.2~1.34eV<sup>9</sup> but higher than 1.02eV.<sup>10</sup> However, it should be mentioned that since the impedance semicircle at 500°C was incomplete due to delayed response at low temperature, the intercept difference (ASR) was estimated roughly with the instant fit (Zview software). Therefore, there should be some errors involved in calculation of ASR at 500°C. The ASR can be further improved by optimizing the composition of composite cathodes based on the effective medium percolation theory.<sup>10, 75</sup> Since BRO7 particles are a lot smaller than ESB particles, percolation and TPB length maximization can occur at non-equal volume fraction of each phase, considering the fact that the densities of BRO7 and ESB20 are approximately the same (8.92 and 8.96 g/cm<sup>3</sup>, respectively). Reduced processing steps and high yield of GNC synthesis route are expected to enable such further optimization, which is not possible with the conventional SS reaction route followed by laborious breaking-down steps.

### **3.4. Conclusion**

A nano-sized Bi<sub>2</sub>Ru<sub>2</sub>O<sub>7</sub> (BRO7) powder was successfully synthesized using glycine-nitrate combustion (GNC) route. Pure BRO7 phase was achieved upon calcining at 700°C for 2hrs with the average crystallite size of ~24nm in diameter. Even though the resulting powder tends to aggregate, resulting in overall 200~400nm size range, it still showed much smaller particle size than the one prepared by SS reaction route followed by extra milling steps such as vibro-milling and sonication for further

particle size reduction. The glycine-to-nitrate (G/N) ratio turned out to play a critical role in determining the reaction temperature and reaction duration, thus phase purity and particle morphology (particle size, shape, and agglomeration etc).

Composite cathodes of such prepared BRO7 with SS ESB (GNC BRO7-SS ESB) showed better electrochemical performance than SS BRO7-SS ESB and VM BRO7-SS ESB cathodes. ASR values of  $0.123\Omega\text{cm}^2$  at  $700^\circ\text{C}$  and  $4.59\Omega\text{cm}^2$  at  $500^\circ\text{C}$  were achieved respectively, which follows well the trend of particle size effect on performance of composite cathodes. Additionally, the number of processing steps (thus time) was reduced by GNC route. In conclusion, it was demonstrated that GNC can be an effective synthesis route to produce nanoparticles of pyrochlore BRO7 and its composite cathode would be a potential candidate as a cathode material for LT-SOFC applications.

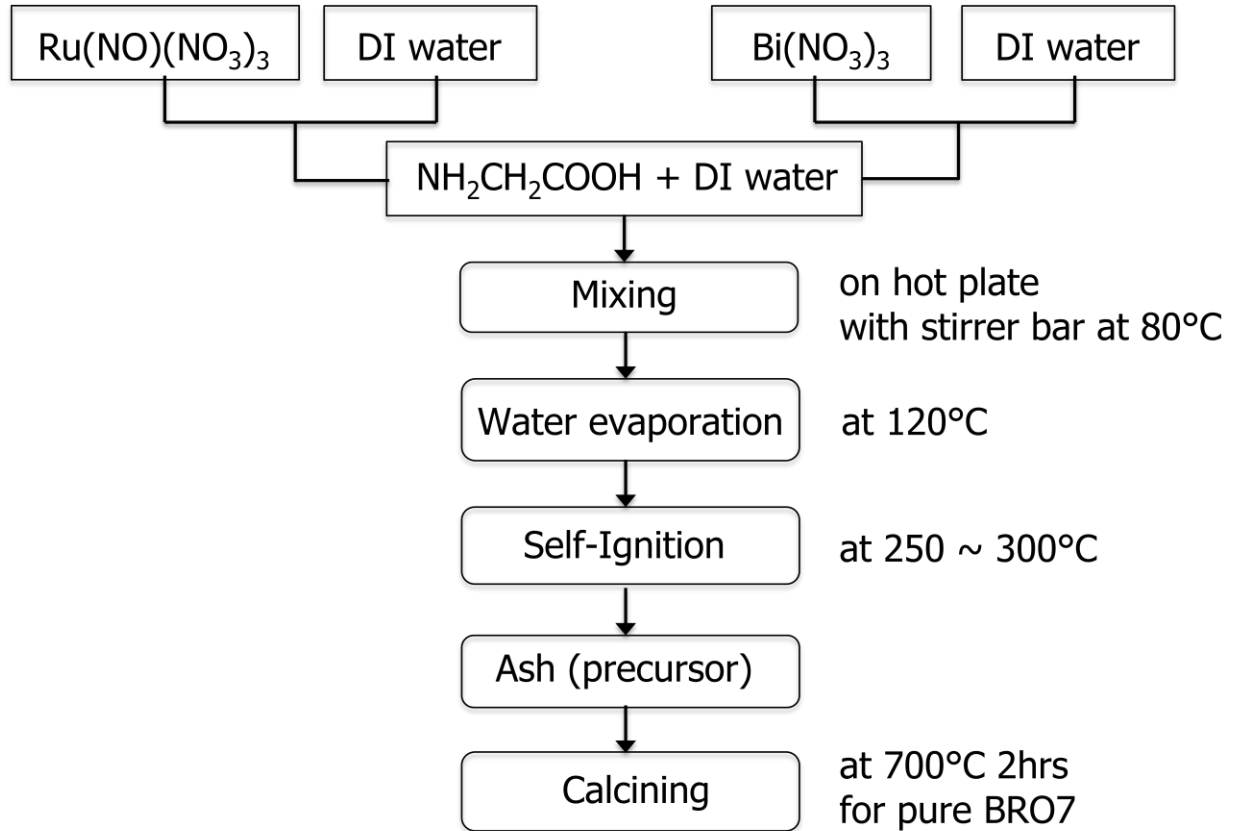


Figure 3-1. Flow chart of glycine-nitrate combustion (GNC) route for BRO7 synthesis

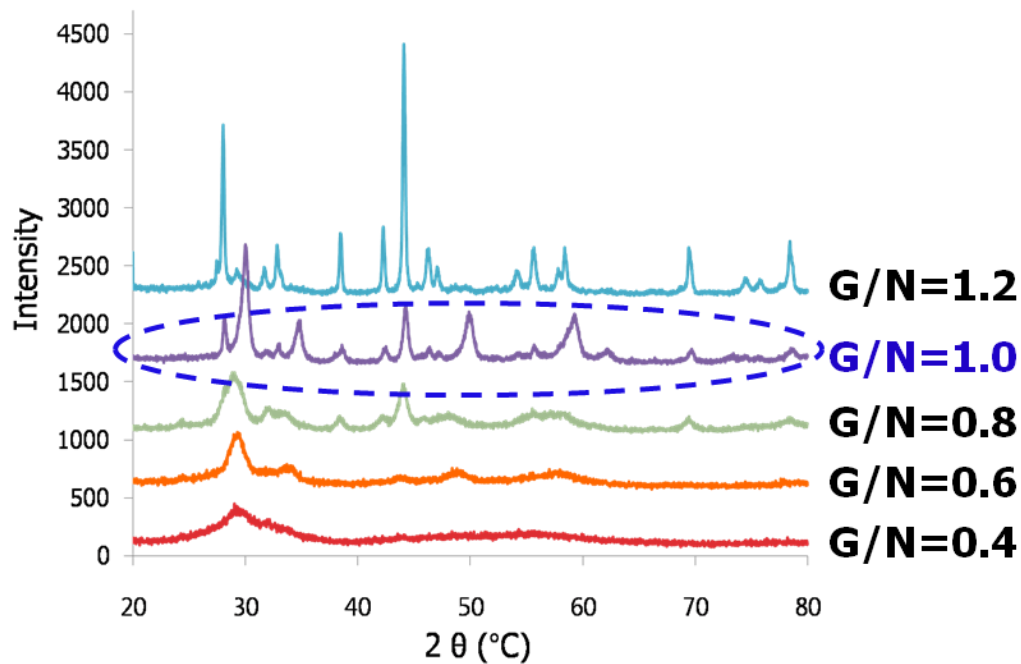


Figure 3-2. Effect of glycine to nitrates ratio (G/N) on the crystallinity of as-synthesized BRO7 precursors

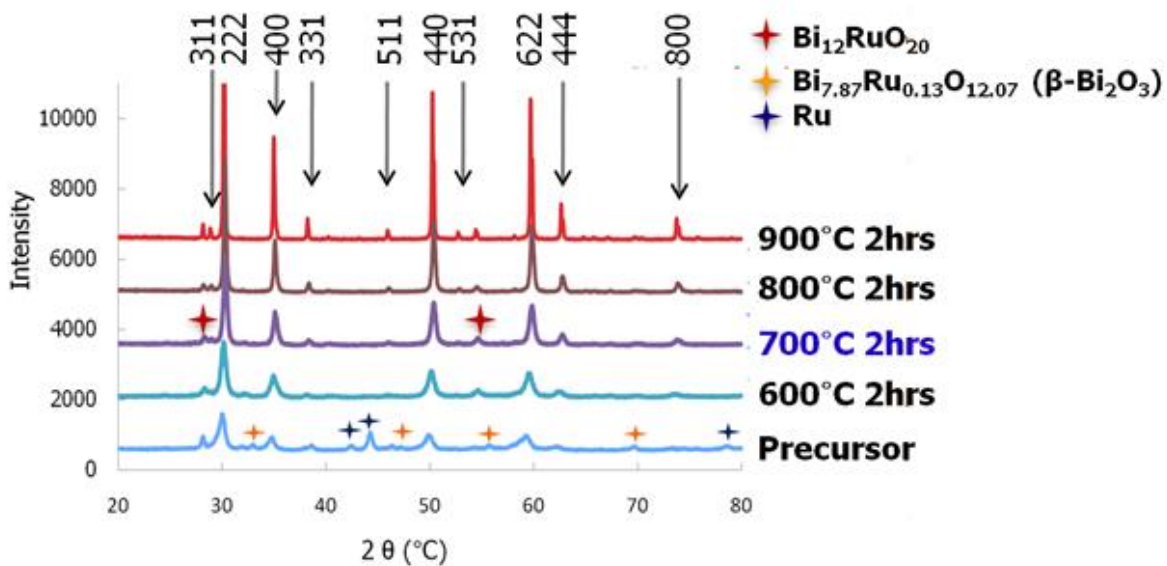


Figure 3-3. Evolution of high-purity BRO7 as a function of calcining temperature

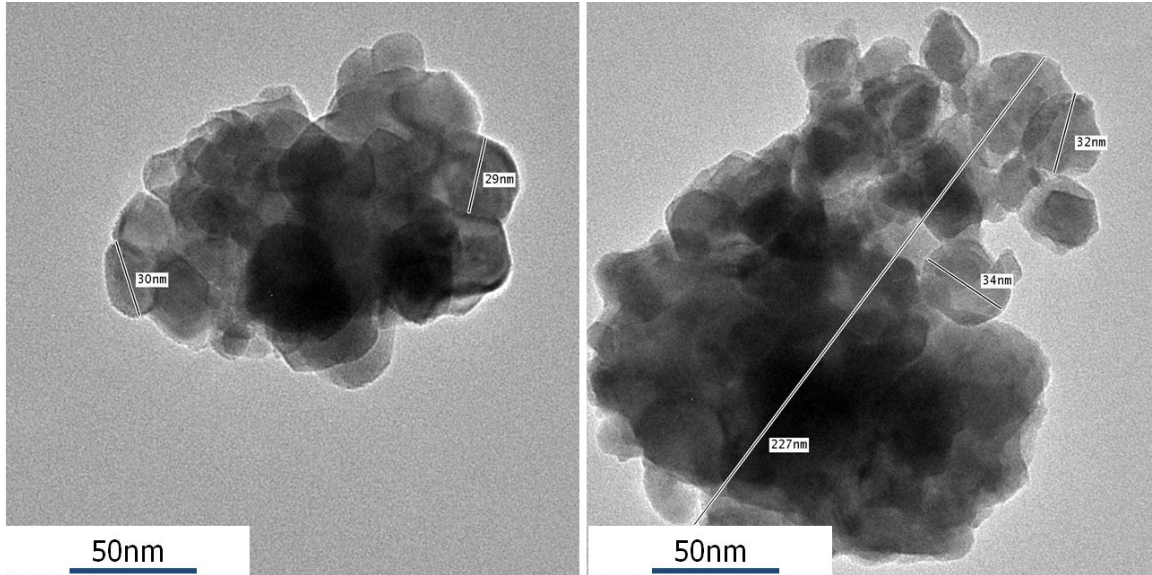


Figure 3-4. TEM images of BRO7 nanoparticles and aggregates of those taken from two different spots

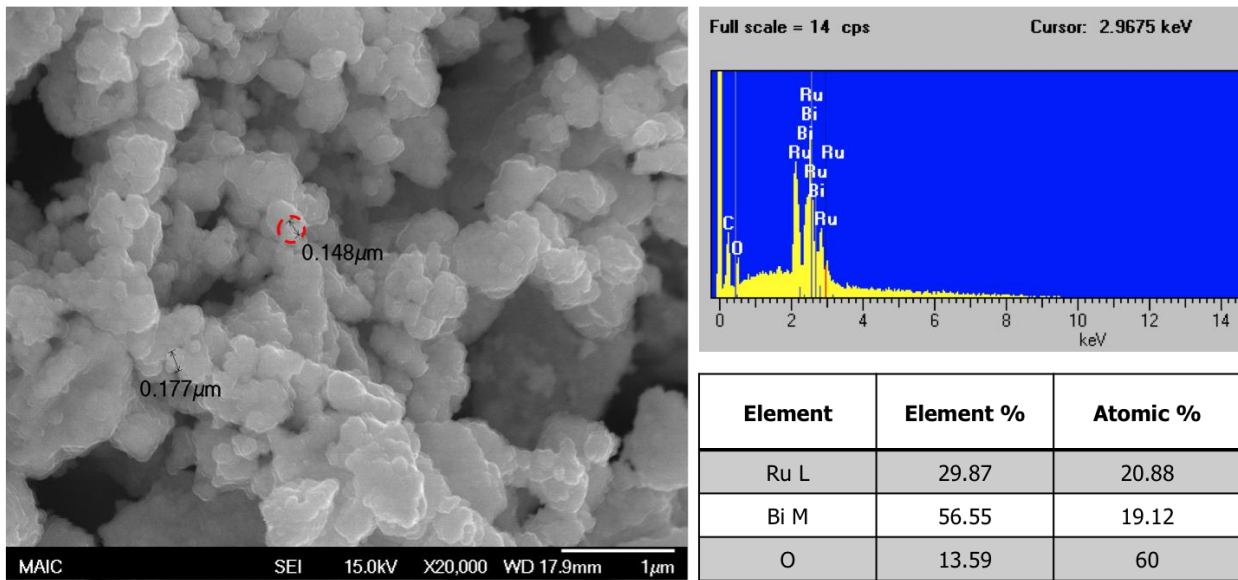


Figure 3-5. (Left) SEM image of BRO7 aggregates calcined at 700°C for 2hrs and (Right) Energy Dispersive Spectroscopy (EDS) analysis on the particle (red circle in the left figure)

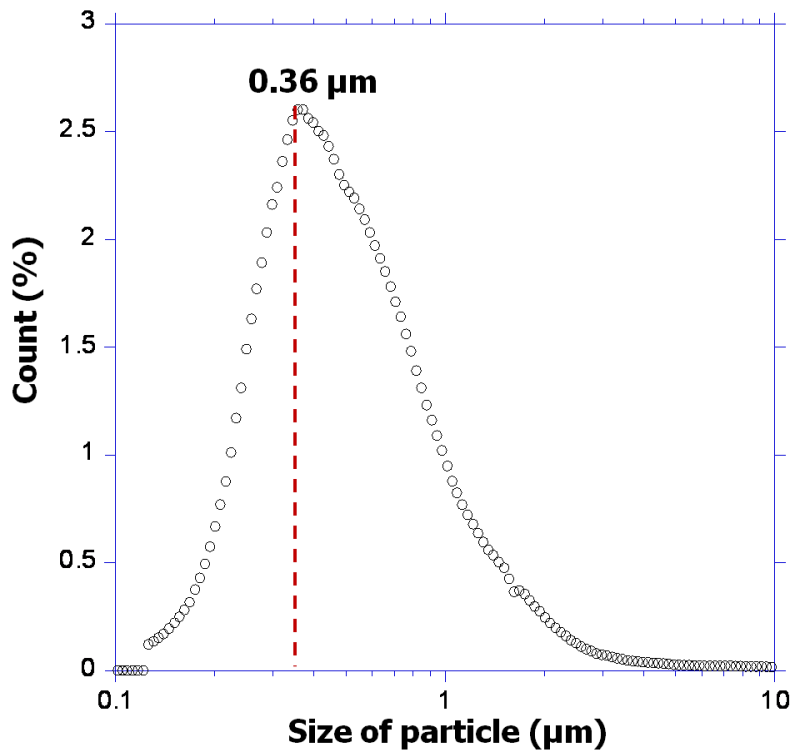


Figure 3-6. Particle size distribution of BRO7 particles measured by TSI PSD 3603 (Aerosizer)

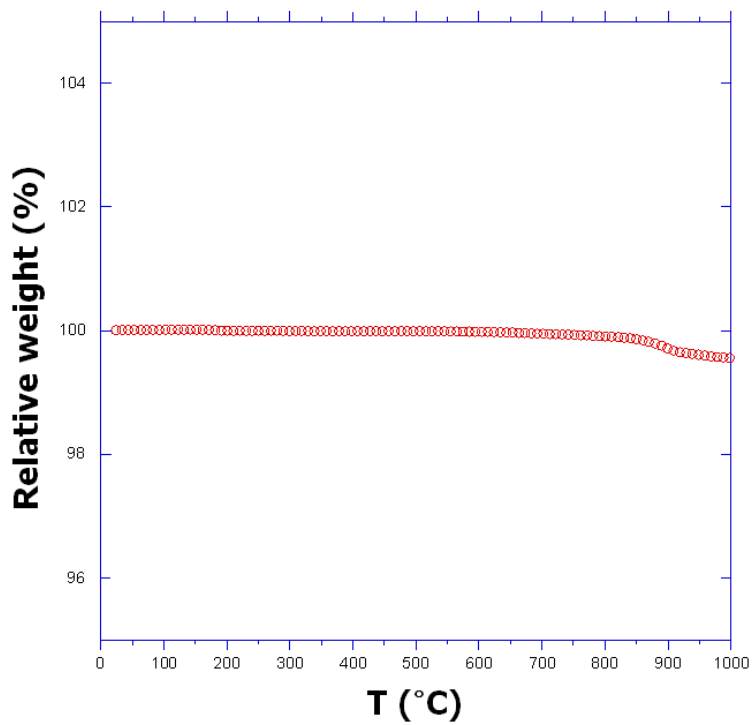


Figure 3-7. Thermogravimetric (TG) plot to show the stability of the final BRO7 calcined 700°C 2hrs powder at temperature range of 25~1000°C

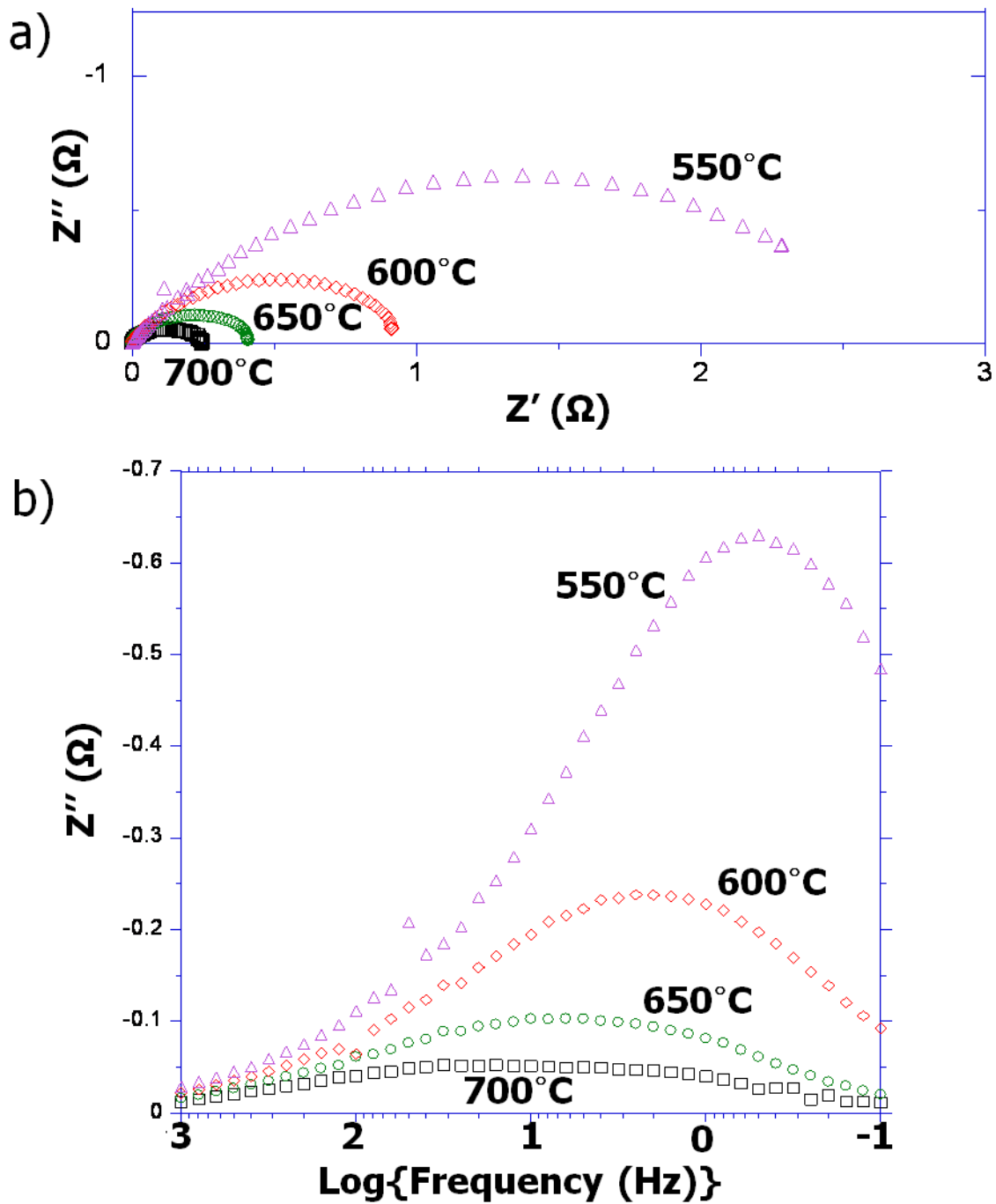


Figure 3-8. a) Nyquist and b) Bode plots as a function of temperature for GNC BRO7-SS ESB composite cathode tested in air

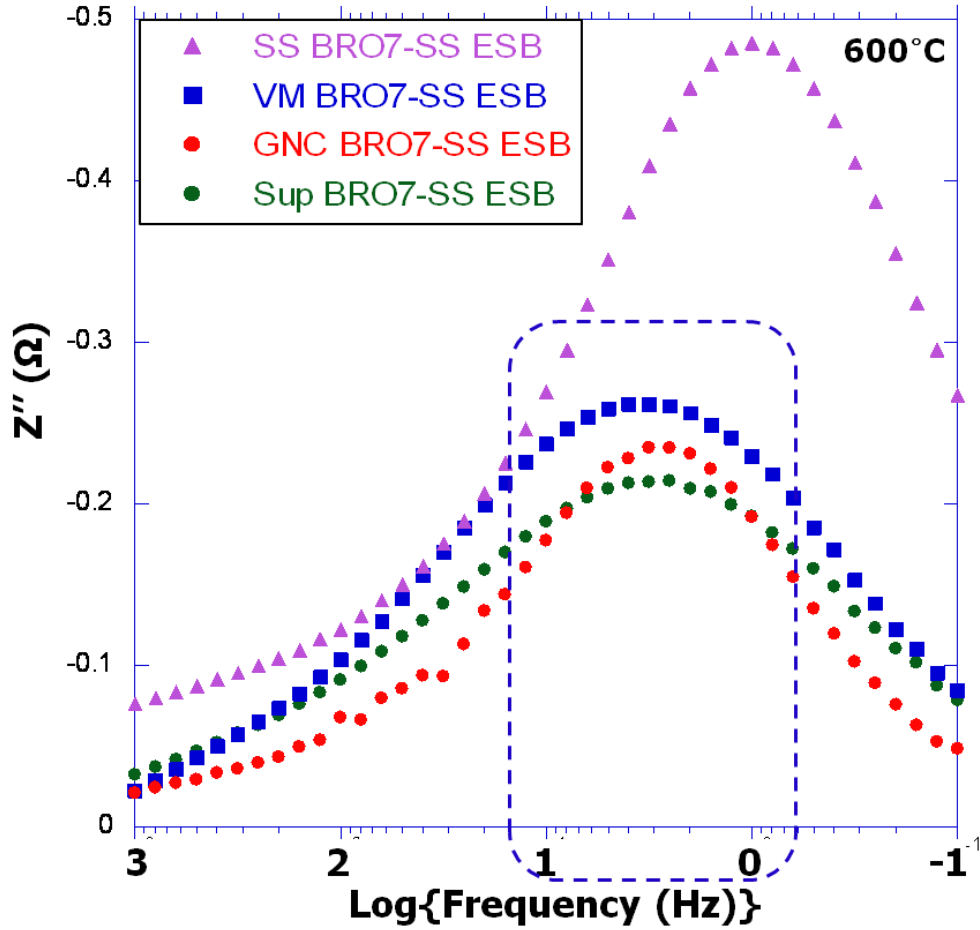


Figure 3-9. Overlapped Bode plots measured at 600°C of BRO7-ESB composite cathodes where the particle size of SS ESB is fixed whereas different processing routes were used for BRO7, resulting in different particle sizes. (VM: vibro-milled, Sup: sonication and sedimentation as described in ref.10) The data other than the one for GNC BRO7-SS ESB was extracted from ref.10

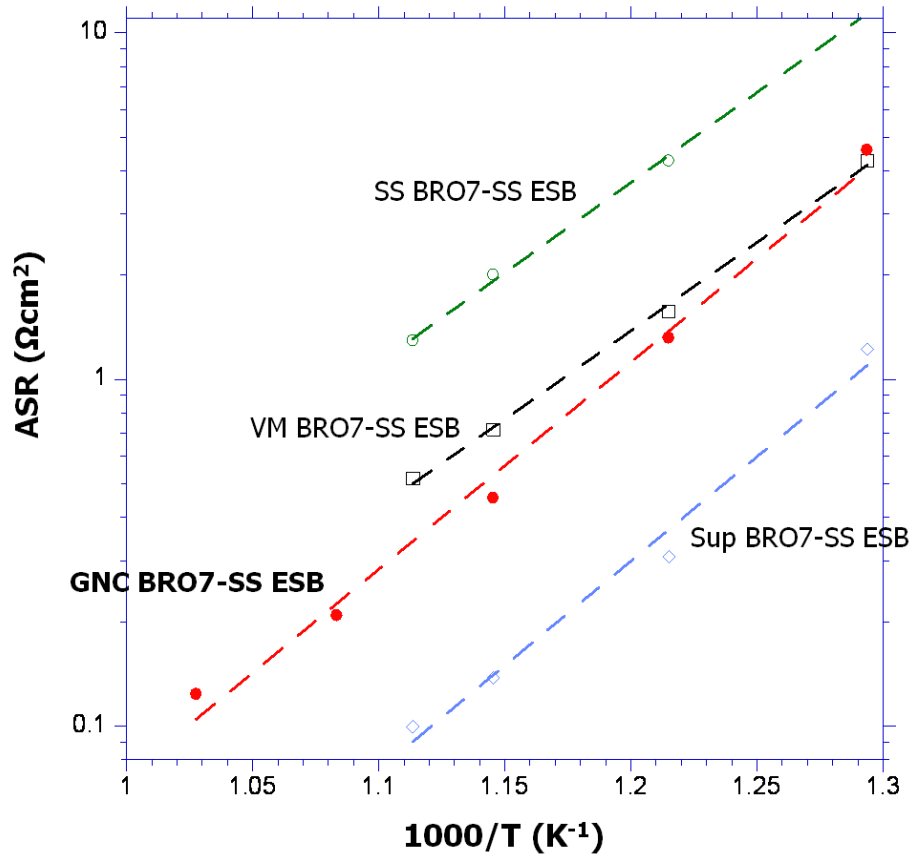


Figure 3-10. Arrhenius plot of ASR for comparison of GNC BRO7-SS ESB with the other BRO7-ESB composite cathodes reported (SS: prepared by solid state reaction route (~micron size), VM: SS+vibro-milling (700~800nm), Sup:SS+VM+sonication+sedimentation (<100nm) as described in ref.10)

Table 3-1. Crystallite sizes of pure BRO7 depending on  $2\theta$  using Scherrer's equation and its average

$2\theta$	FWHM	hkl	D (nm)	Strain (%)
30.239	0.368	222	31	0.58
35.059	0.460	400	23	0.62
50.280	0.457	440	25	0.42
59.713	0.493	622	23	0.37
62.643	0.472	444	25	0.33
73.756	0.642	800	18	0.37
Average			24.13	
95% confidence interval		20.01<	24.13	<28.26

Table 3-2. ASR values of all BRO7-ESB composite cathodes compared at each temperature measured

Cathodes	ASR( $\Omega\text{cm}^2$ ) at each temperature					
	700°C	650°C	625°C	600°C	550°C	500°C
SS BRO7-SS ESB <sup>10</sup>			1.29	2.00	4.27	11.55
VM BRO7-SS ESB <sup>10</sup>			0.52	0.72	1.57	4.28
GNC BRO7-SS ESB (in this study)	0.123	0.21		0.46	1.32	4.59
Sup BRO7-SS ESB <sup>10</sup>			0.23	0.35	0.92	2.80

## CHAPTER 4 SYNTHESIS OF IN-SITU COMPOSITE CATHODES OF BISMUTH RUTHENATE AND STABILIZED BISMUTH OXIDE FOR LT-SOFC

### 4.1. Introduction

Low temperature (LT)-solid oxide fuel cell (SOFC) operating at 650°C and below can reduce the cost of production by allowing cheaper and wider selection of materials such as stainless steel for interconnects and other structural components.<sup>76</sup> However, since decrease of operating temperatures usually causes an overall degradation of cell performance, high-performance cell components are required.<sup>77</sup> As the substantial reduction in the electrolyte ohmic resistance has been achieved by employing either thin-film technology or electrolyte materials with higher ionic conductivity such as gadolinia-doped ceria (GDC), the main focus of research is now primarily geared towards reduction of the electrode polarization, in particular, the oxygen reduction reaction in the cathode.<sup>78-79</sup>

It has proven that a composite cathode, consisting of an electro-catalyst with high electronic conductivity and an oxygen-ion conducting phase, can decrease the cathode polarization substantially by extending triple phase boundary (TPB) reaction sites from the electrode/electrolyte interface into the electrode. Moreover, adding ionic conductivity to the electrode provides additional path for transport of oxygen species to the cathode/electrolyte interface.<sup>6-7</sup> For example, it was recently reported from our group that ASR values as low as  $0.03\Omega\text{cm}^{-1}$  and  $0.73\Omega\text{cm}^{-1}$  at 700°C and 500°C, respectively, can be achieved for a optimized bismuth ruthenate ( $\text{Bi}_2\text{Ru}_2\text{O}_7$  or BRO7)- erbia stabilized bismuth oxide ( $\text{Bi}_{1.6}\text{Er}_{0.4}\text{O}_3$  or ESB) composite cathode where very fine particles of BRO7 were prepared by conventional solid state (SS) reaction route followed by multiple extra processing steps such as vibro-milling, sonication, and sedimentation.<sup>10</sup>

However, it should be pointed out that the yield ratio to get those fine particles (<100nm) of BRO7 was prohibitively low.

On the other hand, agglomeration of each constituting phase is often observed with the conventionally made composite cathodes during mixing and sintering process, which is deleterious to the overall cathode performance since the number of reaction sites will be reduced from the agglomeration of each phase.<sup>10</sup> In addition, percolation of each constituting phase is one of the most important issues to be considered when a composite cathode is made since only the effective oxygen ions transported to the interface between the electrolyte and electrode can contribute to the overall cathode performance.<sup>32, 75</sup>

One way to resolve the issues of both low yield of BRO7 nanoparticles from extra processing steps and agglomeration and percolation of each BRO7 and ESB phase mentioned above is proposed in this study, called in-situ composite synthesis, a new approach to synthesize a composite cathode through wet chemical based in-situ synthesis process. The concept is that nitrate solution of targeted cations (Bi, Ru) is employed to synthesize nanoparticles of one phase (BRO7 in this study) in situ on surface of the other phase (ESB in this study) while the other phase of powder (ESB) is dispersed and stabilized in aqueous solution through repulsive surface charge of the powder generated by adding a dispersant and controlling pH of the solution. Dispersing and stabilizing oxide materials in aqueous solution has been extensively studied in tape casting industry for various applications such as multilayer ceramic capacitors (MLCCs), varistors, inductors, resistors, and ceramic substrates etc.<sup>80-85</sup>

As a result, formation of BRO7 nanoparticles will be ensured because wet chemical route is employed (refer to chapter 3). Moreover, since nanoparticles of BRO7 are formed on surface of ESB particles, agglomeration of BRO7 nanoparticles will be prevented. Similarly, agglomeration of ESB particles is also expected to be suppressed by addition of a dispersant due to electrostatic repulsion between functional anions adsorbed on ESB particles in the solution state<sup>86-87</sup> and by formed BRO7 nanoparticles in the final dry state as well. Therefore, in this work, synthesis of in-situ composite cathodes of ESB-BRO7 was tried to get better percolation and less agglomeration of each constituting phase in the cathodes. The processing cost was also expected to be reduced since separate processes for each phase were not required, which normally happens for conventional composite synthesis route.

Dispersion behavior of ESB powder with/without a dispersant (ammonium citrate in this study) was carefully examined through zeta potential measurement to stabilize ESB powder in the aqueous solution. Then, (Ru, Bi) nitrates were added to the solution for final in-situ composite cathodes of BRO7-ESB using knowledge of wet chemical synthesis for BRO7 nanoparticles (refer to chapter 3).

Electrochemical performance of such prepared composite cathodes was compared to those of the conventionally made BRO7-ESB cathodes reported previously from our group to examine the feasibility of in-situ composite cathode synthesis route. Better percolation and less agglomeration of each BRO7 and ESB phase were expected to improve electrochemical performance.

## 4.2. Experimental

### 4.2.1. Stabilization of ESB Suspension

A parameter for characterizing degree of repulsive force, thus the stability of a suspension, is the zeta potential. In colloid science, a suspension having a zeta potential  $>130\text{mV}$  is considered to have sufficient repulsive force between particles to inhibit agglomeration.<sup>88</sup> Experimental zeta potential measurement of suspensions is most commonly carried out using electrophoretic light scattering (ELS) technique.<sup>89</sup> In this study, surface charge, thus zeta potential, of ESB was first carefully examined to find the optimum pH of the solution and the amount of a dispersant to be added for exceeding the zeta-potential requirement of  $>130\text{mV}$ , thus stabilizing ESB powder in the solution. To control pH of the solution, titration solution such as  $\text{HNO}_3$  and  $\text{NH}_4\text{OH}$  were employed. Also, ammonium citrate dibasic ( $\text{C}_6\text{H}_{14}\text{N}_2\text{O}_7$ , Fisher Scientific) was used as an anionic dispersant. Figure 4-1 shows the molecular structure of it.

### 4.2.2. Synthesis Process

The overall process of in-situ composite synthesis is outlined in Figure 4-2 for better understanding. First, ESB powder was obtained by a conventional solid state (SS) reaction and then crushed by mortar and pestle and sieved (325 Mesh). Such prepared ESB powder was then stabilized in de-ionized (DI) water based on zeta-potential measurement by controlling pH and adding ammonium citrate as a dispersant. Once stabilized ESB suspension was prepared, stoichiometric amounts of  $\text{Ru}(\text{NO})(\text{NO}_3)_3$  (Ru 31.3% min, Alfa Aesar) and  $\text{Bi}(\text{NO}_3)_3 \cdot x\text{H}_2\text{O}$  (Puratronic® 99.999%, Alfa Aesar) for the final  $\text{Bi}_2\text{Ru}_2\text{O}_7$  were separately dissolved in DI water and added into the ESB suspension. Cations such as  $\text{Bi}^{3+}$  and  $\text{Ru}^{4+}$  were expected to adsorb onto negatively charged functional anions of the dispersant ( $\text{COO}^-$  or  $\text{O}^-$ ) which are also

adsorbed onto surface of ESB particles in suspension due to specific adsorption of anions to the surface of ESB particles. The whole solution was then stirred for 30 min on a hot plate at 80°C for better mixing. After then, the hot plate was heated to 120°C for water evaporation. Once water is evaporated, the solution becomes viscous gel consisting of ESB particles surrounded by (Ru, Bi) oxides. Upon subsequent heating of the hot plate up to 250~300°C, weak self auto-ignition occurs, producing precursors of in-situ synthesized BRO7-ESB composites. As-prepared precursors were then ball milled in ethanol for 24 hrs using YSZ grinding media and dried on a hot plate with stirring to break up any aggregates inside the precursors before calcination. The dried BRO7-ESB composite precursors were calcined at 700~900°C for 2hrs to remove any residual carbonates and unreacted phases, resulting in in-situ BRO7-ESB powder.

On the other hand, ESB pellets were fabricated from SS ESB powder by uniaxial pressing (approximately 12 Kpsi) in a half-inch cylindrical die followed by isostatic pressing (250 MPa). These green bodies were then fired at 890 °C for 15 hrs, producing the final pellets with 1.11 cm  $\pm$ 0.02 cm in diameter and 0.3 cm  $\pm$ 0.01 cm in thickness.

Cathode inks were prepared by combining organic vehicles with in-situ BRO7-ESB powder in appropriate ratio for 35~40vol% of porosity in the final cathode after sintering. The inks were applied to both sides of the ESB electrolyte substrates by screen printing to make symmetrical cells. These cells were dried at 120°C for 1 hr, and sintered at 800°C for 2 hrs. Pure BRO7 powder was separately mixed with organic vehicles and applied on top of the cathodes as a current collector. The active cathode area, where the cathode ink was applied (the top or bottom surface area of the electrolyte), was 0.97cm<sup>2</sup>.

### 4.2.3. Characterization

Zeta potential was measured using ZetaPlus from Brookhaven Instruments and analyzed with PALS Zeta potential analyzer software ver.3.16. Smoluchowski model was applied to get values of the zeta-potential since  $ka \gg 1$  for ESB powder in DI water in this study, where  $k=1/\lambda$  ( $\lambda$ ; double layer thickness) and  $a$ =radius of particle.<sup>90</sup> X-ray diffraction (XRD) patterns of calcined composite powders were recorded with a Philips APD 3720 diffractometer using  $\lambda K\alpha(\text{Cu}) = 1.5406 \text{ \AA}$  to determine phase formation, purity, and crystallinity. Step scans were taken over a range of  $2\theta$  angles,  $20^\circ$ – $80^\circ$ , with  $0.02^\circ$  step scan and 0.5sec/step. Evaluation of particle size and microstructure of the cathode systems was carried out with the aid of a JEOL JSM 6400 scanning electron microscope (SEM). Impedance testing on symmetrical cells consisting of in-situ BRO7-ESB composite cathodes on ESB electrolyte was performed using a Solartron 1470E frequency response analyzer at open circuit potential over a frequency range of 0.01Hz to 0.1MHz with AC voltage amplitude of 50mV at temperatures of 550–700°C in air.

## 4.3. Results and Discussion

### 4.3.1. Zeta Potential of ESB Suspension

Figure 4-3 shows zeta potential profiles of ESB powder suspensions as a function of pH with and without a dispersant (ammonium citrate dibasic). For ESB suspension without ammonium citrate, the isoelectric point (IEP), point of pH where zeta potential becomes zero, was determined to be ~pH 3.1, which is very close to that obtained for  $\text{Bi}_2\text{O}_3$  from the literature.<sup>87</sup> Since  $\text{Bi}_2\text{O}_3$  is a base material for ESB and valence of Er is the same as that of Bi as +3, close values of IEP between ESB and  $\text{Bi}_2\text{O}_3$  appear reasonable. Zeta potentials of ESB suspension without ammonium citrate show

relatively low (<130mV) at all pH measured, indicating that charge repulsion between particles in the solution is not sufficient enough to stabilize the suspension.

On the other hand, as ammonium citrates were added to the suspension, potential curves were shifted to the lower pH side and, more importantly, to the more negative values because the surface layer of ESB particles becomes more negative due to adsorption of functional anions of the dispersant ( $\text{COO}^-$  or  $\text{O}^-$ ). Thus, suspensions can be stabilized from electrostatic repulsion between particles developed from overlap of the electric double layer in the solution. The IEP of ESB suspensions with ammonium citrates was estimated to be ~pH 1.9. Since the IEP of ESB suspension was changed before and after addition of ammonium citrates, there should be some interactions, called specific adsorption, between ESB particles and dispersants.<sup>91-94</sup>

Also, it can be noticed that 0.5wt% (relative to ESB powder) ammonium citrate made the suspension more negative than 1.0wt% ammonium citrate, indicating that 0.5wt% ammonium citrate can stabilize the suspension more effectively. This happens because the ionic strength of the solution becomes higher as the concentration of ions increases as follows:

$$I_c = \frac{1}{2} \times \sum C_i Z_i^2 \quad (4-1)$$

where  $C_i$  is the concentration of each ion and  $Z_i$  the valence of each ion present in suspension.<sup>90, 93</sup> Thus, double layer thickness ( $\lambda$ ) will shrink since it is inversely proportional to the ionic strength so that absolute zeta potential of suspension will be reduced, hence stability of the particles.

As a result, pH range of 5 with 0.5wt% of ammonium citrate was chosen as the optimized stabilizing condition for synthesis of in-situ composite cathodes since the zeta

potential of ESB suspension at this pH showed the maximum negative value (about -50mV), which is enough for effectively stabilizing ESB suspension. However, since pH of the suspension during in-situ composite synthesis is fluctuating due to the equilibrium reaction between  $H^+/OH^-$  ions and metal oxides' hydroxyl group, pH range of 5~7 was tried to be maintained by adding titration solution such as  $HNO_3$  and  $NH_4OH$ .

#### **4.3.2. Phase Purity of BRO7-ESB Composite and Formation of BRO7 Nanoparticles**

As can be seen in Figure 4-4, BRO7-ESB composites prepared by in-situ synthesis showed some extra peaks in XRD patterns other than peaks from each pure phase up to 800°C of calcining temperature. However, impurity phases were totally removed with calcination of 900°C for 2hrs. When compared to overlapped patterns separately obtained from each of pure ESB and BRO phase (top of the figure), XRD pattern of in-situ composites calcined at 900°C for 2hrs was matched well with those, indicating that BRO7-ESB composite phase was really formed by in-situ synthesis. No reaction between BRO7 and ESB phase was observed for in-situ composites. In addition, Figure 4-5 is a SEM image of final ESB-BRO7 composites calcined at 900°C for 2hrs. It clearly shows that BRO7 nanoparticles are formed on surface of ESB particles and each phase is well connected, which is beneficial for transporting of conductive species such as electrons and oxygen ions in composite cathodes.

#### **4.3.3. Electrochemical Performance**

Electrochemical performance of in-situ BRO7-ESB composite cathodes was expected to be superior to conventionally made composite cathodes using mechanical mixing due to better percolation and less agglomeration of each phase. It should be emphasized that even though there could exist many of TPB reaction sites in the

cathode, only conducting species which transport to the interface between the electrolyte and cathode can contribute to the overall performance.<sup>75, 79</sup> Figure 4-6 shows Nyquist and Bode plots of an in-situ BRO7-ESB composite cathode. ASR increases as temperature goes down since the oxygen reduction reaction is thermally activated process.<sup>74</sup> The Nyquist plot (Figure 4-6 a) was  $R_{el}$ -corrected for easy comparison. That is, the high-frequency real-axis intercept,  $R_{el}$ , was subtracted from the real component of each data point in spectra. In this way, the point of low-frequency intersecting real-axis directly corresponds to the cathode polarization,  $R_c$ . From the Bode plot (Figure 4-6 b), the dominant electrochemical process seemed to be changed from 10~1kHz at >650°C to <10Hz at <650°C. Frequency range of 1~10Hz is typically assumed to be related to oxygen adsorption (1~10Hz).<sup>55</sup>

Area specific resistance (ASR) of the cathodes can easily be calculated as follows:

$$ASR = \frac{\text{cathode area}}{2} \times R_c \quad (4-2)$$

where the cathode area is divided by 2 to account for the symmetrical cell. In Table 4-1, calculated ASR values of in-situ BRO-ESB composite cathodes and four other BRO7-ESB composite cathodes reported from our group, which were made by conventional mixing,<sup>10</sup> are shown to compare the performance of those measured at temperatures of 500~700°C. For detailed explanation about preparation methods of compared BRO7-ESB composite cathodes, refer to chapter 3.

Even though it was not substantial as expected, performance improvement was observed for in-situ composite cathode compared to all other BRO7-ESB composite cathodes except Sup BRO7-SS ESB. In particular, since the particle size combination is very similar for GNC BRO7-SS ESB and in-situ BRO7-ESB, performance improvement

was believed to be caused by better percolation and less agglomeration of in-situ composite cathodes. However, ASR of in-situ BRO7-ESB cathodes was still higher than that of Sup BRO7-SS ESB.

To further examine whether the dominating process of in-situ composite cathodes is different from those of conventionally made composite cathodes, the Bode plots of all the cathodes compared at 600°C were overlapped as shown in Figure 4-7. The characteristic frequencies of VM BRO7-SS ESB, GNC BRO7-SS ESB, In-situ BRO7-ESB, and Sup BRO7-SS ESB were almost the same, indicating that the dominant electrochemical process was not that changed. Even though better percolation and less agglomeration were expected to expedite the transport of oxygen ions through the cathode, degree of improvement seemed not sufficient enough to affect the dominant process at practical level.

On the other hand, Figure 4-8 is the Arrhenius plot of ASR for direct comparison among all the BRO7-ESB composite cathodes prepared in this study and reported in the literature.<sup>10</sup> The activation energy from this plot was calculated using the equation as below:

$$\frac{T}{ASR} = A \exp\left(\frac{-E_a}{RT}\right) \quad (4-3)$$

The activation energy of the in-situ composite cathode was determined to be ~1.24eV, which is comparable to the previously reported values, 1.2~1.34eV.<sup>9</sup>

#### 4.4. Conclusion

In-situ BRO7-ESB composite cathode was successfully developed by wet chemical based in-situ synthesis of BRO7 nanoparticles inside the stabilized ESB suspension. Pure BRO7-ESB composites were obtained after calcination of 900°C for

2hrs. Since ESB particles were dispersed and stabilized through electrostatic repulsion between functional anions adsorbed on ESB particles generated by adding a dispersant and controlling pH of the solution, BRO7 nanoparticles were formed on surface of ESB particles. As a result, less agglomeration and better percolation of each BRO7 and ESB phase were achieved for the final product. The processing cost was also reduced since separate processes for each phase were not required, which normally happens for conventional composite synthesis route. Electrochemical performance was improved for in-situ BRO7-ESB composite cathodes compared to conventionally mixed BRO7-ESB composite cathodes except Sup BRO7-SS ESB (refer to chapter 3). ASR values of  $0.097\Omega\text{cm}^{-1}$  and  $3.58\Omega\text{cm}^{-1}$  were obtained at  $700^\circ\text{C}$  and  $500^\circ\text{C}$ , respectively.

Consequently, the feasibility of in-situ composite synthesis route was successfully demonstrated. Further optimization of dispersing and stabilizing strength of dispersants will make this synthesis route more attractive to the fabrication of LT-SOFC cathodes.

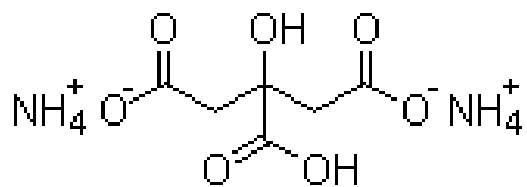


Figure 4-1. Molecular structure of ammonium citrate dibasic

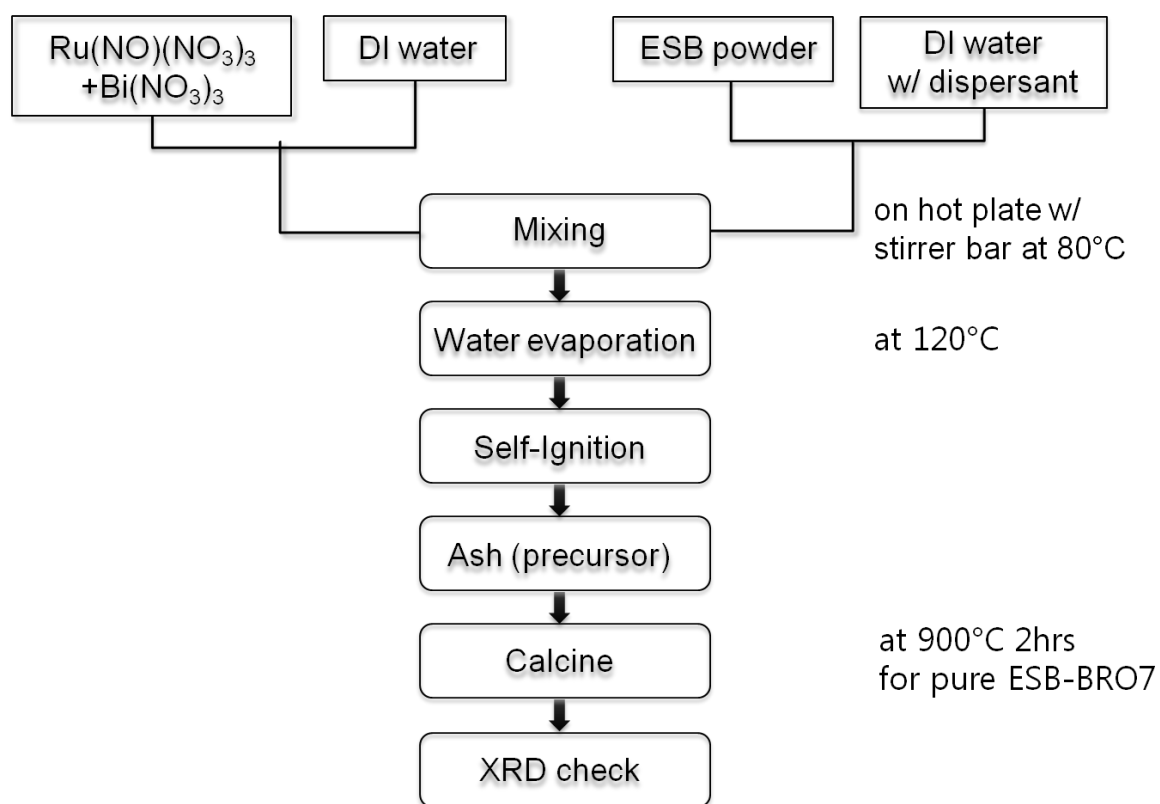


Figure 4-2. Flow chart of synthesis process for in-situ ESB-BRO7 composite cathodes

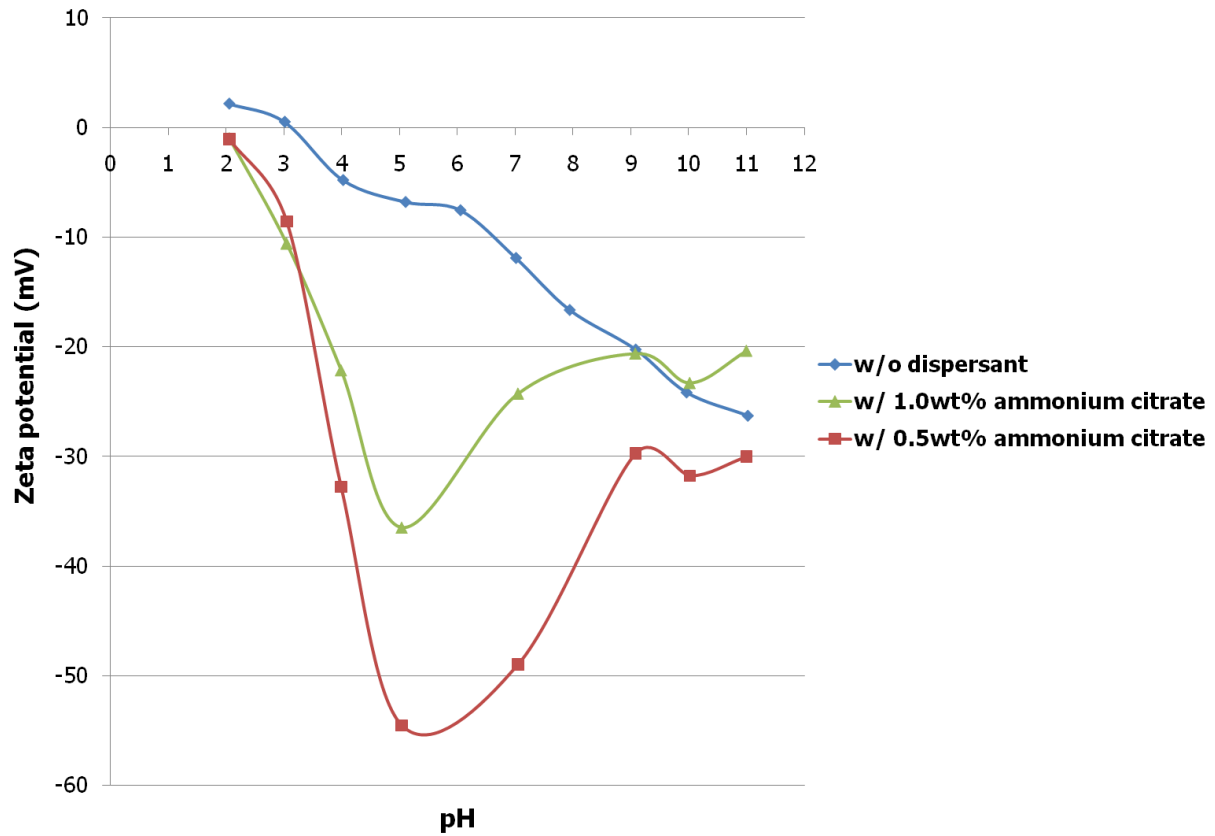


Figure 4-3. Zeta potential of ESB powder suspension with or without a dispersant (ammonium citrate) as a function of pH

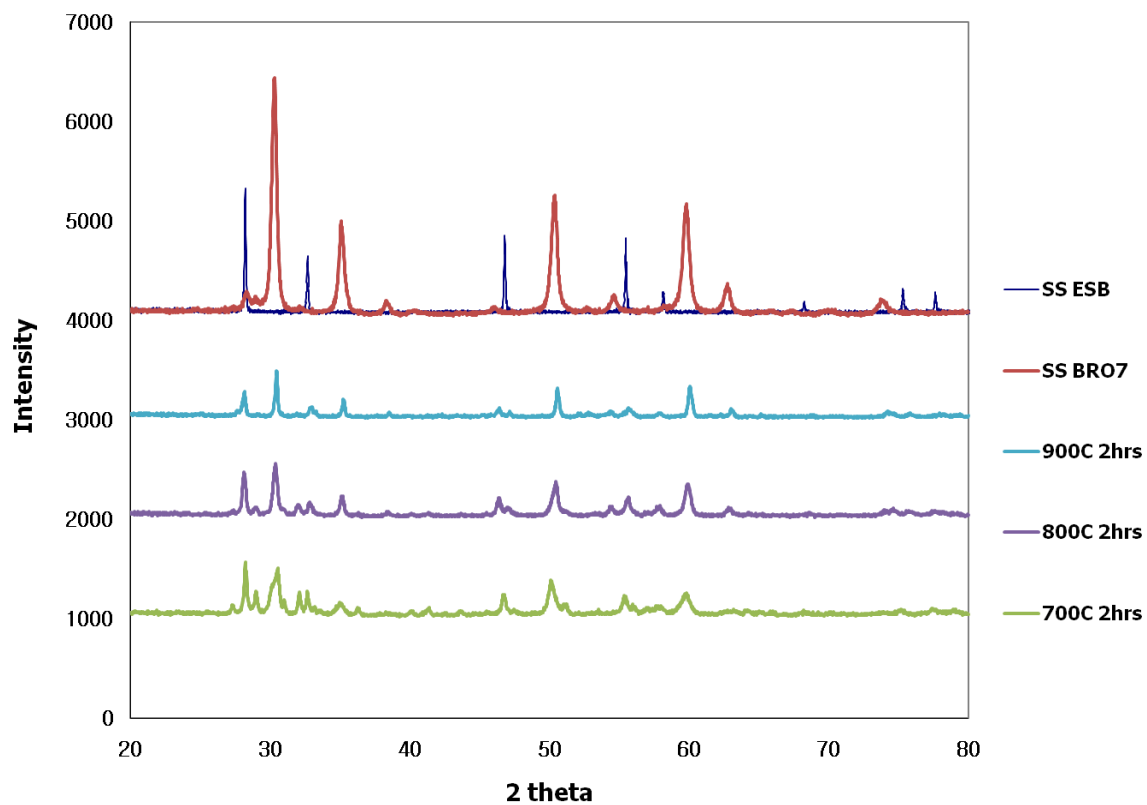


Figure 4-4. XRD patterns of in-situ ESB-BRO7 composite cathodes depending on calcining temperatures and overlapped XRD patterns of each ESB and BRO7 phase synthesized by solid state (SS) reaction for comparison

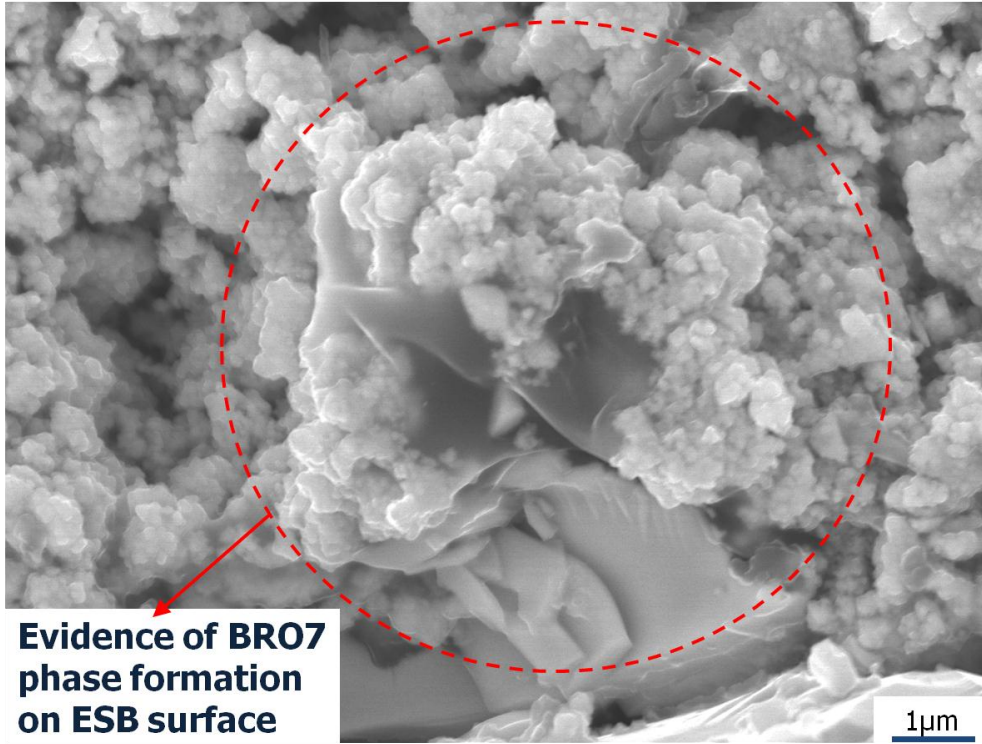


Figure 4-5. SEM image of in-situ BRO7-ESB composites showing adsorbed BRO7 nanoparticles on ESB phase

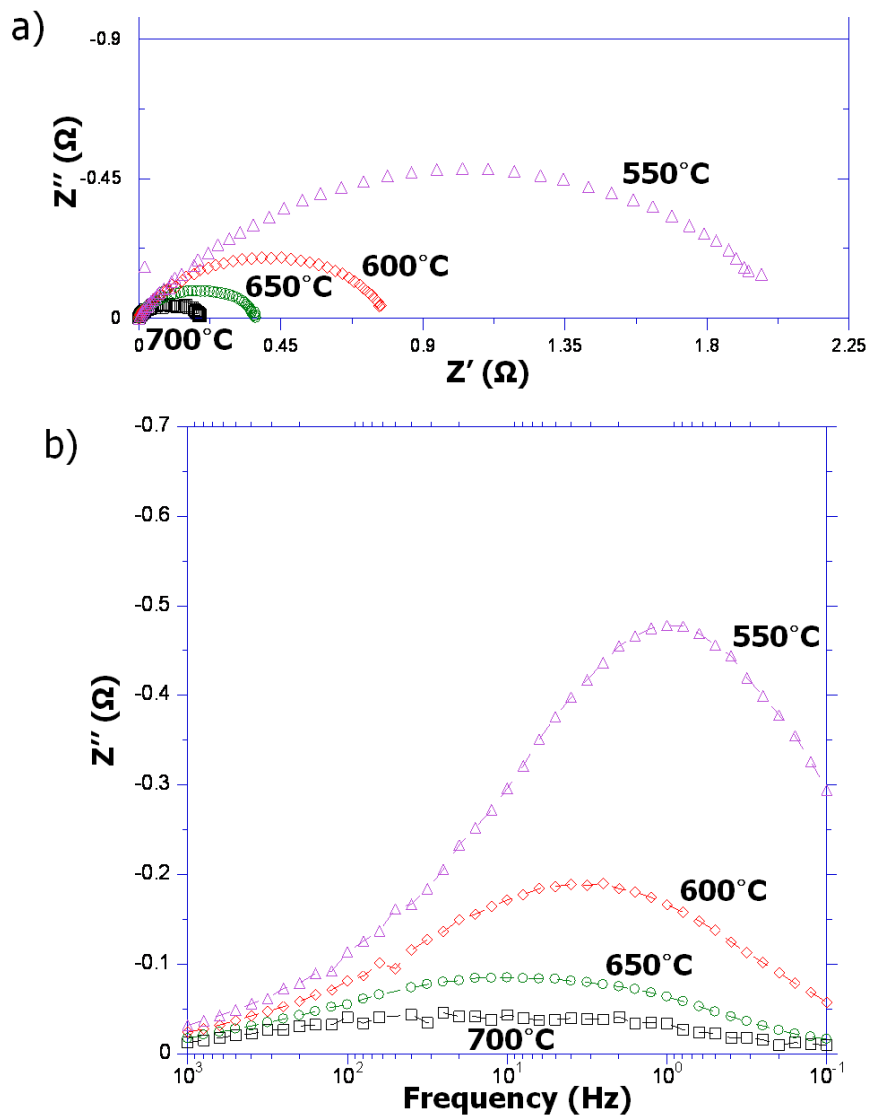


Figure 4-6. a) Nyquist and b) Bode plots of in-situ BRO7-ESB composite cathode tested at each temperature in air under open circuit potential

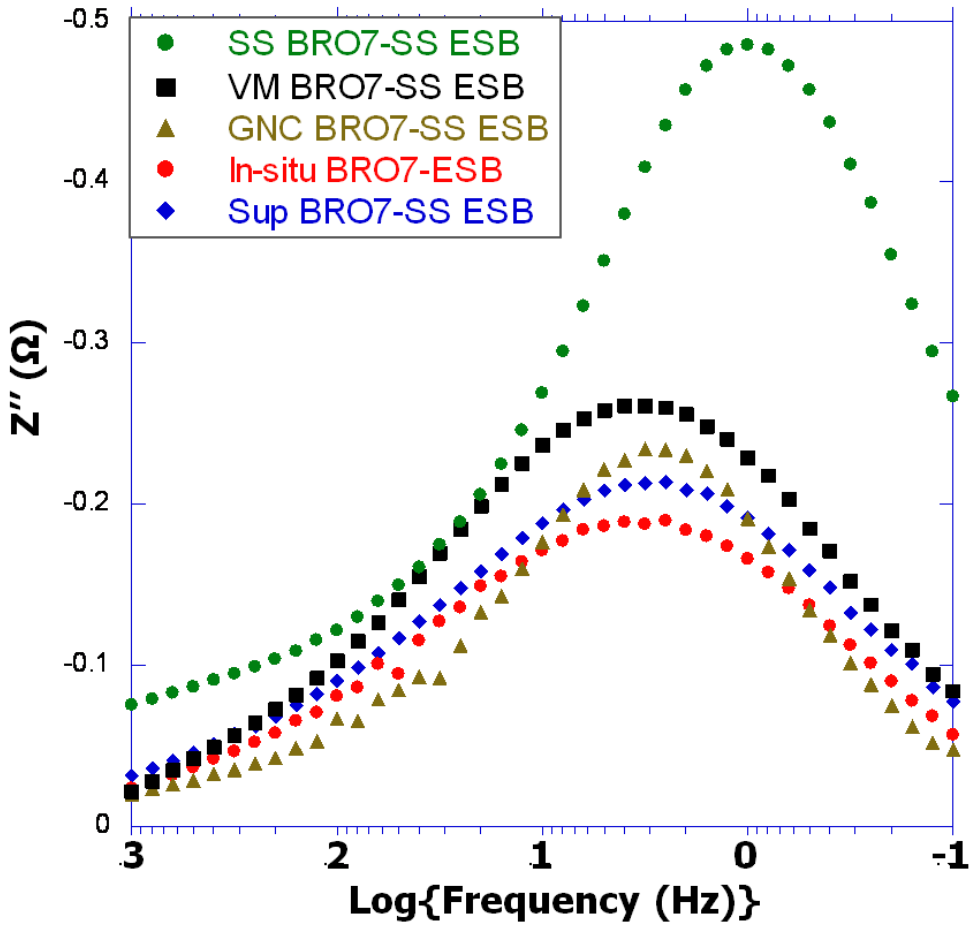


Figure 4-7. Overlapped Bode plots measured at 600°C of BRO7-ESB composite cathodes where the particle size of SS ESB is fixed whereas different processing routes were used for BRO7, resulting in different particle sizes. (VM: vibro-milled, Sup: sonicated and sedimented as described in ref.10.) The data for SS BRO7-SS ESB, VM BRO7-SS ESB, and Sup BRO7-SS ESB was extracted from ref.10 and the one for GNC BRO7-SS ESB from chapter 3

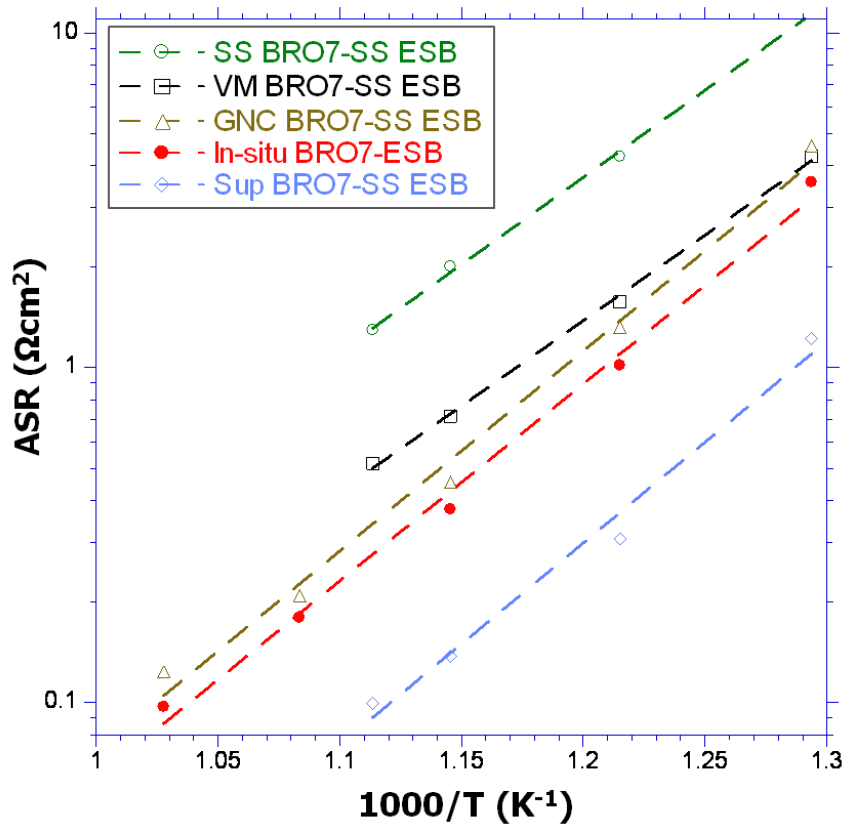


Figure 4-8. Arrhenius plot of ASR for comparison among five different cathode systems<sup>10</sup>

Table 4-1. ASR values of all BRO7-ESB composite cathodes compared at each temperature measured

Cathodes	ASR( $\Omega\text{cm}^2$ ) at each temperature					
	700°C	650°C	625°C	600°C	550°C	500°C
SS BRO7-SS ESB <sup>10</sup>			1.29	2.00	4.27	11.55
VM BRO7-SS ESB <sup>10</sup>			0.52	0.72	1.57	4.28
GNC BRO7-SS ESB (Chapter 3)	0.123	0.21		0.46	1.32	4.59
In-situ BRO7-ESB (in this study)	0.097	0.18		0.38	1.02	3.58
Sup BRO7-SS ESB <sup>10</sup>			0.23	0.35	0.92	2.80

CHAPTER 5  
PYROCHLORE BISMUTH RUTHENATE,  $\text{Bi}_2\text{Ru}_2\text{O}_7$ , INFILTRATED CATHODES FOR  
HIGH-PERFORMANCE LT-SOFCs

**5.1. Introduction**

Low temperature (LT)-solid oxide fuel cell (SOFC) operating at 650°C and below can reduce the cost of production by allowing cheaper and wider selection of materials such as stainless steel for interconnects and other structural components.<sup>76</sup> Also, improved system stability and durability are additional benefits. However, since decreasing the operating temperatures usually leads to an overall degradation of cell performance, development of cell components with higher performance is needed.<sup>77</sup> Thanks to the substantial reduction in the electrolyte ohmic resistance by employing either thin-film technology or electrolyte materials with higher ionic conductivity such as gadolinia-doped ceria (GDC), the focus of improving overall performance is now mainly on finding means to reduce the electrode polarization, in particular, the oxygen reduction reaction in the cathode.<sup>3, 78-79</sup>

The concept of a composite cathode consisting of an ionic conducting phase and an electronic conducting phase is theoretically proposed to be a highly effective way of improving cathode performance by extending the active triple-phase-boundary (TPB) region from the electrolyte/electrode interface into the electrode bulk and has been experimentally demonstrated by many researchers.<sup>6, 33, 40, 95</sup> For cathodes, for example, a composite cathode consisting of strontium-doped  $\text{LaMnO}_3$  (LSM) and yttrium-stabilized zirconia (YSZ) showed improved area specific resistance (ASR), reducing the original ASR of  $7.82\ \Omega\text{cm}^2$  obtained with a pure LSM cathode on a YSZ electrolyte to  $2.49\ \Omega\text{cm}^2$  at 700°C. ASR was further reduced to  $1.06\ \Omega\text{cm}^2$  with GDC substituted for YSZ at the same temperature. It was concluded by authors that the higher ionic

conductivity as well as the higher oxygen surface exchange rate of GDC over YSZ are the main reason for the improved performance.<sup>6</sup>

In addition, there have been many studies on optimizing the microstructure of cathodes since electrochemical performance strongly depends on the microstructural parameters such as the number of TPB reaction sites, percolation of each phase constituting the cathode, porosity for gas diffusion.<sup>32, 34-36, 96</sup> Relatively recently, a more powerful processing approach to develop the novel cathode structure was established, called 'infiltration' or 'impregnation.'<sup>41-42, 45-46, 48-49, 97-98</sup> The infiltration technique involves depositing nanoparticles of electronic, ionic conducting phase, or sometimes metal electrocatalyst into a preformed scaffold. Since the sintering of scaffold is separately carried out at high temperature for ensuring good adhesion between scaffold and electrolyte, good connection between particles to achieve the effective electronic and/or ionic conduction, and structural stability of the cathode, the infiltration of nanoparticles and the formation of desired phase can be performed at relatively low temperature.<sup>56</sup> Such prepared nanostructure allows for high catalytic activity and enlarged TPB length so that overall performance enhancement is expected. For example, Jiang et al. showed that GDC infiltrated LSM cathode could reduce its ASR down to  $0.21\Omega\text{cm}^2$  at  $700^\circ\text{C}$  when  $5.8\text{mgcm}^{-2}$  GDC was loaded, about five times lower than that ( $1.06\Omega\text{cm}^2$ ) of the conventionally made GDC-LSM composite cathode mentioned above.<sup>47</sup>

On the other hand, a composite cathode consisting of erbia-stabilized bismuth oxide (ESB) as an ionic conducting phase and pyrochlore bismuth ruthenate ( $\text{Bi}_2\text{Ru}_2\text{O}_7$  or BRO7 shortly) as an electronic conducting phase was demonstrated from our group to be one of the most promising cathode materials due to the high ionic conductivity

( $0.023\text{Scm}^{-1}$  at 773K and  $0.37\text{Scm}^{-1}$  at 973K)<sup>99</sup> of ESB and high electronic conductivity ( $\sim 300\text{Scm}^{-1}$  at room temperature up to 1173K)<sup>25</sup> of BRO7 phase.<sup>9-10, 23</sup> Moreover, the oxygen surface exchange rate of stabilized bismuth oxide is the factor of  $10^3$  larger than that of YSZ.<sup>100-101</sup> An ASR as low as  $0.03\text{Scm}^{-1}$  at 700°C was achieved for conventionally made BRO7-ESB composite cathode with the optimized microstructure and particle size combination, though the yield ratio to get those fine particles (<100nm) of BRO7 was prohibitively low, thus not suitable for mass production.<sup>10</sup> Thus, infiltrating BRO7 nanoparticles on ESB scaffolds can be an alternative effective way of fabricating BRO7-ESB composite cathodes. The improved electrochemical performance is expected as long as the infiltrated BRO7 phase forms sufficient nano-networks on the surface of ESB to provide enough electron conducting paths through the cathode layer. Furthermore, less agglomeration of each phase<sup>9</sup>, often observed with the conventionally made composite cathode, and better adhesion between the electrolyte and cathode layers will be additional advantage for these infiltrated cathodes.

Based on knowledge of infiltration and wet chemical synthesis route, BRO7 infiltrated ESB composite cathodes were developed in this study.

## **5.2. Experimental**

### **5.2.1. Infiltration Process**

Schematic of infiltration process is shown in Figure 5-1 for better understanding. ESB powder was obtained by a conventional solid state (SS) reaction route and then crushed by mortar and pestle and sieved (325 Mesh). ESB pellets were fabricated from these powders by uniaxial pressing (approximately 12 Kpsi) in a half-inch cylindrical die. Next, these green bodies were first weakly fired at 700 °C for 4 hrs before depositing ESB scaffolds on top of those. Then, ESB scaffolds were constructed by screen-printing

ESB slurry mixed with 30vol% graphite (Catalog number G67-500, Fisher Scientific) as a pore former on both sides of the weakly-fired ESB pellets to give an appropriate porosity. The pellets were then fired at 890°C for 14 hrs.

Glycine-added nitrate solutions for infiltration were prepared by the same method described in chapter 3 for GNC BRO7. Such prepared GNC BRO7 solution was stirred for 1 hr on a hot plate at 80°C for better mixing and heated up to 120°C for water evaporation until a concentrated solution (about 0.4M) was obtained. The solution was then infiltrated onto both sides of ESB scaffolds using a vacuum apparatus for better infiltration by capillary force. The cells with the precursors were oven-dried for 20 min at 70°C before further heat treatment. The symmetrical cells were then heat treated with different temperature profiles (sample #1 and #2) as shown in Figure 5-2 to form BRO7 nanoparticles and also to remove any residual carbonates and unreacted phases. The mass difference of symmetric cells before and after infiltration was measured to estimate the infiltrated BRO7 phase loading. Lastly, these cells were dried at 120°C for 1 hr, and sintered at 800°C for 2 hrs. Pure BRO7 powder was separately mixed with organic vehicles and applied on top of the cathodes as a current collector. The active cathode area, where the cathode ink was applied (the top or bottom surface area of the electrolyte), was 0.97cm<sup>2</sup>.

### **5.2.2. Characterization**

Evaluation of particle size and microstructure of the cathode systems was carried out with the aid of a JEOL JSM 6400 scanning electron microscope (SEM). Further compositional analysis of infiltrated BRO7 particles was performed by a JEOL TEM 200CX transmission electron microscope (TEM) combined with energy dispersive X-ray spectrometry (EDS) on a sliced cathode sample prepared by focused ion beam (FIB). In

addition, Amira image reconstruction software was utilized to calculate the average porosity of ESB scaffolds. Finally, impedance testing of BRO7 infiltrated cathodes on ESB pellets was performed using a Solartron 1470E frequency response analyzer at open circuit potential over a frequency range of 0.01Hz to 0.1MHz with AC voltage amplitude of 50mV at temperatures of 550–700°C in air. Impedance set-up is visualized in Figure 5-3 for better understanding.

### **5.3. Results and Discussion**

#### **5.3.1. Cathode Microstructure and the Effect of Heating Condition**

Figure 5-4 shows typical cross-sectional SEM images of BRO7 infiltrated ESB cathodes. ESB scaffolds and BRO7 nanoparticles are clearly seen in the images. ESB scaffolds were well connected and good adhesion between scaffold and the electrolyte was obtained for both sample #1 and #2. However, the distribution of BRO7 particles turned out to be quite different for each sample. For sample #1, mostly the top half layer of ESB scaffolds was infiltrated and the deposited particles are scattered rather than continuous whereas more continuous and deeper infiltration through ESB scaffolds was observed for sample #2. Gradual heating from room temperature with slow heating rate (sample #1) seemed to be an ineffective way to penetrate the BRO7 nitrate solution into the scaffold because the solution returns to the external surface of the cathode where it remains after firing.<sup>102</sup> On the other hand, the auto-ignition for BRO7 phase formation takes place right away for sample #2 when the sample is inserted into the furnace already preheated to 300°C. From our previous study on BRO7 nanoparticle synthesis using GNC (chapter 3), it was found that if not enough heat (below 300°C) is provided to viscous glycine-nitrate solution, the auto-ignition reaction is sluggish when it starts self auto-ignition, thus resulting in formation of less pure and larger BRO7 particles. Also,

low temperature heating affected degree of the agglomeration of synthesized BRO7 powder because less gas byproduct was produced during the reaction for preventing the agglomeration of particles. Consequently, the heating condition was concluded to affect degree of the infiltration (penetration depth, distribution, and size of BRO7 nanoparticles etc). Magnified SEM image clearly showed BRO7 nanoparticles deposited on the surface of the ESB scaffold with size range of 100~200nm in diameter (Figure 5-5).

The way of area selection for porosity calculation and its average porosity value is shown in Figure 5-6. The average porosity was estimated to be ~23.7vol%, which is a little bit lower than expected because 30vol% of graphite was used as a pore-former to construct ESB scaffolds. Since only bright region in the middle of images was selected for porosity calculation, there could be some errors involved depending on how to select the area.

The loading of infiltrated BRO7 was determined by mass change before and after infiltration to be about 4.59wt% ( $1.0\text{mgcm}^{-2}$ ) and 5.46wt% ( $1.2\text{mgcm}^{-2}$ ) relative to ESB scaffolds for sample #1 and #2, respectively, with 2 min of vacuum-assisted nitrate solution infiltration. The infiltrated amount with vacuum assistance seemed higher than that of drop coating by hand reported in the literature. For example, it was reported that GDC loading was  $0.72\text{mgcm}^{-2}$  after one infiltration, increased to  $1.68\text{mgcm}^{-2}$  after twice, and to  $5.8\text{mgcm}^{-2}$  after six times of repeated infiltration.<sup>47</sup> Thus, it is believed that vacuum-assisted infiltration is a more powerful method to deposit materials than drop coating by hand. However, it should be pointed out that the BRO7 loading can be further optimized with repeated infiltration as long as the appropriate porosity for gas

transport is maintained. There should be the optimized loading at which the deposited nanoparticles provide both ionic and electronic conducting pathways effectively throughout the cathode.

### 5.3.2. Compositional Analysis

Compositional analysis was performed by TEM with EDS on both ESB scaffolds and BRO7 nanoparticles to confirm the formation of BRO7 phase (Figure 5-7). While no Ru element was detected on ESB scaffolds, it was detected on BRO7 nanoparticles as shown in the bottom of the image (Figure 5-7 b), clearly indicating that BRO7 formed on the surface of ESB scaffold.

### 5.3.3. The Effect of Infiltration on Cathode Polarization

Figure 5-8 shows the Nyquist plot of BRO7 infiltrated ESB cathode #1 at different temperatures (550~700°C). At 700°C, it seems that multiple arcs are involved in the resulting shape of spectrum. In other words, the electrochemical processes are uniformly distributed over a wide range of frequencies (0.1Hz~1kHz). That is, all the sub-reaction steps such as oxygen adsorption and dissociation, diffusion of oxygen ion, and ion incorporation are playing roles to certain degree in the overall oxygen reduction reaction. However, as temperature decreases, processes more related to low frequency range (0.1~10Hz) start to dominate the overall process as shown at 550°C, which is typically assumed to be related to oxygen adsorption (1~10Hz) and gas diffusion through the pores (<1Hz).<sup>55</sup>

ASR was calculated from impedance spectra at each temperature as follows:

$$ASR = \frac{\text{cathode area}}{2} \times [Z'(\text{low freq intercept}) - Z'(\text{high freq intercept})] \quad (5-1)$$

For sample #1, an ASR value of  $0.096\Omega\text{cm}^2$  was obtained at  $700^\circ\text{C}$  and  $3.55\Omega\text{cm}^2$  at  $500^\circ\text{C}$ . This is about 22% lower compared to that of conventionally mixed GNC BRO7-SS ESB composite cathode (chapter 3).

On the other hand, Figure 5-9 shows the Nyquist plot of BRO7 infiltrated ESB cathode #2 at different temperatures ( $550\sim 700^\circ\text{C}$ ). Even though the frequency distribution seemed to be similar to that of sample #1, the shape of spectrum looked different. The calculated ASR values were  $0.073\Omega\text{cm}^2$  and  $1.82\Omega\text{cm}^2$  at  $700^\circ\text{C}$  and  $500^\circ\text{C}$ , respectively. This is the marked improvement compared to GNC BRO7-SS ESB. The overall performance improvement is better visualized in Figure 5-10 through overlapped Nyquist plots of all three composite cathodes compared. About 41~68% of performance improvement was achieved depending on the temperatures. However, since different degree of improvement was obtained at each temperature, it was inferred that different dominating process could be involved for each sample at each temperature.

To further clarify this observation, three Bode plots of GNC BRO7-SS ESB, sample #1, and sample#2 were overlapped to elucidate the dominating process for each cathode at each temperature as shown in Figure 5-11. The most significant point from the figure is that the electrochemical process related to 10Hz~1kHz frequency range was dramatically reduced for sample #2 regardless of temperatures so that the dominating process is now changed to 1~10Hz frequency range for sample #2. Since the main difference between sample #1 and #2 is the degree of penetration and continuity of BRO7 nanoparticles through the cathode layer, more TPB reaction sites

are assumed to be formed and a more continuous electronic pathway is expected to be established deep down to the scaffolds/electrolyte interface for sample #2.

Typically, the electrochemical process in the 10Hz~1kHz frequency range is attributed to diffusion of oxygen ion ( $O_{ad}^-$ ,  $O_{ad}^{2-}$ ,  $O_{TPB}^-$ , or  $O_{TPB}^{2-}$ ) towards TPB reaction sites.<sup>55, 79</sup> Since mainly the surface layer of ESB scaffold was infiltrated for sample #1, diffusion of available adsorbed oxygen and oxygen ion are limited, thus oxygen incorporation takes place primarily at the surface of the ESB scaffold. On the other hand, there exist more BRO7 nanoparticles distributed continuously throughout the scaffolds for sample #2. Therefore, the number of TPB sites is likely to dramatically increase throughout the cathode layer, resulting in much easier diffusion of adsorbed oxygen and oxygen ion towards TPB sites, which is observed as the dramatic reduction of cathode polarization in 10Hz~1kHz frequency range. In other words, the effective TPB length is extended.

The effect of infiltration on the overall performance becomes more substantial as temperature goes down, suggesting that different activation energies are involved. The activation energy for each sample was calculated using the equation as below:

$$\frac{T}{ASR} = A \exp\left(\frac{-E_a}{RT}\right) \quad (5-2)$$

The resulting values are shown in Table 5-1. It is clearly seen that the activation energy was indeed reduced for the infiltrated cathode with the optimized heating condition (sample #2). The more reduced cathode polarization at lower temperatures demonstrates significance of both the effective TPB reaction sites and high ionic conductivity/oxygen surface exchange rate of the ionic conductive phase in the composite cathodes.

### 5.3.4. Performance Comparison

To compare the performance of these cathodes with the others from literatures, an Arrhenius plot of ASR for cathodes used in this study along with several other infiltrated cathodes in addition to conventionally mixed LSM-YSZ and LSM-GDC was drawn in Figure 5-12. As can be seen, the optimized BRO7 infiltrated ESB cathode (sample #2) shows the best performance among all the cathodes compared.<sup>103</sup> Considering that YSB infiltrated LSM cathode also employs a stabilized bismuth oxide (YSB) as an ionic conducting phase which has similar ionic conductivity and oxygen surface exchange rate to ESB, BRO7 phase is also assumed to play an important role in the substantial reduction of cathode polarization. However, it should be noticed that the LSM phase rather than YSB was employed as the scaffolds for their system. Thus, there is the possibility for further performance enhancement with infiltrated LSM-YSB cathode if YSB is used as the scaffolds and LSM is infiltrated. This strategy is expected to work well since the electrochemical process in 10Hz~1kHz frequency range seems to be dominant for infiltrated LSM-YSB as shown in Figure 5-13, indicating that diffusion of oxygen ion ( $O_{ad}^-$ ,  $O_{ad}^{2-}$ ,  $O_{TPB}^-$ , or  $O_{TPB}^{2-}$ ) towards TPB reaction sites is limited, which was considerably improved in our BRO7 infiltrated ESB cathodes (sample #1 and #2).

In Figure 5-14, the performance of BRO7 infiltrated ESB cathodes is further compared to the other conventionally made BRO7-ESB composite cathodes reported previously from our group.<sup>10</sup> For detailed explanation about the preparation method of each composite cathode, refer to chapter 3.

The optimized BRO7 infiltrated ESB cathode (sample #2) exhibits the second best performance among all the BRO7-ESB composite cathodes shown. However, since

Sup BRO7-Sup ESB composite cathode showing the lowest ASR was prepared by conventional solid state reaction followed by multiple extra processing steps such as vibro-milling, sonication, and sedimentation, the yield ratio to get the final product is prohibitively low yield, thus not suitable for mass production. Consequently, from the realistic point of view, the processing route used to synthesize Sup BRO7-Sup ESB is not appropriate for fabrication of high performance cathodes. As a summary, ASR values of all BRO7-ESB composite cathodes are listed in Table 5-2 to show the exact values obtained.

#### **5.4. Conclusion**

A high-performance composite cathode was developed by infiltrating a (Bi,Ru) nitrate solution with glycine onto preformed ESB scaffolds. It was found that care must be taken for infiltration process since different heating conditions can lead to different degrees of infiltration (penetration depth, distribution, and size of BRO7 nanoparticles etc). The optimized heating condition enabled the formation of continuous BRO7 nanoparticles through the scaffolds, resulting in substantial extension of the effective TPB reaction sites. Infiltrated BRO7 nanoparticles substantially accelerated the cathode reaction, especially diffusion of adsorbed oxygen and oxygen ions towards TPB reaction sites. ASR values as low as  $0.073\Omega\text{cm}^2$  and  $1.82\Omega\text{cm}^2$  were achieved with the optimized cathode at  $700^\circ\text{C}$  and  $500^\circ\text{C}$ , respectively, which was the best performance among all the infiltrated cathodes compared and the second best among all BRO7-ESB composite cathodes compared. Furthermore, the activation energy was also reduced for the infiltrated cathode. In conclusion, it was demonstrated that the BRO7 infiltrated ESB cathode can be an excellent candidate as a cathode for LT-SOFC.

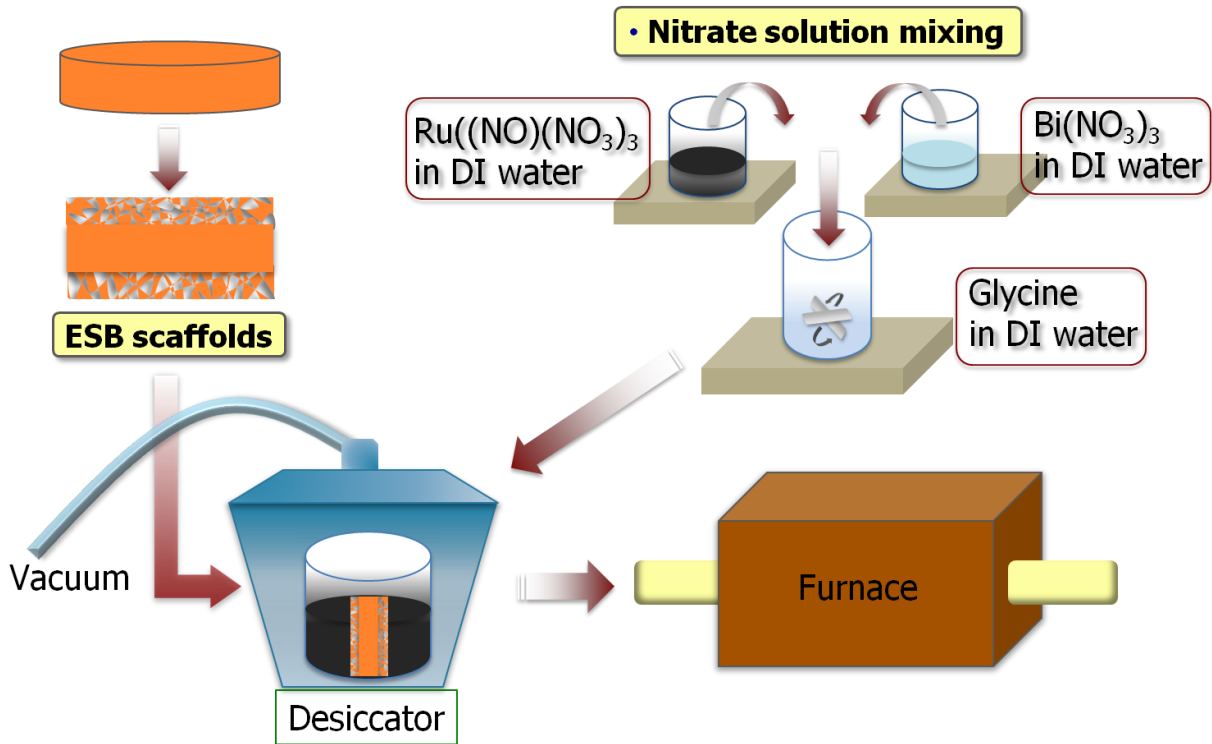


Figure 5-1. Schematic of infiltration process

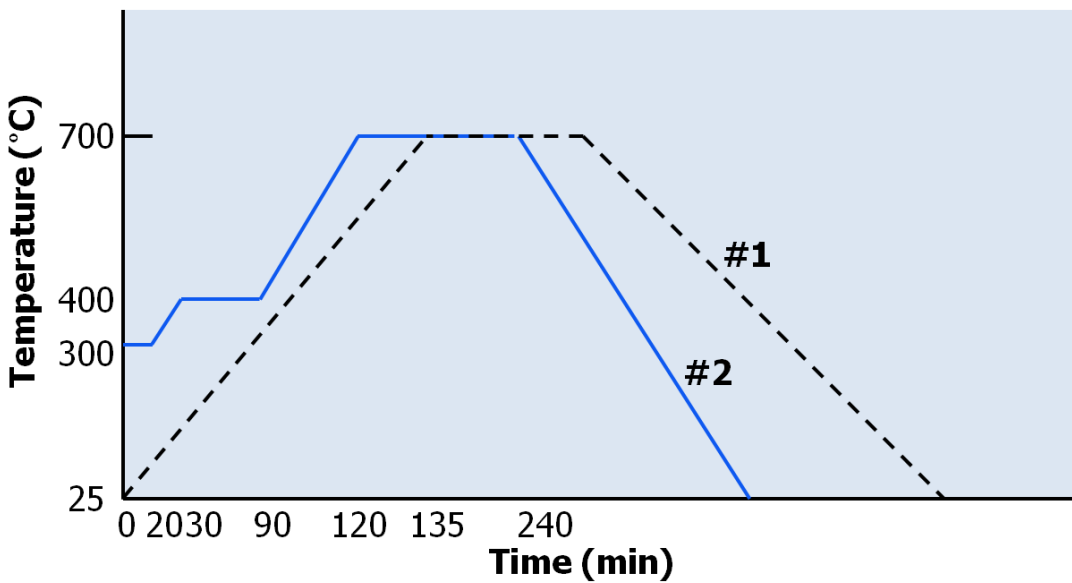


Figure 5-2. Temperature profiles of two different heat treatment conditions for sample #1 and sample #2

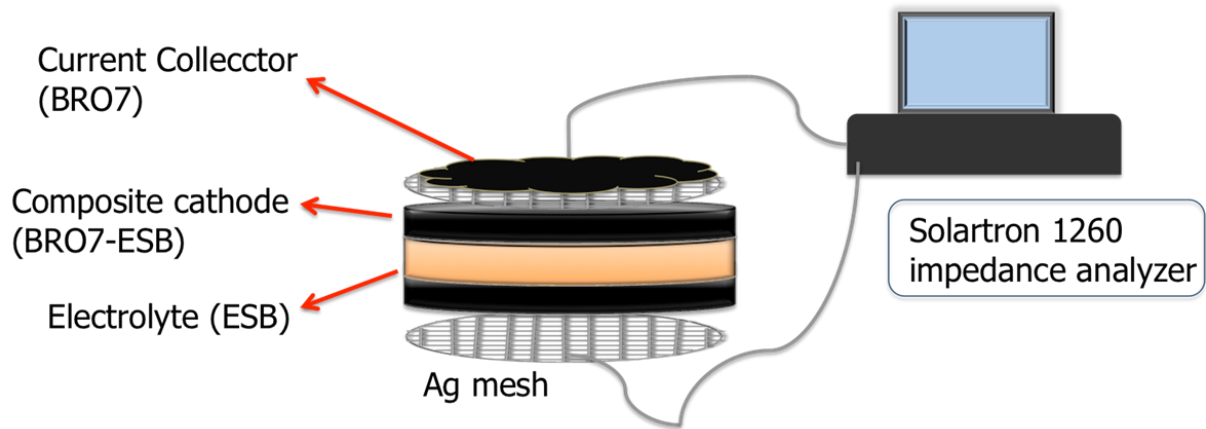


Figure 5-3. Schematic of impedance testing set-up

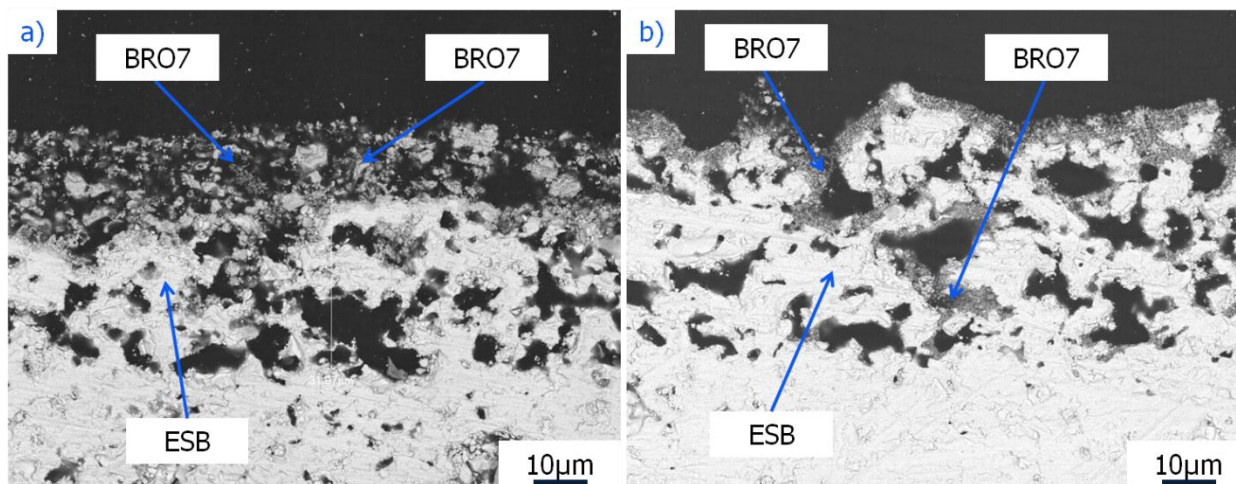


Figure 5-4. Cross-sectional SEM images of a) sample #1 and b) sample #2

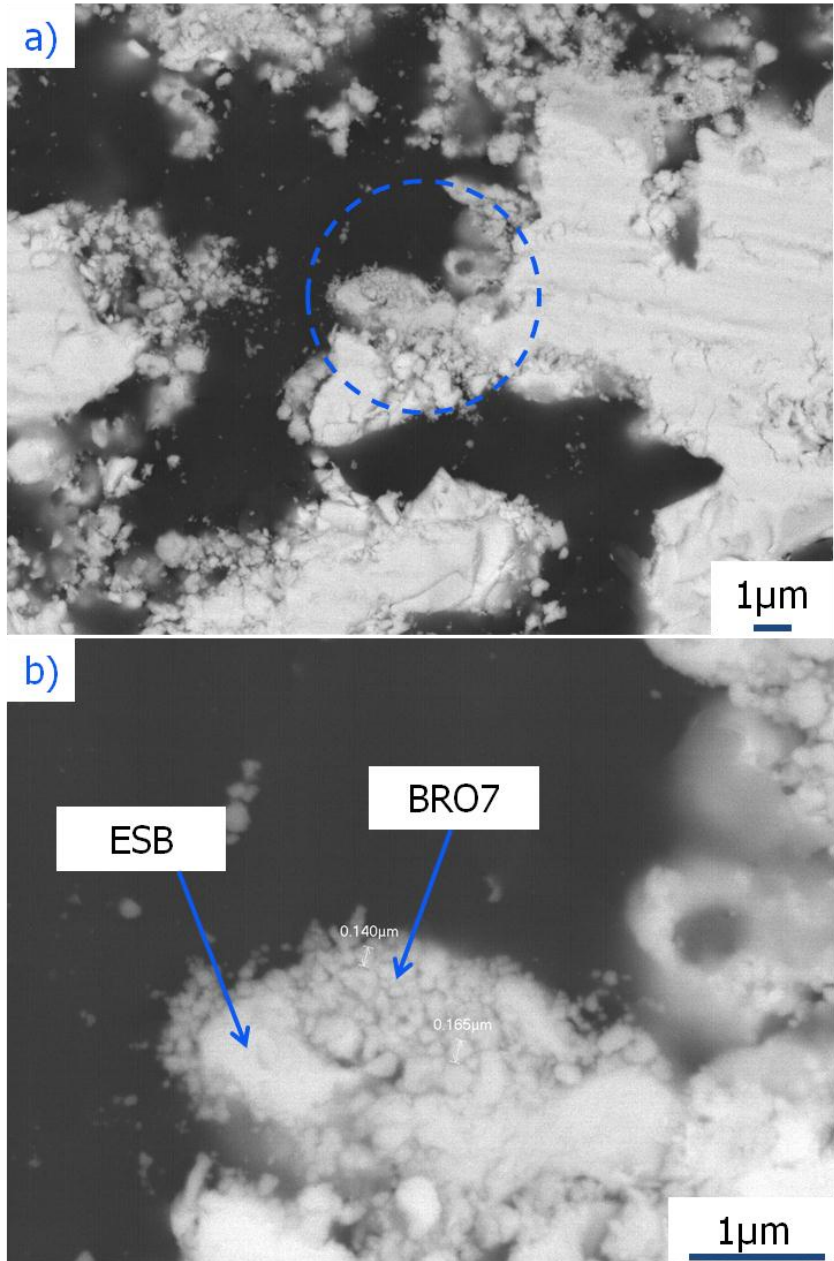
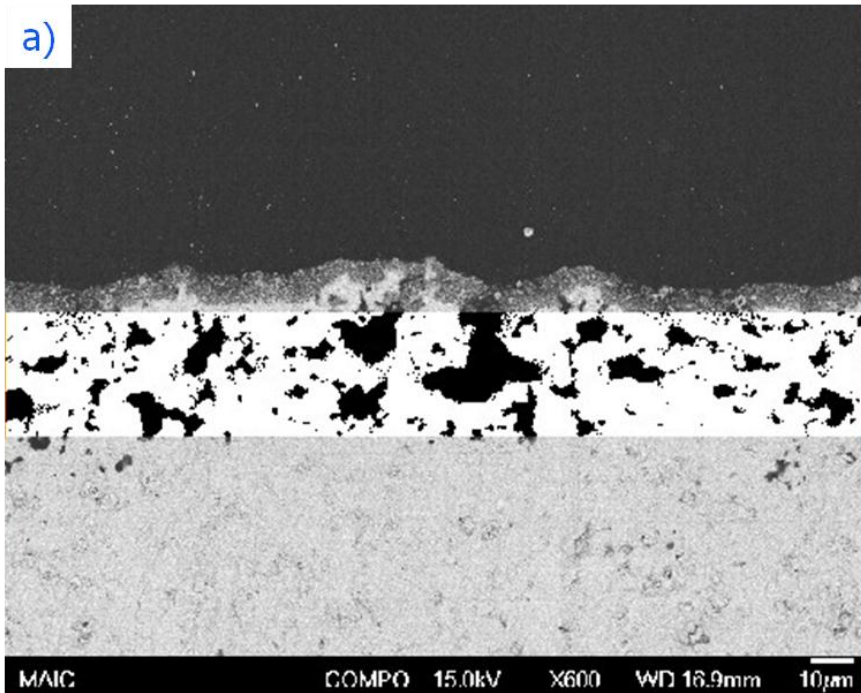


Figure 5-5. SEM images of BRO7 nanoparticles taken from sample #1: the same spot with (a) low (b) high (zoomed-in) magnifications



b) Avg Porosity	<b>23.7 %</b>
Standard deviation	2.04
95% confidence interval	22.4% < Avg. < 25%

Figure 5-6. a) A SEM image of infiltrated BRO7-ESB composite cathodes taken from sample #1, showing the region (bright region in the middle of image) used for porosity calculation where 30vol% of graphite was used as a pore-former to construct ESB scaffolds and b) calculated average porosity and its standard deviation

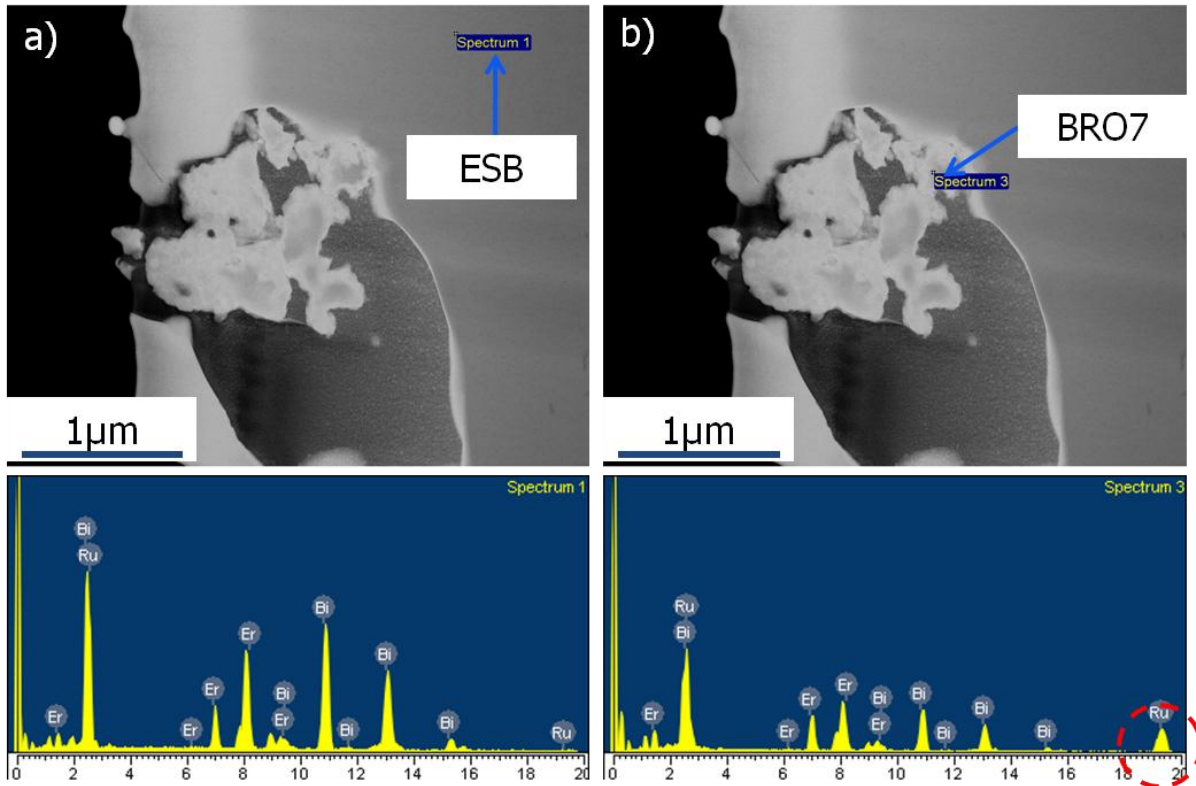


Figure 5-7. TEM images and EDS spectra of a) ESB scaffold and b) BRO7 nanoparticles with red circle on Ru element energy spectrum indicating the presence of Ru element in BRO7 nanoparticles (taken from sample #1)

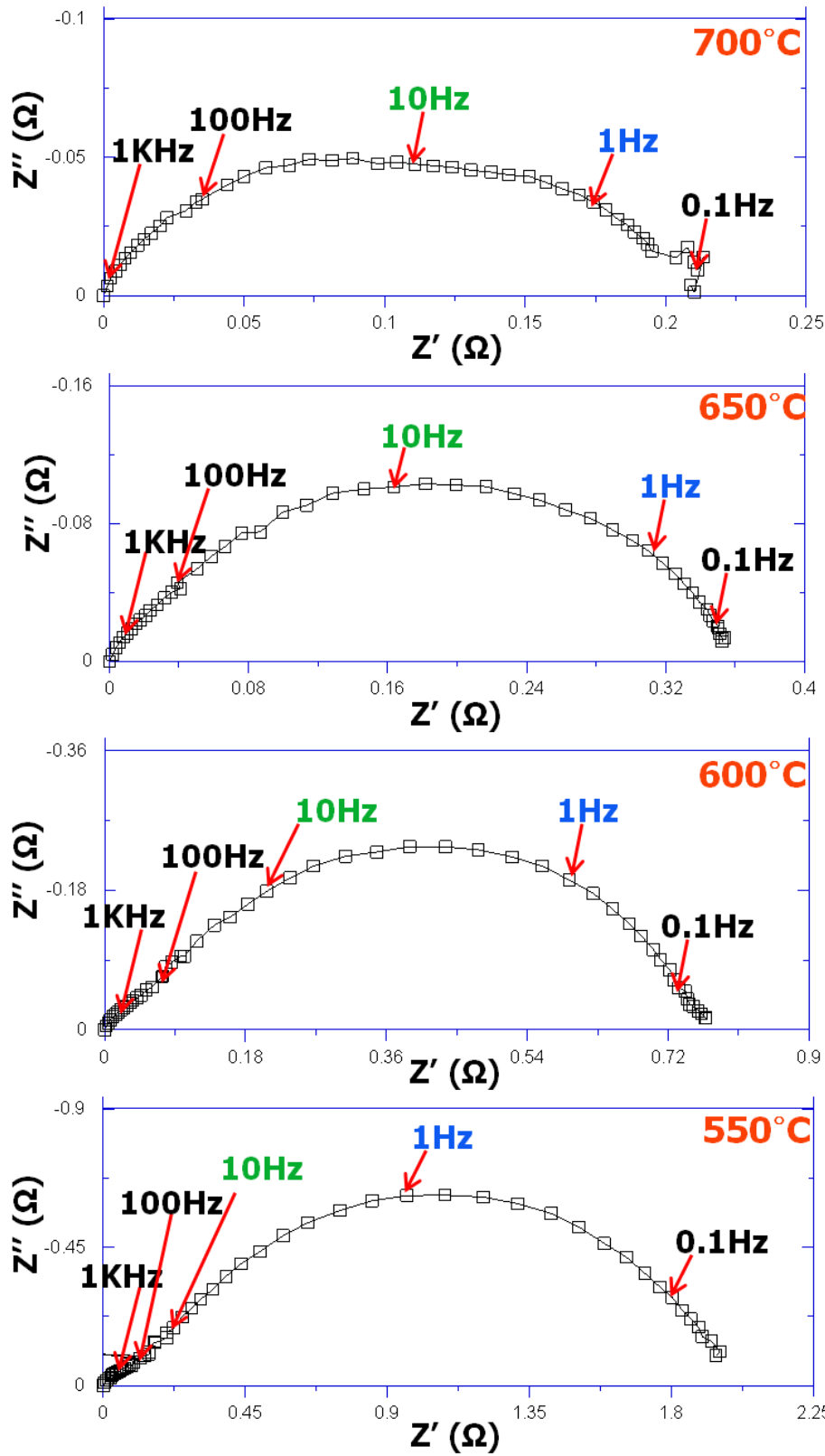


Figure 5-8. Nyquist plots of BRO7 infiltrated ESB composite cathode (sample #1) at different temperatures (550~700°C)

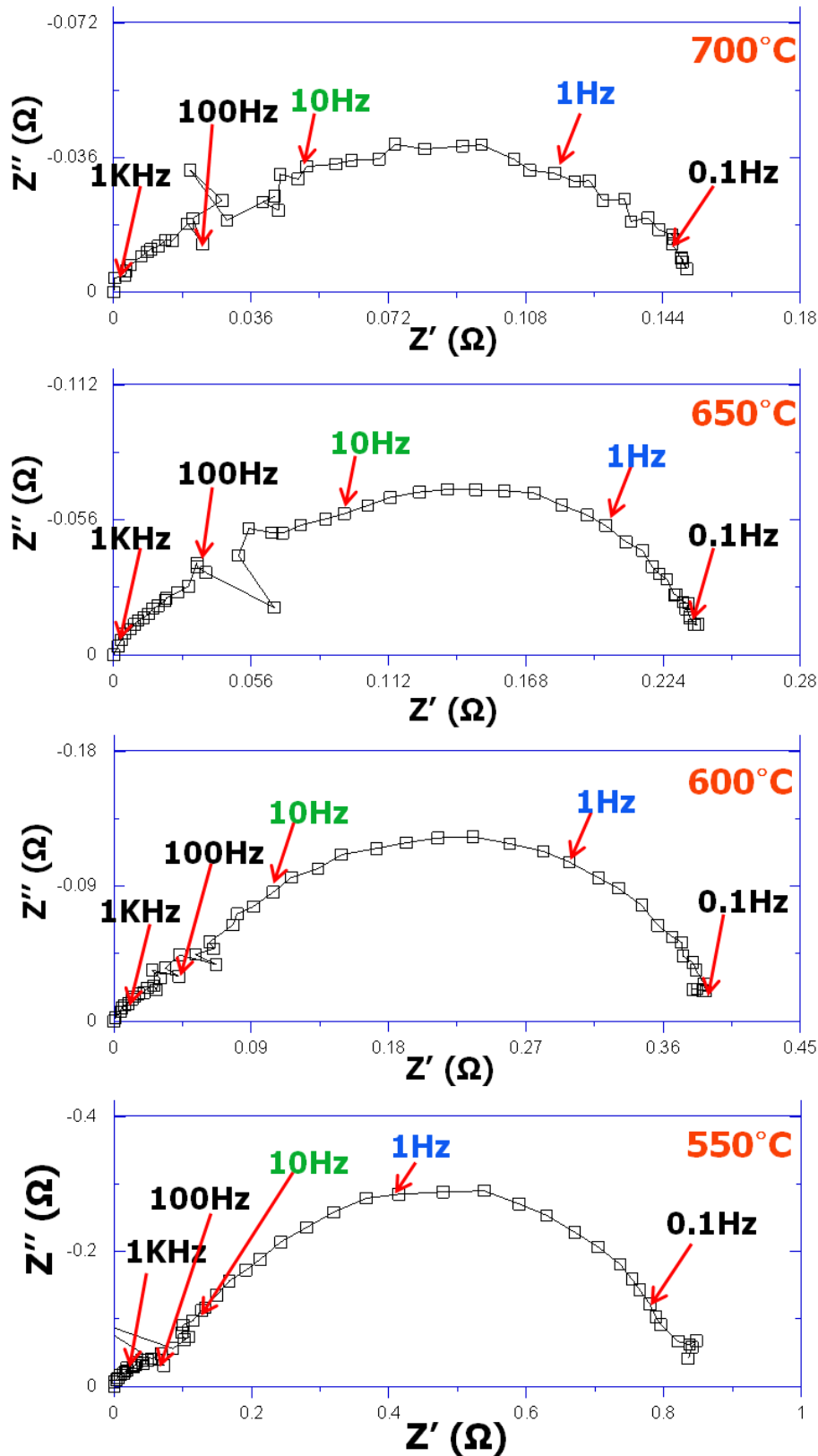


Figure 5-9. Nyquist plots of BRO7 infiltrated ESB composite cathode (sample #2) at different temperatures (550~700°C)

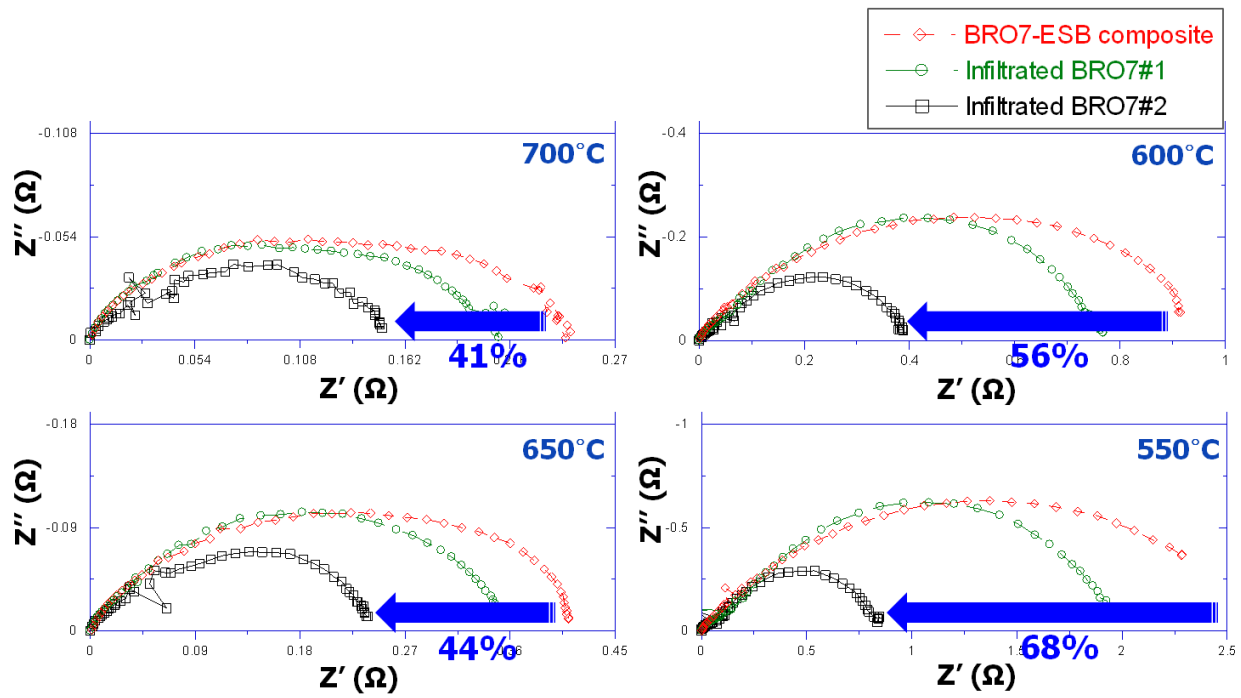


Figure 5-10. Overlapped Nyquist plots of GNC BRO7-SS ESB, infiltrated BRO7-ESB sample #1, and sample #2 at different temperatures (550~700°C) to better show the improvement of performance

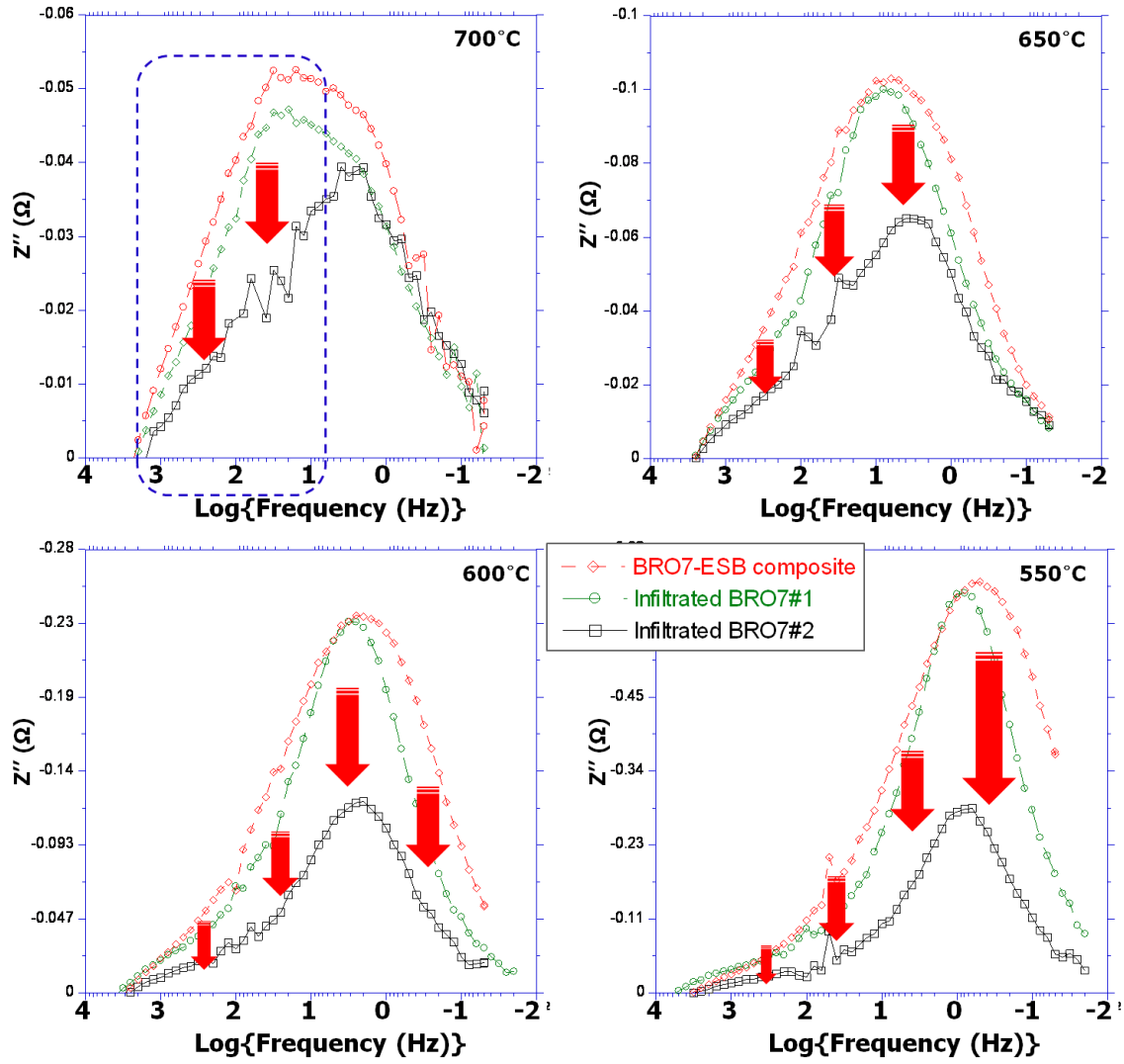


Figure 5-11. Overlapped Bode plots of BRO7 infiltrated ESB composite cathodes (sample #1 and #2) and GNC BRO7-SS ESB composite cathode at different temperatures (550–700°C) for comparison on dominating processes

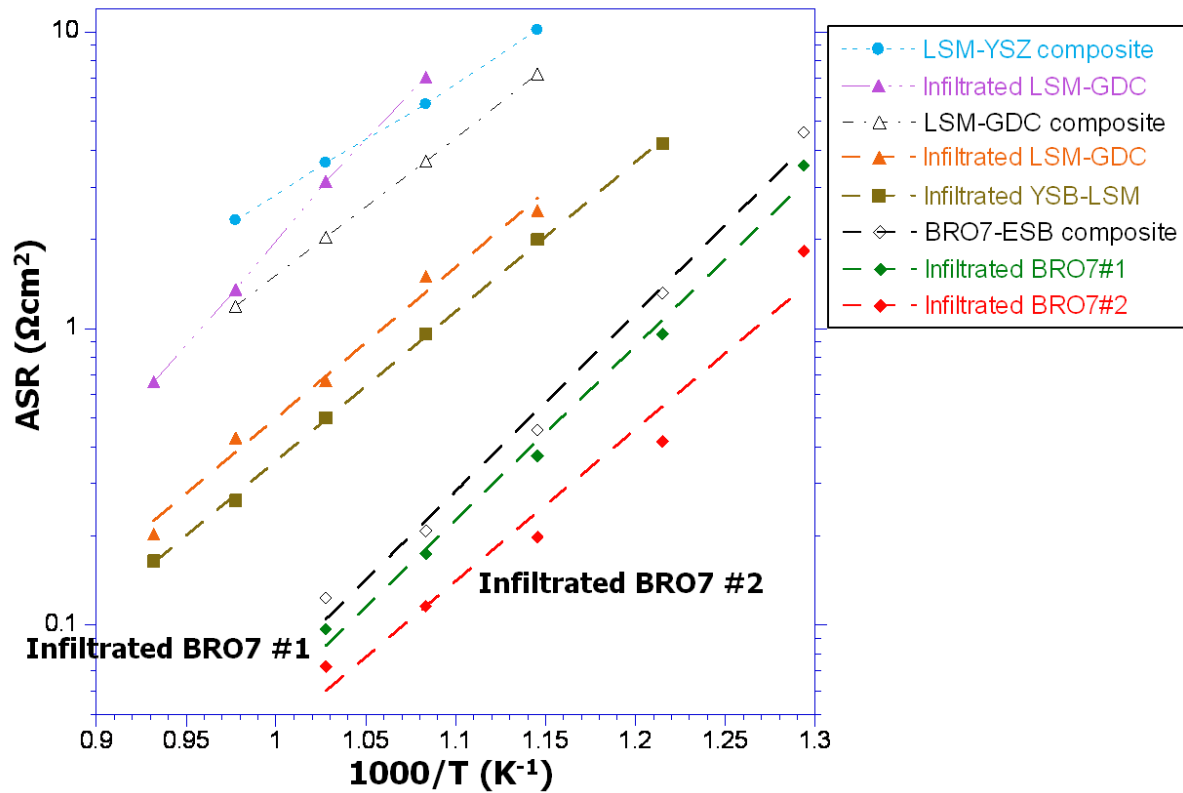


Figure 5-12. Arrhenius plot of ASR for performance comparison with several conventionally mixed composite cathodes and the other infiltrated cathodes reported. All the data other than BRO7-ESB composite cathode and infiltrated BRO7 cathodes (#1 and #2) in this study was extracted from the references cited in ref.103

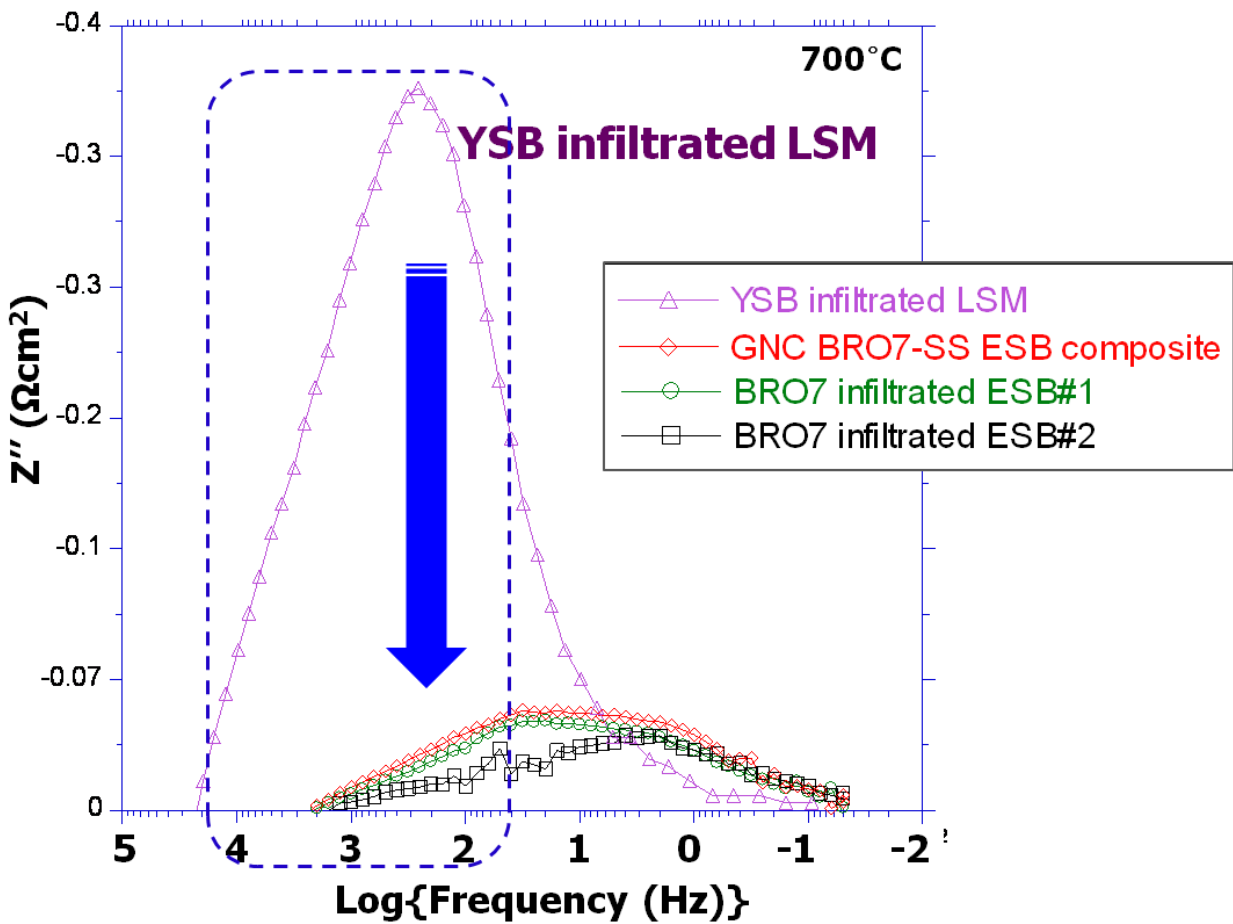


Figure 5-13. Overlapped Bode plots of BRO7 infiltrated ESB cathodes (sample #1 and #2), conventionally mixed BRO7-ESB composite cathode, and YSB infiltrated LSM cathodes at 700°C. Notice that imaginary impedance ( $Z''$ ) is area normalized for direct comparison. Data for YSB infiltrated LSM was extracted from ref.103

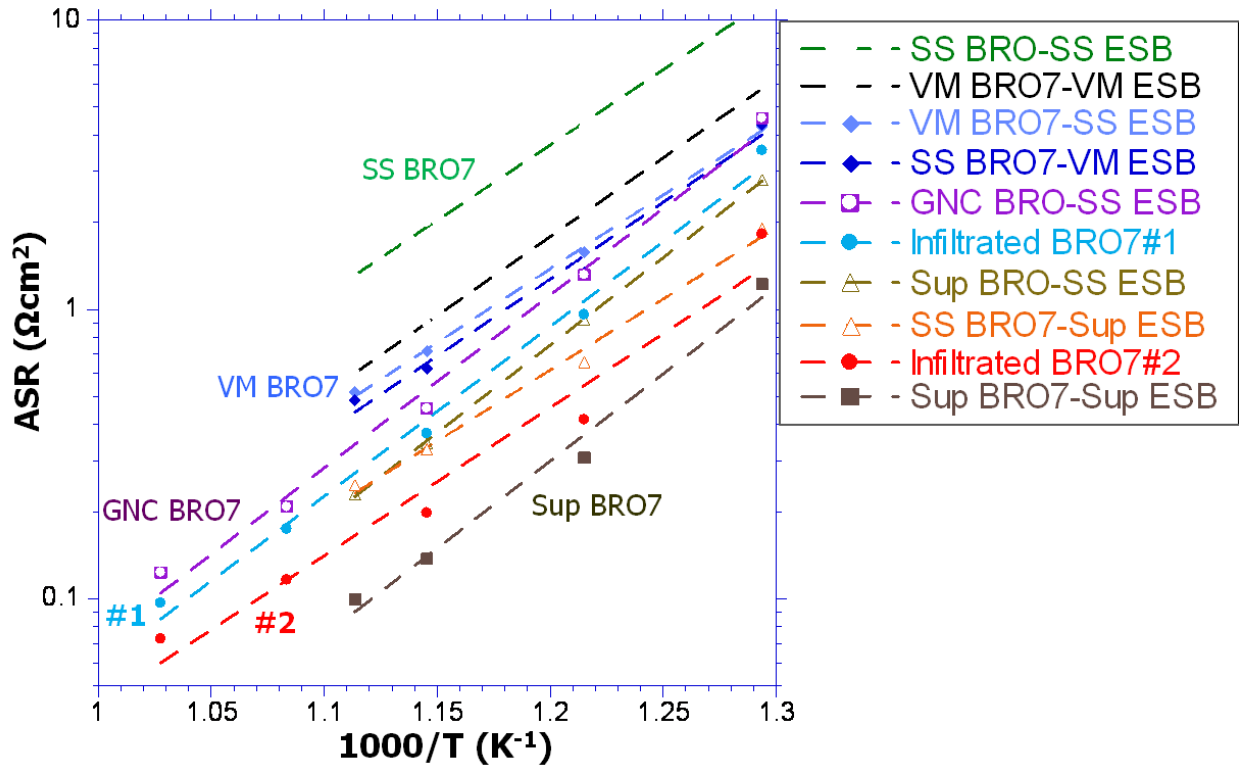


Figure 5-14. Arrhenius plot of ASR for performance comparison among all conventionally mixed BRO7-ESB composite cathodes. All the data other than GNC BRO7-ESB composite cathode and infiltrated BRO7 cathodes (#1 and #2) in this study was extracted from ref.10

Table 5-1. Activation energies of GNC BRO7-SS ESB (chapter 3) and infiltrated BRO7 cathodes (sample #1 and #2) calculated from Figure 5-12 using equation (5-2)

Activation Energy (Ea)	GNC BRO7-SS ESB (chapter 3)	Infiltrated BRO7 #1 (in this study)	Infiltrated BRO7 #2 (in this study)
eV	1.26	1.24	1.09
$\text{kJmol}^{-1}$	122	120	105

Table 5-2. ASR values of all BRO7-ESB composite cathodes compared at each temperature measured

Cathodes	ASR( $\Omega\text{cm}^2$ ) at each temperature					
	700°C	650°C	625°C	600°C	550°C	500°C
SS BRO7-SS ESB <sup>10</sup>			1.29	2.00	4.27	11.55
VM BRO7-VM ESB <sup>10</sup>			0.61	0.90	2.09	5.89
VM BRO7-SS ESB <sup>10</sup>			0.52	0.72	1.57	4.28
SS BRO7-VM ESB <sup>10</sup>			0.49	0.63	1.34	4.35
GNC BRO7-SS ESB (chapter 3)	0.123	0.21		0.46	1.32	4.59
SS BRO7-Sup ESB <sup>10</sup>			0.25	0.33	0.66	1.90
Sup BRO7-SS ESB <sup>10</sup>			0.23	0.35	0.92	2.80
Sup BRO7-Sup ESB <sup>10</sup>			0.10	0.14	0.31	1.22
Infiltrated BRO7-ESB #1 (in this study)	0.096	0.17		0.37	0.96	3.55
Infiltrated BRO7-ESB #2 (in this study)	0.073	0.12		0.20	0.42	1.82

## CHAPTER 6 SUMMARY

Solid oxide fuel cell (SOFC) is a one of the most promising candidates for future power generation due to its high efficiency and low pollution emission. However, for its successful commercialization, the production cost should be reduced dramatically to compete with the other power generating systems. Reducing the operating temperatures down to 500~650°C could be an option so that the wider selection of cheaper materials such as stainless steel for interconnects and the other structural components will be realized. However, since reduction of operating temperatures generally causes performance degradation of the system due to its inherent characteristic of thermally activated process, development of high-performance constituting components at low temperatures is necessary. With the inception of thin-film electrolytes and electrolytes with ionic conductivities higher than conventional YSZ materials, much of research focus is now geared towards the electrode (anode and cathode) development. Since the oxygen reduction reaction becomes more of an issue than fuel oxidation reaction at low temperatures, hence it is essential to develop a cathode with high catalytic activity towards oxygen reduction as well as a microstructure that maximizes the number of reaction sites (TPBs) and facilitates oxygen transport towards the electrolyte. It is also important that the cathode be chemically compatible with the electrolyte and mechanically stable with time so that performance does not degrade to a significant extent over the lifetime of the cell.

In this dissertation, three different physicochemical approaches were attempted to develop a high-performance composite cathode for LT-SOFC applications. First, glycine-nitrate-combustion (GNC) synthesis route was thoroughly investigated to obtain

pure high-temperature pyrochlore  $\text{Bi}_2\text{Ru}_2\text{O}_7$  (BRO7). Especially glycine-to-nitrate ratio (G/N) was carefully examined to find the optimum ratio for better crystallinity and phase purity of BRO7. The optimum G/N ratio, which can generate the maximum reaction heat, was found to be about 0.6 based on the calculation above. Five different G/N ratios, 0.4, 0.6, 0.8, 1.0, and 1.2, were chosen in this study for BRO7 synthesis to evaluate the effect of G/N ratio on the crystallinity and particle size of BRO7 precursor. BRO7 precursors become more crystalline from amorphous as G/N ratio is varied from 0.4 to 1.2 even though the best crystallinity was expected to appear at G/N=0.6 resulting from the maximum reaction heat provided. This could be attributed to the presence of abundant oxygen gas from the environment so that more reducing agent, i.e. glycine, is required to generate the maximum heat, which is in turn evidenced as better crystallinity for G/N ratios above 0.6. However, the best peak pattern similar to pure BRO7 was achieved at G/N=1.0 with less impurity phases such as unreacted  $\text{Bi}_2\text{O}_3$ , Ru and/or  $\text{RuO}_2$ .

G/N ratio of 1.0 was selected for further study of phase evolution at different calcining conditions and microstructural analysis on the final powder. The duration was fixed at 2hrs for this study while the calcining temperatures were varied at 600-900°C with 100°C interval. As calcining temperature arose, the crystallinity increased accordingly. Pure BRO7 phase was achieved even at 700°C 2hrs, which is noticeable compared to 900°C-tens of hours heat treatment necessary for the formation of pure BRO7 with conventional SS route. Impurity phases such as unreacted  $\text{Bi}_2\text{O}_3$  was totally removed beyond 700°C.

For BRO7 powders calcined at 700°C 2hrs, the average crystallite size of ~24nm in diameter was achieved. However, it should be pointed out that the resulting particles tend to aggregate during calcining. For better understanding on behavior of these aggregates, analysis on particle size distribution was performed. Most of aggregated particles exist in size range of 200~400nm in diameter. However, this size range was still much smaller than the conventionally made one. For example, the particle size of vibro-milled (VM) SS BRO7 after 7 days of vibro-milling was reduced from ~1.31 $\mu\text{m}$  of as-prepared SS BRO7 to ~0.73 $\mu\text{m}$ , which is still about two times bigger than nanoparticles of GNC BRO7 and contains a small number fraction but significant volume fraction of large, unbroken particles. On the other hand, energy dispersive spectroscopy (EDS) analysis on nanoparticles confirmed the composition of  $\text{Bi}_2\text{Ru}_2\text{O}_7$ .

Composite cathodes of such prepared BRO7 with SS ESB showed better electrochemical performance than SS BRO7-SS ESB and VM BRO7-SS ESB as well. ASR values of 0.123 $\Omega\text{cm}^2$  at 700°C and 4.59 $\Omega\text{cm}^2$  at 500°C, respectively, were achieved, which follows well the trend of particle size effect on performance of composite cathodes. Additionally, the number of processing steps (thus time) was dramatically reduced by GNC route. In conclusion, it was demonstrated that GNC can be an effective synthesis route to produce nanoparticles of pyrochlore BRO7 and its composite cathode would be a potential candidate as a cathode material for LT-SOFC application.

Secondly, a unique in-situ composite synthesis route was developed and applied to synthesize a BRO7-ESB composite cathode with better percolation and less agglomeration of each phase through wet chemical based in-situ synthesis process.

The processing cost was also expected to be reduced since separate processes for each phase to make a final composite cathode were not required, which normally happens for conventional composite synthesis route. Since ESB particles were dispersed and stabilized through electrosteric repulsion between functional anions adsorbed on ESB particles generated by adding a dispersant and controlling pH of the solution, BRO7 nanoparticles were formed on surface of ESB particles. As a result, less agglomeration and better percolation of each BRO7 and ESB phase were achieved for the final product.

The isoelectric point (IEP) of ESB suspension turned out to be about pH 3.1. However, as ammonium citrates were added to the suspension, potential curves were shifted to the lower pH side and, more importantly, to the more negative values because the surface layer of ESB particles becomes more negative due to adsorption of functional anions of the dispersant ( $\text{COO}^-$  or  $\text{O}^-$ ). Thus, suspensions can be stabilized from electrostatic repulsion between particles developed from overlap of the electric double layer in the solution. The IEP of ESB suspensions with ammonium citrates was estimated to be  $\sim$ pH 1.9. Since the IEP of ESB suspension was changed before and after addition of ammonium citrates, there should be some interactions, called specific adsorption, between ESB particles and dispersants. 0.5wt% (relative to ESB powder) ammonium citrate gave the suspension more negative zeta potential than 1.0wt% ammonium citrate due to its lower ionic strength of the solution with 0.5wt%, thus extended double layer thickness ( $\lambda$ ). As a result, stability of the particles in suspension was enhanced with 0.5wt% ammonium citrate.

pH range of 5~7 with 0.5wt% of ammonium citrate was chosen as the optimized stabilizing condition for synthesis of in-situ composite cathodes since the zeta potential of ESB suspension at this pH showed the maximum negative value (about -50mV), which is enough for effectively stabilizing ESB suspension. Final pure BRO7-ESB composites were obtained after calcination of 900°C for 2hrs.

Electrochemical performance was improved for in-situ BRO7-ESB composite cathodes compared to that of conventionally made GNC BRO7-SS ESB composite cathodes. ASR values of  $0.097\Omega\text{cm}^2$  and  $3.58\Omega\text{cm}^2$  were obtained at 700°C and 500°C, respectively. The activation energy of the in-situ composite cathode was determined to be  $\sim 1.24\text{eV}$ , which is comparable to the previously reported values, 1.2~1.34eV. Consequently, the feasibility of in-situ composite synthesis route was successfully demonstrated. Further optimization of dispersing and stabilizing strength of dispersants will make this synthesis route more attractive to the fabrication of LT-SOFC cathodes.

Lastly, the infiltration of BRO7 on ESB scaffolds was carried out to increase the electrochemical performance. Two different heating conditions were applied to deposit BRO7 nanoparticles on the surface of the ESB scaffolds. The distribution of BRO7 nanoparticles turned out to be quite different for each sample. For sample #1, mostly the top half layer of ESB scaffolds was infiltrated and the deposited particles are scattered rather than continuous whereas more continuous and deeper infiltration through ESB scaffold was observed for sample #2. Gradual heating from room temperature with slow heating rate (sample #1) seemed to be an ineffective way to penetrate the BRO7 nitrate solution into the scaffold because the solution returned to the external surface of the cathode where it remains after firing. On the other hand, the

auto-ignition for BRO7 phase formation takes place right away for sample #2 when the sample is inserted into the furnace already preheated to 300°C. It was found that if not enough heat (below 300°C) is provided to viscous glycine-nitrate solution, the auto-ignition reaction is sluggish when it starts self auto-ignition, resulting in larger and less pure BRO7 particles. Also, low temperature heating affected degree of the agglomeration of synthesized BRO7 powder because less gas byproduct was produced during the reaction for preventing the agglomeration of particles. Consequently, the heating condition was concluded to affect degree of the infiltration (penetration depth, distribution, and size of BRO7 nanoparticles etc).

Electrochemical performance of such prepared BRO7-ESB composite cathode was compared with the other infiltrated cathodes and also other conventionally made BRO7-ESB composite cathodes reported in the literatures. The optimized BRO7 infiltrated ESB cathode (sample #2) showed the second best performance among all BRO7-ESB composite cathodes compared. It was believed that the optimized heating condition enabled the formation of continuous BRO7 nanoparticles through ESB scaffolds, resulting in substantial extension of the effective TPB reaction sites. The extended TPB substantially accelerated the cathode reaction, especially diffusion of adsorbed oxygen and oxygen ion. ASR values as low as  $0.073\Omega\text{cm}^2$  and  $1.82\Omega\text{cm}^2$  were achieved with the optimized cathode at 700°C and 500°C, respectively. Furthermore, the activation energy was also reduced for the infiltrated cathode. In conclusion, it was demonstrated that the BRO7 infiltrated ESB cathode can be an excellent candidate as a cathode for LT-SOFC.

## APPENDIX A ISSUE ON SYNTHESIS OF PURE $\text{Bi}_2\text{Ru}_2\text{O}_7$

Throughout this dissertation, pyrochlore bismuth ruthenate ( $\text{Bi}_2\text{Ru}_2\text{O}_7$ , or shortly BRO7) was used as one of the primary components in composite cathodes for LT-SOFC. Although satisfactory results were obtained in terms of electrochemical impedance test, phase purity of BRO7 was one of the main obstacles to be attacked many times because there were many impurity phases possible to be formed due to incomplete reaction among constituting elements i.e. Ru, Bi, and O. Since BRO7 possesses a high temperature pyrochlore structure, the reaction temperature is one of the critical factors influencing degree of reaction, thus purity of BRO7 phase. For example, if the reaction temperature is not sufficient enough,  $\text{Bi}_3\text{Ru}_3\text{O}_{11}$  (or  $\text{Bi}_2\text{Ru}_2\text{O}_{7.3}$ ) phase appears instead. This is why many researchers have chosen solid state reaction method for BRO7 synthesis, which is high temperature heat treatment over  $900^\circ\text{C}$  for tens of hours.

Difference between phases is normally characterized from XRD patterns. As can be seen in Figure A-1,  $\text{Bi}_3\text{Ru}_3\text{O}_{11}$  (or  $\text{Bi}_2\text{Ru}_2\text{O}_{7.3}$ ) contains more number of diffraction peaks around  $30^\circ$  in  $2\theta$  while BRO7 shows only two strong peaks around  $30^\circ$  (Figure A-2), the latter of which correspond to diffractions from (311) and (222) planes. Overall, the XRD pattern is matched well with pure BRO7 phase. This is a quite exciting result if it is considered that BRO7 was synthesized with a wet chemical synthesis i.e. glycine-nitrate combustion (GNC) rather than conventional solid state reaction, which is fast auto-ignition reaction enabling formation of pure BRO7 with fine particle size resulting from high reaction temperature in short reaction time. Glycine plays a significant role as a chelating agent for cations (Ru, Bi) and a fuel for the reaction as well. Since only mild

post-heat treatment (700°C for 2hrs) was applied to precursor to remove unreacted phase such as Ru and  $\rho$ -Bi<sub>2</sub>O<sub>3</sub>, particle size of the final product was kept small (20~40nm in diameter). This is marked reduction in particle size compared to the one synthesized with solid state reaction showing micron size.

However, more careful examination on the XRD pattern confirmed that one extra peak other than two main BRO7 peaks exists at about 28.5° in 2θ for synthesized BRO7 with GNC. It was realized that this peak comes from the different composition of bismuth ruthenate, i.e. Bi<sub>12</sub>RuO<sub>20</sub> (Figure A-2). It was assumed to form due to incomplete reaction between the constituting elements or insufficient of elements in the vicinity during reaction. However, this is not surprising because this phase was also observed sometimes even with conventional solid state reaction. Therefore, it should be emphasized that formation of small amount of Bi<sub>12</sub>RuO<sub>20</sub> phase doesn't compromise the superiority of GNC method to conventional solid state reaction for synthesis of fine particle size BRO7. Moreover, it was found that this extra phase could be removed with aid of leaching process. Figure A-3 shows XRD patterns for BRO7 before and after leaching taken from the literature.

However, leaching process was not applied to GNC BRO7 in this dissertation for reasons below;

1. It is the extra processing step increasing the processing cost and time
2. Materials loss from leaching process was concerned
3. The overall performance was not affected that much since it was small amount compared to pure BRO7 so that sufficient electronic conductivity is provided from synthesized BRO7.

Consequently, pure BRO7 with small amount of  $\text{Bi}_{12}\text{RuO}_{20}$  was successfully synthesized by GNC and GNC is the strong synthesis technique for producing fine particles of BRO7, which is preferred for SOFC cathode application since triple phase boundary (TPB) reaction sites for oxygen reduction can be dramatically increased from more contacts between constituting particles in the cathode. However, care must be taken depending on the application. If the electronic conductivity is the main concern of the application, it is desirable to use leaching process for removal of the extra phase,  $\text{Bi}_{12}\text{RuO}_{20}$ , since this extra phase doesn't contribute to the electronic conductivity.

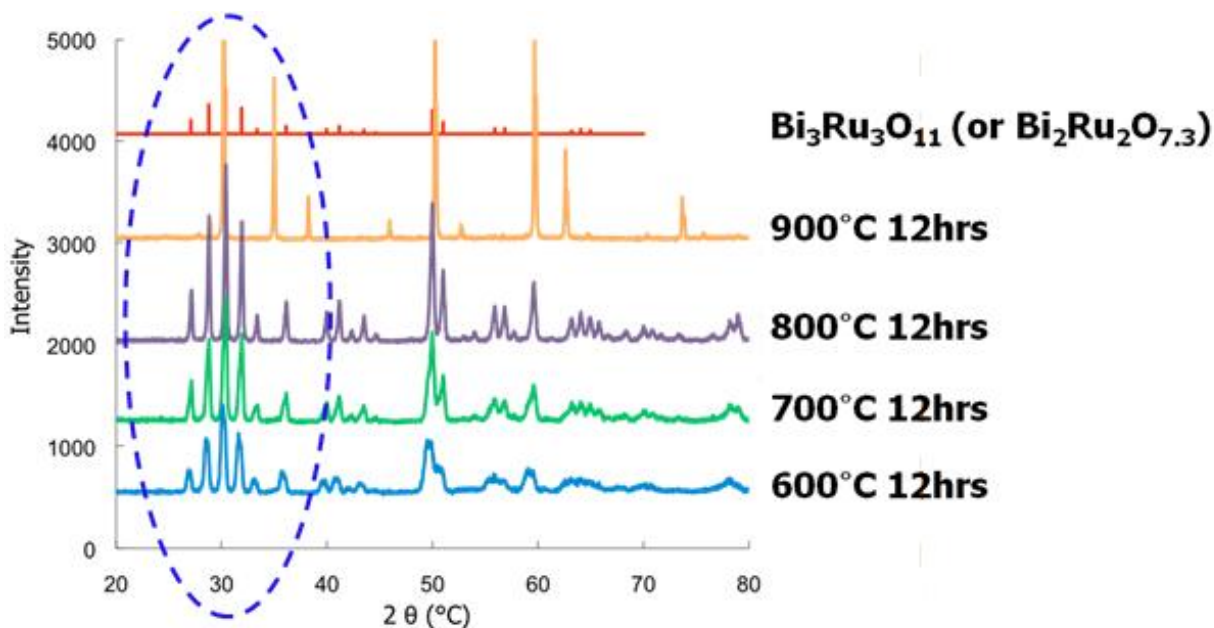


Figure A-1. Diffraction patterns of  $\text{Bi}_3\text{Ru}_3\text{O}_{11}$  (or  $\text{Bi}_2\text{Ru}_2\text{O}_{7.3}$ ) synthesized with amorphous citrate reaction method

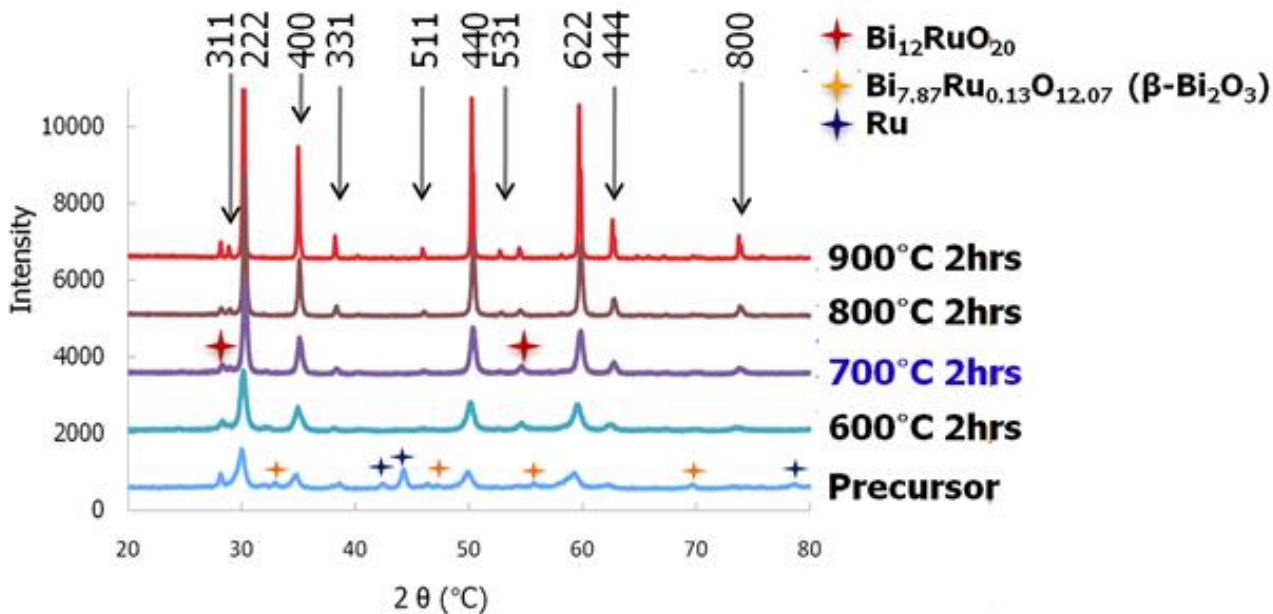


Figure A-2. Diffraction patterns of BRO7 and impurity phases such as  $\text{Bi}_3\text{Ru}_3\text{O}_{11}$  (or  $\text{Bi}_2\text{Ru}_2\text{O}_{7.3}$ ) synthesized with GNC method

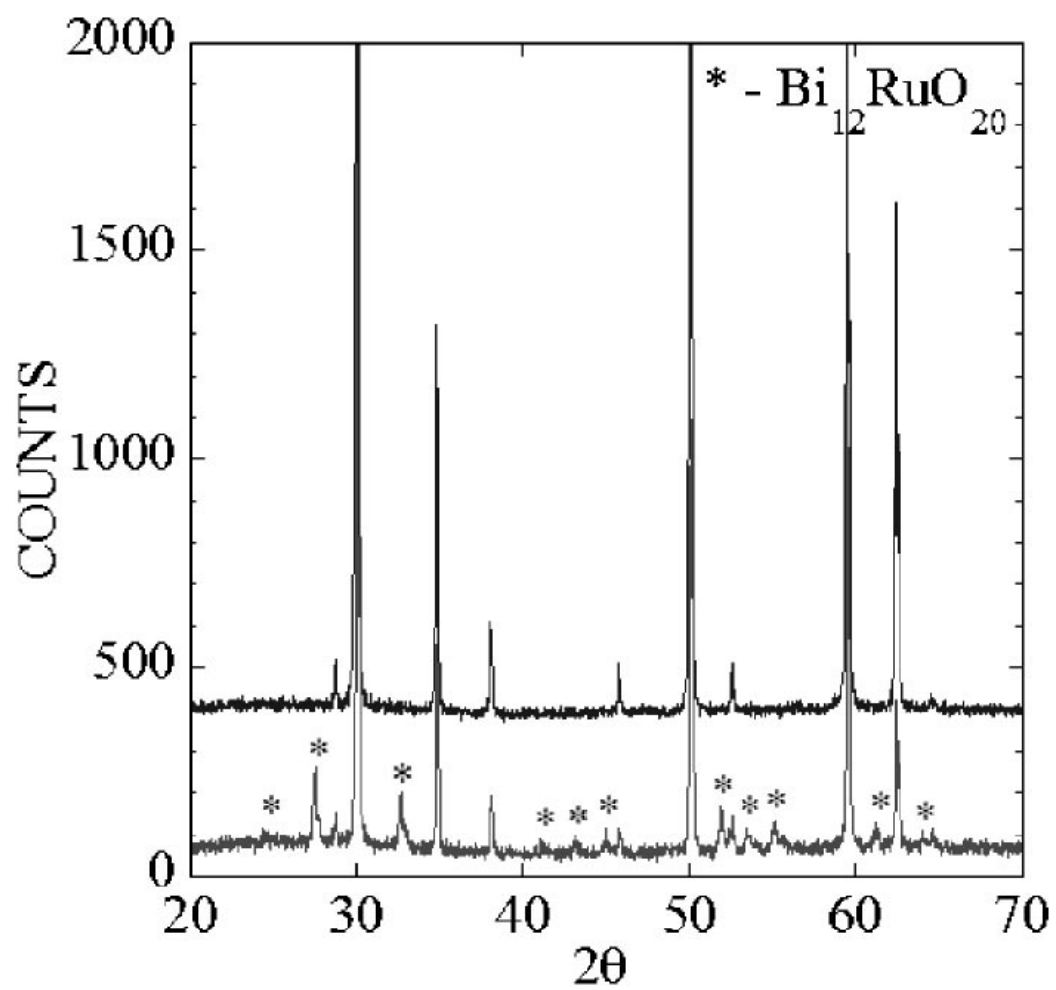


Figure A-3. Diffraction patterns of BRO7 (bottom) before and (top) after leaching taken from the literature<sup>23</sup>

## APPENDIX B IMPEDANCE SPECTROSCOPY

A short description of impedance spectroscopy is given in this section for better understanding the electrochemical response since it was one of the main characterization techniques utilized in this dissertation.

Electrochemical impedance spectroscopy (EIS) is a valuable tool for characterization of electrochemical processes. A small AC potential (across a range of frequencies) is applied to the sample, and the current response (impedance using Ohm's Law) through the sample is measured over a range of frequencies. This response is usually represented as a "Nyquist" or "Cole-Cole" plot where the real part of the impedance is the abscissa and the imaginary part of the impedance the ordinate (usually the negative and positive portions of the imaginary axis are reversed for simplicity). The response of the cell is usually modeled in terms of equivalent circuits, i.e. a group of electrical circuit elements (resistors, capacitors, inductors) that are connected in a way that would give the same response as the cell.

A common cell response feature (a semi-circle), and its equivalent circuit representation (a resistor and capacitor in parallel) are shown in Figure B-1. Such behavior could be characteristic, for example, of a double-layer capacitance (resulting from charge separation between electrode and electrolyte) in parallel with a resistance to charge transfer or a polarization resistance. It should be noted that the magnitude of the impedance decreases as frequency increases. The semi-circle is characteristic of a single "time-constant". Typical impedance plots of electrochemical cells contain more than one time constant (semi-circle) indicative of more than one electrochemical process, and often only a portion of one or more of the semi-circles is seen.

Often two time constants will overlap and the semi-circles must be deconvoluted in order to determine each individual contribution. Also it should be mentioned that many times in the study of solid samples, the center of the semi-circle may be depressed below the x-axis. The equivalent circuit is similar to that in Figure B-1, but the capacitor is replaced by a so-called constant-phase element (CPE). A capacitor can be thought of as a constant phase element whose phase angle (the phase difference between voltage and current responses) is  $90^\circ$ . When this phase angle is somewhat less than this, a depressed semi-circle is observed. This behavior has been explained in a number of ways. Surface roughness of the electrode is one explanation—for example, it is common for electrochemical cells with solid electrodes (which typically have rough surfaces) to display this behavior while it is not observed on mercury electrodes (which are atomically smooth).

Another common cell response feature on a Nyquist plot is a straight line with a  $45^\circ$  angle (Figure B-2). This feature is usually modeled by so-called Warburg impedance and is characteristic of semi-infinite diffusion. As shown in Figure B-2, in many cases at low frequencies, the plot forms an arc. This is justified because at high frequencies, the time for a molecule to diffuse through, for example, a porous cathode is much longer than the period of the applied AC stimulus, hence the molecule does not 'see' that the cathode is of finite thickness.

The response of a cell can be perfectly modeled by a number of different equivalent circuits. Knowledge of the physical processes occurring in each cell can help identify the most appropriate model. The model can be justified by altering a single

aspect of the cell (e.g. grain size, Figure B-3)<sup>104</sup> and verifying that the impedance spectrum changes in such a way that is as predicted by the model.

Another typical cell response and equivalent circuit model are shown in Figure B-4. This figure will be used as an example for calculation of various cell parameters. The simplest parameter to extract is the total ohmic resistance of the cell, given as  $R_{\Omega}$  in the figure. This is also known as the solution or electrolyte resistance. It should be noted at this point that while in this case the electrolyte response behaves as a pure resistor, in many polycrystalline electrolytes the response may exhibit some capacitive behavior due to the grains (bulk) and the grain boundaries, hence up to two semi-circles may appear in this region of the Nyquist plot (as in Figure B-4).  $R_{ct}$  is the charge transfer resistance (which is controlled by the kinetics of the charge transfer reaction), and is measured as the difference between the extrapolated low frequency real axis intercept and the high frequency axis intercept. The rate of the charge transfer reaction can be modeled by the Butler-Volmer equation. Since in IS the applied signal is small, the overpotential (the electrode potential minus the equilibrium potential for the reaction) should be small, and the Butler-Volmer equation becomes

$$R_{ct} = \frac{RT}{nFi_0} \quad (B-1)$$

where  $R$ ,  $T$ ,  $n$ , and  $F$  have their usual meanings, and  $i_0$  is the exchange current density. Thus if  $R_{ct}$  is known, the exchange current density can be calculated.

Diffusion of species toward and away from the reaction sites usually gives the linear response shown at the low frequency end of the figure. Naturally this is not the only form of spectrum observed, and  $R_{ct}$  is not the only non-electrolyte resistance reported. Polarization resistance,  $R_p$ , and the more general electrode resistance,  $R_{el}$ ,

are frequently reported. However, in most all cases, the value for the resistance is measured as the difference between low and high frequency real-axis intercepts of the arc of interest.

Since resistance is not a materials parameter, cell geometry is usually taken into account, and IS results are reported in terms of resistivities or conductivities. For a particular resistance,

$$\rho = \frac{RA}{l} \quad (\text{B-2})$$

$$\sigma = \frac{1}{\rho} = \frac{l}{RA} \quad (\text{B-3})$$

where  $\rho$  is the resistivity,  $\sigma$  is the conductivity,  $A$  and  $l$  are the area and length over which a uniform current is carried, respectively. It is seen, for example that the ohmic contribution can be identified by performing a series of experiments, holding all experimental conditions the same while changing electrolyte thickness—a plot of  $R_{\Omega}$  versus electrolyte thickness should be a straight line with intercept zero. Area specific resistance is another parameter that is commonly reported, and is simply the resistance of interest multiplied by the area of interest. For example, the electrode resistance multiplied by the electrode area gives the electrode area-specific resistance ( $\Omega\text{cm}^2$ ).

These properties will often show an Arrhenius relationship with temperature, and a log plot of these parameters versus reciprocal temperature will give a straight line, the slope of which is reported as the activation energy of the specific process. With this brief description of EIS, one can begin to imagine how this technique can be utilized to help interpret cell behavior, as well as help determine rate-controlling processes.

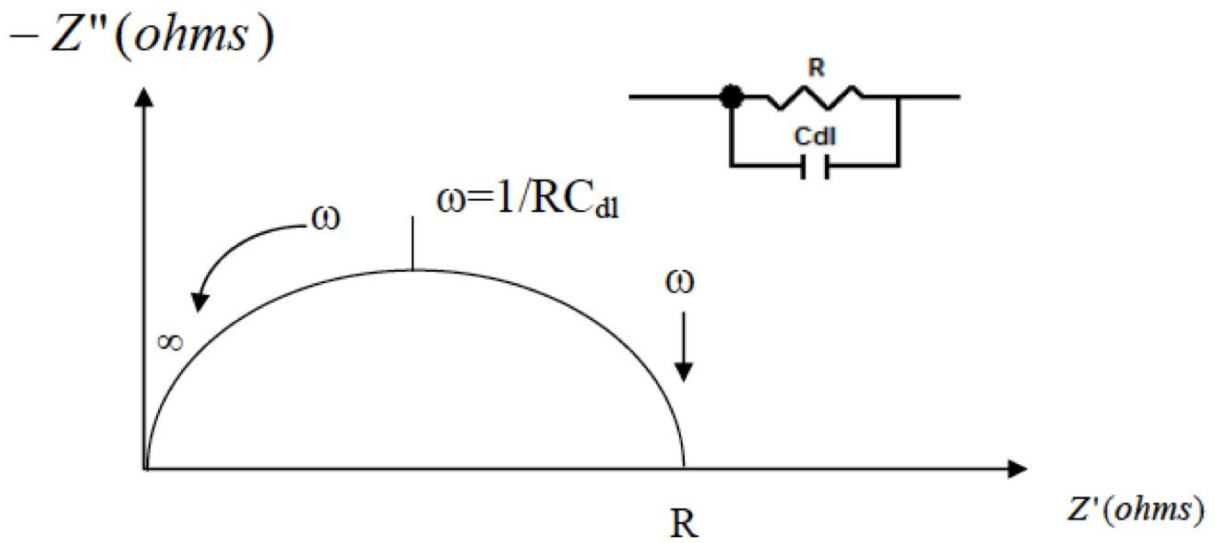


Figure B-1. Typical impedance cell response on complex plane and its equivalent circuit

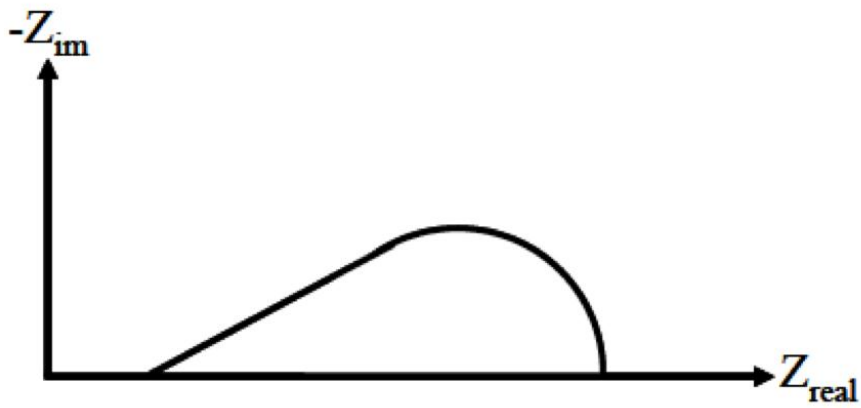


Figure B-2. Typical Warburg impedance response on complex plane

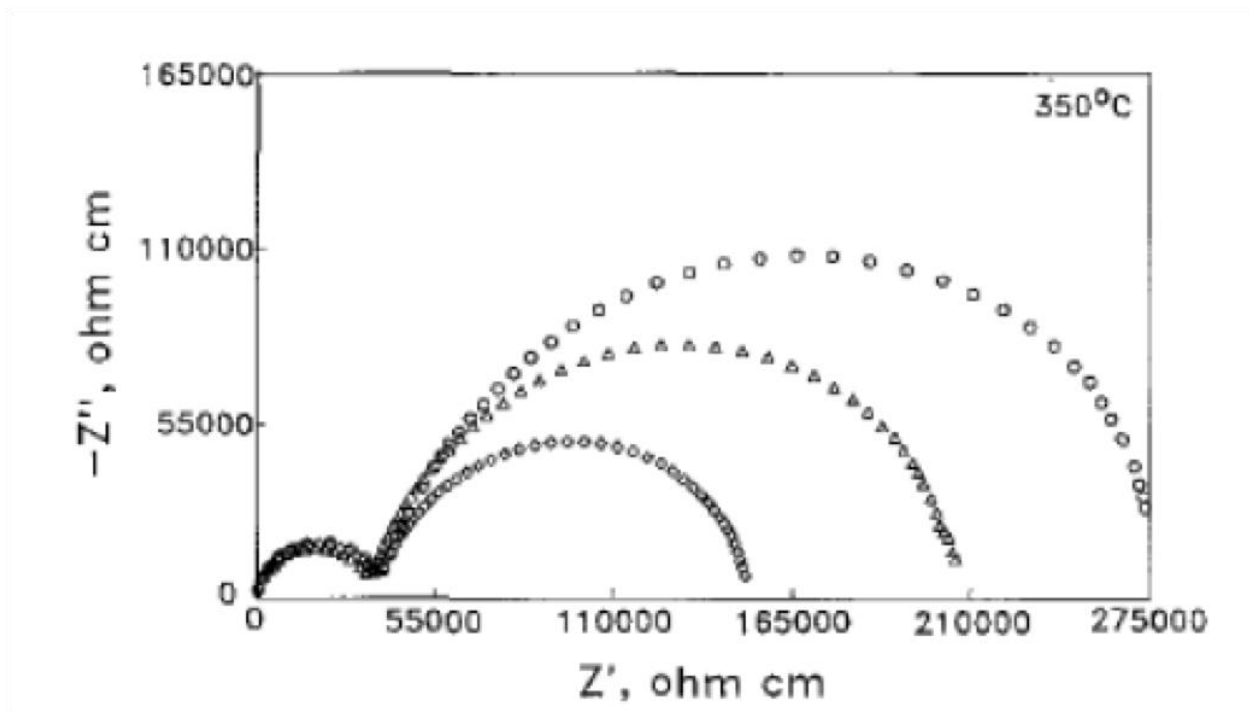


Figure B-3. Impedance response for as-sintered (1500°C, 4 hr) HS3Y samples (circles), annealed at 1200°C for 110 hr in both 10% H<sub>2</sub> balance N<sub>2</sub> atmosphere (triangles), and air (diamonds) showing the effect of increasing grain size<sup>104</sup>

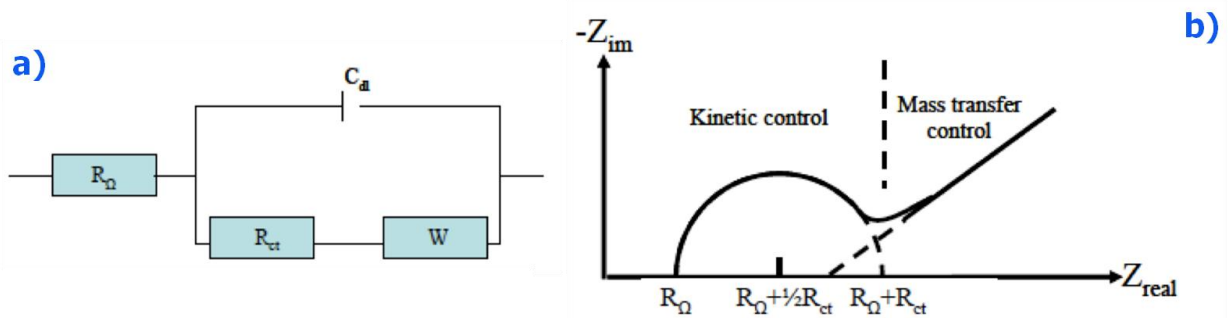


Figure B-4. a) Equivalent circuit and b) impedance response in complex plane for mixed kinetic and charge transfer control

## LIST OF REFERENCES

1. M. C. Williams, *Fuel Cells*, **7**, 78 (2007).
2. O. Yamamoto, *Electrochim Acta*, **45**, 2423 (2000).
3. J. M. Ralph, A. C. Schoeler and M. Krumpelt, *J Mater Sci*, **36**, 1161 (2001).
4. S. M. Haile, *Acta Mater*, **51**, 5981 (2003).
5. J. Fleig, *Annu Rev Mater Res*, **33**, 361 (2003).
6. E. P. Murray and S. A. Barnett, *Solid State Ion.*, **143**, 265 (2001).
7. V. Dusastre and J. A. Kilner, *Solid State Ion.*, **126**, 163 (1999).
8. M. Liu and Z. Wu, *Solid State Ion.*, **107**, 105 (1998).
9. A. Jaiswal, C. T. Hu and E. D. Wachsman, *J Electrochem Soc*, **154**, B1088 (2007).
10. M. Camaratta and E. Wachsman, *J Electrochem Soc*, **155**, B135 (2008).
11. Z. P. Shao and S. M. Haile, *Nature*, **431**, 170 (2004).
12. P. W. Li and M. K. Chyu, *Transactions of the ASME*, **127**, 1344 (2005).
13. J. Newman and K. E. Thomas-Alyea, *Electrochemical Systems* Wiley Interscience, Hoboken, New Jersey (2004).
14. B. C. H. Steele, *Solid State Ion.*, **75**, 157 (1995).
15. E. D. Wachsman, *J Eur Ceram Soc*, **24**, 1281 (2004).
16. N. X. Jiang, E. D. Wachsman and S. H. Jung, *Solid State Ion.*, **150**, 347 (2002).
17. M. J. Verkerk, K. Keizer and A. J. Burggraaf, *J Appl Electrochem*, **10**, 81 (1980).
18. B. C. H. Steele, *Solid State Ion.*, **129**, 95 (2000).
19. T. Takahashi, T. Esaka and H. Iwahara, *J Appl Electrochem*, **7**, 299 (1977).
20. E. D. Wachsman, P. Jayaweera, N. Jiang, D. M. Lowe and B. G. Pound, *J Electrochem Soc*, **144**, 233 (1997).
21. J. Y. Park, H. Yoon and E. D. Wachsman, *Journal of the American Ceramic Society*, **88**, 2402 (2005).

22. E. Girdauskaite, H. Ullmann, M. Al Daroukh, V. Vashook, M. Bulow and U. Guth, *J Solid State Electr*, **11**, 469 (2007).
23. A. Jaiswal and E. D. Wachsman, *J Electrochem Soc*, **152**, A787 (2005).
24. J. M. Bae and B. C. H. Steele, *J Electroceram*, **3**, 37 (1999).
25. T. Takeda, R. Kanno, Y. Kawamoto, Y. Takeda and O. Yamamoto, *J Electrochem Soc*, **147**, 1730 (2000).
26. Z. M. Zhong, *Electrochem Solid St*, **9**, A215 (2006).
27. G. R. Facer, M. M. Elcombe and B. J. Kennedy, *Aust J Chem*, **46**, 1897 (1993).
28. R. J. Bouchard and J. L. Gillson, *Mater Res Bull*, **6**, 669 (1971).
29. K. S. Lee, D. K. Seo and M. H. Whangbo, *J. Solid State Chem.*, **131**, 405 (1997).
30. W. Y. Hsu, R. V. Kasowski, T. Miller and T. C. Chiang, *Appl. Phys. Lett.*, **52**, 792 (1988).
31. T. Tsai and S. A. Barnett, *Solid State Ion.*, **93**, 207 (1997).
32. A. V. Virkar, J. Chen, C. W. Tanner and J. W. Kim, *Solid State Ion.*, **131**, 189 (2000).
33. T. Kenjo, S. Osawa and K. Fujikawa, *J Electrochem Soc*, **138**, 349 (1991).
34. C. W. Tanner, K. Z. Fung and A. V. Virkar, *J Electrochem Soc*, **144**, 21 (1997).
35. K. Sasaki, J. P. Wurth, R. Gschwend, M. Godickemeier and L. J. Gauckler, *J Electrochem Soc*, **143**, 530 (1996).
36. M. Kleitz and F. Petitbon, *Solid State Ion.*, **92**, 65 (1996).
37. J. Maier, *Solid State Ion.*, **148**, 367 (2002).
38. J. Maier, *J Eur Ceram Soc*, **24**, 1251 (2004).
39. P. Costamagna, P. Costa and V. Antonucci, *Electrochim Acta*, **43**, 375 (1998).
40. X. J. Chen, S. H. Chan and K. A. Khor, *Electrochim Acta*, **49**, 1851 (2004).
41. S. P. Jiang, Y. J. Leng, S. H. Chan and K. A. Khor, *Electrochem Solid St*, **6**, A67 (2003).
42. S. P. Jiang and W. Wang, *Solid State Ion.*, **176**, 1351 (2005).
43. Y. Huang, J. M. Vohs and R. J. Gorte, *Electrochem Solid St*, **9**, A237 (2006).

44. Y. Y. Huang, K. Ahn, J. M. Vohs and R. J. Gorte, *J Electrochem Soc*, **151**, A1592 (2004).
45. Y. Y. Huang, J. M. Vohs and R. J. Gorte, *J Electrochem Soc*, **151**, A646 (2004).
46. T. Z. Sholklapper, C. Lu, C. P. Jacobson, S. J. Visco and L. C. De Jonghe, *Electrochem Solid St*, **9**, A376 (2006).
47. S. P. Jiang and W. Wang, *J Electrochem Soc*, **152**, A1398 (2005).
48. F. Zhao, Z. Wang, M. Liu, L. Zhang, C. Xia and F. Chen, *J Power Sources*, **185**, 13 (2008).
49. J. Chen, F. L. Liang, B. Chi, J. Pu, S. P. Jiang and L. Jian, *J Power Sources*, **194**, 275 (2009).
50. W. Zhu, D. Ding and C. Xia, *Electrochem Solid St*, **11**, B83 (2008).
51. M. Shah, J. D. Nicholas and S. A. Barnett, *Electrochem Commun*, **11**, 2 (2009).
52. S. P. Jiang, *Mat Sci Eng a-Struct*, **418**, 199 (2006).
53. T. Z. Sholklapper, C. P. Jacobson, S. J. Visco and L. C. De Jonghe, *Fuel Cells*, **8**, 303 (2008).
54. J. M. Vohs and R. J. Gorte, *Adv Mater*, **21**, 943 (2009).
55. M. J. Jorgensen and M. Mogensen, *J Electrochem Soc*, **148**, A433 (2001).
56. Z. Y. Jiang, C. R. Xia and F. L. Chen, *Electrochim Acta*, **55**, 3595 (2010).
57. H. S. Horowitz, J. M. Longo and H. H. Horowitz, *J Electrochem Soc*, **130**, 1851 (1983).
58. R. G. Egdell, J. B. Goodenough, A. Hamnett and C. C. Naish, *J Chem Soc Farad T 1*, **79**, 893 (1983).
59. J. Prakash, D. Tryk and E. Yeager, *J Power Sources*, **29**, 413 (1990).
60. M. Kleitz, T. Iharada, F. Abraham, G. Mairesse and J. Fouletier, *Sensor Actuat B-Chem*, **13**, 27 (1993).
61. N. M. Markovic and P. N. Ross, *J Electrochem Soc*, **141**, 2590 (1994).
62. S. Linquette-Mailley, A. Caneiro, E. Djurado, G. Mairesse and J. Fouletier, *Solid State Ion.*, **107**, 191 (1998).
63. F. Abraham, Nowogroc.G and D. Thomas, *Cr Acad Sci C Chim*, **278**, 421 (1974).

64. M. Hrovat, S. Bernik and D. Kolar, *J Mater Sci Lett*, **7**, 637 (1988).
65. M. M. Milanova, M. Kakihana, M. Arima, M. Yashima and M. Yoshimura, *J Alloy Compd*, **242**, 6 (1996).
66. A. Kahoul, P. Nkeng, A. Hammouche, F. Naamoune and G. Poillerat, *J. Solid State Chem.*, **161**, 379 (2001).
67. C. Abate, V. Esposito, K. Duncan, J. C. Nino, D. M. Gattia, E. D. Wachsman and E. Traversa, *Journal of the American Ceramic Society*, **93**, 1970 (2010).
68. B. W. Liu and Y. Zhang, *J Alloy Compd*, **453**, 418 (2008).
69. L. A. Chick, L. R. Pederson, G. D. Maupin, J. L. Bates, L. E. Thomas and G. J. Exarhos, *Mater Lett*, **10**, 6 (1990).
70. K. Gurunathan, N. P. Vyawahare, G. J. Phatak and D. P. Amalnerkar, *J Mater Sci-Mater El*, **16**, 159 (2005).
71. S. R. Jain, K. C. Adiga and V. R. P. Verneker, *Combust Flame*, **40**, 71 (1981).
72. B. D. C. A. Wesley, *Elements of X-Ray Diffraction*, second ed., in, p. 284, Addison-Wesley, Reading, MA (1978).
73. M. E. Orazem, N. Pebere and B. Tribollet, *J Electrochem Soc*, **153**, B129 (2006).
74. M. Godickemeier, K. Sasaki, L. J. Gauckler and I. Riess, *Solid State Ion.*, **86-8**, 691 (1996).
75. Z. L. Wu and M. L. Liu, *Solid State Ion.*, **93**, 65 (1996).
76. B. C. H. Steele and A. Heinzl, *Nature*, **414**, 345 (2001).
77. F. Tietz, Q. Fu, V. A. C. Haanappel, A. Mai, N. H. Menzler and S. Uhlenbruck, *Int J Appl Ceram Tec*, **4**, 436 (2007).
78. C. R. Xia and M. L. Liu, *Adv Mater*, **14**, 521 (2002).
79. S. B. Adler, *Chem Rev*, **104**, 4791 (2004).
80. N. Shohata, T. Matsumura, K. Utsumi and T. Ohno, *Am Ceram Soc Bull*, **59**, 335 (1980).
81. D. Hotza and P. Greil, *Mat Sci Eng a-Struct*, **202**, 206 (1995).
82. R. E. Mistler, *Am Ceram Soc Bull*, **77**, 82 (1998).
83. A. Navarro, J. R. Alcock and R. W. Whatmore, *J Eur Ceram Soc*, **24**, 1073 (2004).

84. D. H. Yoon and B. I. Lee, *J Eur Ceram Soc*, **24**, 739 (2004).
85. L. Y. Wang, G. Y. Tang and Z. K. Xu, *Ceram Int*, **35**, 487 (2009).
86. M. J. Desroches, I. A. Castillo and R. J. Munz, *Part Part Syst Char*, **22**, 310 (2006).
87. C. H. Weng and W. C. J. Wei, *Journal of the American Ceramic Society*, **93**, 3124 (2010).
88. R. J. Hunter, *Introduction to Modern Colloid Science*, New York (1993).
89. V. A. Hackley, R. S. Premachandran, S. G. Malghan and S. B. Schiller, *Colloid Surface A*, **98**, 209 (1995).
90. M. N. Rahaman, *Ceramic Processing and Sintering*, Marcel Dekker, Inc., New York (1995).
91. P. C. Hidber, T. J. Graule and L. J. Gauckler, *J Eur Ceram Soc*, **17**, 239 (1997).
92. J. Cesarano, I. A. Aksay and A. Bleier, *Journal of the American Ceramic Society*, **71**, 250 (1988).
93. B. J. Briscoe, A. U. Khan and P. F. Luckham, *J Eur Ceram Soc*, **18**, 2169 (1998).
94. Y. Q. Liu, L. Gao and J. K. Guo, *Colloid Surface A*, **193**, 187 (2001).
95. E. P. Murray, T. Tsai and S. A. Barnett, *Solid State Ion.*, **110**, 235 (1998).
96. M. J. L. Ostergard, C. Clausen, C. Bagger and M. Mogensen, *Electrochim Acta*, **40**, 1971 (1995).
97. Y. J. Leng, S. H. Chan, K. A. Khor and S. P. Jiang, *J Solid State Electr*, **10**, 339 (2006).
98. L. Nie, M. Liu, Y. Zhang and M. Liu, *J Power Sources*, **195**, 4704 (2010).
99. N. M. Sammes, G. A. Tompsett, H. Nafe and F. Aldinger, *J Eur Ceram Soc*, **19**, 1801 (1999).
100. J. C. Boivin, C. Pirovano, G. Nowogrocki, G. Mairesse, P. Labrune and G. Lagrange, *Solid State Ion.*, **115**, 639 (1998).
101. B. A. Boukamp, *Solid State Ion.*, **136**, 75 (2000).
102. S. W. Jung, C. Lu, H. P. He, K. Y. Ahn, R. J. Gorte and J. M. Vohs, *J Power Sources*, **154**, 42 (2006).
103. Z. Jiang, L. Zhang, L. Cai and C. Xia, *Electrochim Acta*, **54**, 3059 (2009).

104. S. P. S. Badwal, *Solid State Ion.*, **76**, 67 (1995).

## BIOGRAPHICAL SKETCH

Byung Wook Lee was born and raised in Seoul, South Korea in 1979. He earned a bachelor's degree from the Department of Materials Science and Engineering at Hanyang University in Seoul, South Korea, in August 2005. He enrolled in the Department of Materials Science and Engineering at University of Florida in August 2006 to pursue PhD with special interest in the electrochemical energy device such as solid oxide fuel cell (SOFC) under guidance of Professor Eric D. Wachsman.